

Investigation of ground states of spin-1 Bose-Einstein condensate in a harmonic trap

A thesis

Submitted in partial fulfilment of the requirements

Of the degree of
Doctor of Philosophy

By

Projjwal Kanti Kanjilal

Registration ID : 20142026



INDIAN INSTITUTE OF SCIENCE EDUCATION AND RESEARCH PUNE

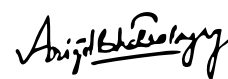
2023

To

*my parents and my grandfather,
the late Shyama Sankar Kanjilal*

CERTIFICATE

Certified that the work incorporated in the thesis entitled "**Investigation of ground states of spin-1 Bose-Einstein condensate in a harmonic trap**" submitted by **Projjwal Kanti Kanjilal** was carried out by the candidate, under my supervision. The work presented here or any part of it has not been included in any other thesis submitted previously for the award of any degree or diploma from any other University or institution.



Dr. Arijit Bhattacharyay
(Supervisor)

Date: 09.08.2023

DECLARATION

I declare that this written submission represents my ideas in my own words and where others' ideas have been included, I have adequately cited and referenced the original sources. I also declare that I have adhered to all principles of academic honesty and integrity and have not misrepresented or fabricated or falsified any idea/data/fact/source in my submission. I understand that violation of the above will be cause for disciplinary action by the Institute and can also evoke penal action from the sources which have thus not been properly cited or from whom proper permission has not been taken when needed.

Projjwal Kanti Kanjilal

Projjwal Kanti Kanjilal

Roll No. 20142026

Date: 09.08.2023

ACKNOWLEDGEMENTS

Firstly, I would like to express my heartfelt gratitude to my supervisor Dr. Arijit Bhattacharyay, for his guidance throughout my Ph.D., not only academically but also personally. I am deeply indebted to my research advisory committee members, Prof. Avinash Khare and Prof. Umakant Rapol for the various discussions and their valuable suggestions.

I would like to thank the Council of Scientific and Industrial Research (CSIR), India, and IISER Pune for providing funding during this research. The support and the resources provided by PARAM Brahma Facility under the National Supercomputing Mission, Government of India at the Indian Institute of Science Education and Research; Pune are gratefully acknowledged.

I had various discussions with Dr. Sourav Laha and Ratheejit Ghosh about different aspects of numerical studies, for which I am grateful to them. I would especially like to thank Dr. Abhijit Pendse for his help during the initial phase of my work and also to the past and present members of the group, Supratik, Akash, Mayank, and Aakash.

I would like to thank all my friends who made my stay at IISER memorable, especially Basudev, Banibrata, Suddhasatwa, Kartik, Anweshi, Arijeet, Arunabha, Mitesh, Souptik, Subhendu, Arnab. I would like to specially mention my college friends, Poulab, Debatri, and Ayan for their incessant support. I would also like to thank my Ph.D. batchmates.

The sports facilities at IISER Pune have been the key to dealing with the tough times. I would like to especially extend my gratitude to all the football teammates for the wonderful experiences shared. I would like to thank the gardening team for maintaining the IISER Pune cricket ground, where many memories belong. I would like to thank past and present members of our cricket team, especially Prasun, Aslam, Partha Da, Amit Da, Krishnendu, Sakil, Ratheejit, Arnab, Alok, Ajad, and Deepanjan for their fighting spirit

and the experience we shared.

It would have been difficult without the constant support provided by my family especially, my parents and uncles. I am grateful to my late grandfather, who taught me to value knowledge over everything. I am indebted to Sukanya for always inspiring me and being there.

SYNOPSIS

The main motivation for this thesis is to provide a general analytical framework to get the ground state profile correctly such that, associated ground state properties of a spin-1 Bose-Einstein condensate (BEC) under harmonic confinement are accurately known. In the following, we summarize the key issues and the way we have addressed those in this thesis.

- To the best of our knowledge, there was no existing general framework that can analytically estimate the ground state profile of spinor condensates with accuracy under harmonic trapping, which is routinely used in experiments. The ground state profiles are used to be estimated using the Thomas-Fermi (T-F) approximation [S1], which could be problematic for various reasons. One of the limitations is that it cannot estimate the condensate profile in the low-density region of the trap. Rather, according to the T-F approximation, the density profile sharply vanishes at the Thomas-Fermi radius, which is far from reality. To get the profile near this region, one had to rely on numerical simulation. One method to go beyond the T-F approximation exists for scalar BEC, which can model the profile in the low-density region [S2], but there it comes with a discontinuity in the condensate profile near the T-F radius.
- For homogeneous spinor BEC, investigation of phase transition at different values of p and q (the linear and quadratic Zeeman terms) has been done in detail [S3]. First, we looked into this problem for a trapped condensate (where density is not uniform) under the T-F approximation. We have shown that all the stationary states, that are the ground state candidates, can be obtained via the T-F approximation in a unified manner. We showed that the T-F approximated energy densities for different stationary states can be compared locally to get to the lowest energy domain-forming

structures. This analytical method of ours can capture a plethora of domain-forming possibilities in a unified way for a generic trapping potential [S4,S5].

- However, an analysis under the T-F approximation although believed to be mostly accurate for large condensates, can break down even for a large condensate in two distinct cases,
 - when there exist competing energies of ground state candidates such that, the error in the T-F approximation for not taking the kinetic energy (K.E.) contribution is of the order of the energy difference of those candidate states.
 - For multi-component states when different components have different T-F radii, which inevitably leads to an indication of domain formation in the ground state, under the T-F approximation. This may not be the case if the tail part of the distribution of the Zeeman components is properly taken into account.
- This requires developing a framework that takes into account the K.E. contribution in a continuous manner throughout the condensate. The framework should be multi-modal as well, as it has to treat different Zeeman projections for spinor condensate on an equal footing, which is important as the single-mode approximation often fails to describe the sub-component distributions accurately.
- Keeping these in mind, we have developed a multi-modal variational method (VM) using the low-lying harmonic oscillator states to model the low-density region of the condensate profile. This method can produce an accurate and continuous condensate profile of a harmonically trapped spin-1 BEC and produces refined predictions about associated ground state properties. We apply the VM in the two distinct cases,
 - In the absence of the magnetic field, the ground state candidates have a negligible energy difference with the T-F approximated ground state for a harmonically trapped condensate with the anti-ferromagnetic type of spin interaction. This renders the T-F approximated results inconclusive. The VM includes the K.E. and produces conclusive results even for small condensates with particle numbers as low as 500 [S6].
 - At particle number $\simeq 500$, the T-F approximation completely breaks down in 3-D condensates and the VM captures an accurate density profile in such a

regime. This number can be higher for different choices of trapping frequency corresponding to the 3-D isotropic harmonic trapping.

- In the presence of magnetic field, the VM corrects the T-F approximated prediction of domain formation in the multi-component ground state. While the SMA becomes inaccurate in estimating the sub-component density distribution, the VM produces accurate analytical expressions of the condensate profiles for each sub-component [S7].
- The VM accurately estimates the profile of the condensate and hence, the total energy of the ground state. The VM estimated total energy can be used to get to the phase diagram of trapped condensates. We look into the phase transition between the phase-matched and polar states (defined later) and estimate the phase boundary in (q, p) parameter space for a condensate with ferromagnetic type of spin-spin interaction under 3-D isotropic harmonic confinement to draw a detailed comparison with that of the homogeneous situation (in the absence of the trapping). We show that a unique scaling factor emerges, which shows the universality of these boundaries with respect to varying numbers of condensate particles [S7].

References

- [S1] L.P. Pitaevskii, S. Stringari, and Oxford University Press. Bose-Einstein Condensation. International Series of Monographs on Physics. Clarendon Press, 2003. ISBN 9780198507192.
- [S2] F. Dalfovo, L. Pitaevskii, and S. Stringari, Phys. Rev. A 54, 4213 (1996).
- [S3] Y. Kawaguchi and M. Ueda, Physics Reports 520, 253 (2012), Spinor Bose–Einstein condensates.
- [S4] P. K. Kanjilal and A. Bhattacharyay, Physica Scripta 95, 045702 (2020).
- [S5] P. K. Kanjilal and A. Bhattacharyay, Physica Scripta 97, 129501 (2022).
- [S6] Kanjilal, Projjwal Kanti and Bhattacharyay, A., Eur. Phys. J. Plus 137, 547 (2022).
- [S7] P. K. Kanjilal and A. Bhattacharyay, arXiv: 2301.06856, Multi-component states for trapped spin-1 Bose-Einstein condensates in the presence of magnetic field (2023).

Contents

Abstract	xix
1 Introduction	1
1.1 Bose-Einstein Condensation	2
1.1.1 Theoretical prediction	2
1.1.2 Road Towards Experimental Realization: The cold race	4
1.1.3 Experimental Observation of the Bose-Einstein condensate	5
1.2 Spinor Bose-Einstein Condensate	7
1.2.1 Some unique features of spinor condensate	8
2 Spin-1 Bose-Einstein Condensate: Basic formalism	11
2.1 Hamiltonian for contact interaction	11
2.2 Mean-field theory	13
2.3 Gross-Pitaevskii equation	15
2.4 Stationary states and Phase Diagram in absence of trapping	16
3 Domain formation in a trapped spin-1 BEC	21
3.1 Stationary states in the presence of trapping potential	22
3.1.1 Single-component states	25
3.1.2 Multi-component states	27
3.2 Domain formation possibilities:	36
3.2.1 In the absence of spin interaction	36
3.2.2 Anti-ferromagnetic type of spin interaction	41
3.2.3 Ferromagnetic type of spin interaction	46
3.3 Discussion	49

4	Variational method: Ground state properties in the absence of the magnetic field	53
4.1	T-F approximated total energy in the absence of the magnetic field	55
4.1.1	Stationary states at $p=0$ and $q=0$	56
4.1.2	The T-F approximated total energy for three-dimensional isotropic harmonic confinement	60
4.1.3	The T-F approximated total energy comparison in quasi-one-dimensional harmonic confinement	63
4.2	Variational Method	64
4.2.1	3-D isotropic harmonic confinement: Variational approach	65
4.2.2	3-D isotropic harmonic confinement: Results	72
4.2.3	Quasi-1-D harmonic confinement: Variational approach	75
4.2.4	Quasi-1-D harmonic confinement: Results	78
4.2.5	Comparison of the variational method with numerically obtained condensate profile	79
4.2.6	Energy Density of the ground state	83
4.3	Discussion	84
5	Multi-component stationary states in the presence of the magnetic field	87
5.1	GP equation in the non-dimensional form: Recap	88
5.2	Multi-component stationary states:	90
5.2.1	PM state: T-F study	91
5.2.2	PM state: The variational method	95
5.2.3	Anti-ferromagnetic state	105
5.3	Phase transition between PM and polar states under confinement	107
5.4	Discussion	114
6	Conclusion and future prospects	117
6.1	Major findings	117
6.2	Future directions	119
	Publications	121
	Bibliography	122

Abstract

In this thesis, we develop general methods to analytically obtain the ground state profiles and associated ground state properties of a spin-1 Bose-Einstein condensate under harmonic confinement with contact interaction. Firstly, from the Gross-Pitaevskii equation, we obtain the number density and energy density profiles of all possible stationary states using the Thomas-Fermi approximation for generic confinement. These stationary states compete to become the ground state in different parameter regimes. We show that a general method exists that can capture a lot of domain structures in a unified way. We show that by comparing the Thomas-Fermi approximated energy densities of different stationary states of a trapped system, under an essential constraint of the same chemical potential of the neighboring domains, one can actually capture the full spectrum of possible domain structures. While it is generally accepted that the Thomas-Fermi approximation is accurate for large condensates where the density is high enough to neglect the kinetic energy contribution compared to the interaction energies, we encounter situations, where even for large condensates, the Thomas-Fermi approximated predictions become inconclusive. We show that in the absence of the magnetic field, the Thomas-Fermi approximation predicts a ground state with which the other competing stationary states have a small energy difference, and the difference is of the order of the error introduced by the Thomas-Fermi approximation itself. Also in the presence of the magnetic field, for multi-component stationary states, the Thomas-Fermi approximation indicates domain structures in the ground state. In contrast, numerical simulations do not predict the same. The single-mode approximation, on the other hand, is also inaccurate in producing the sub-component profiles of the multi-component ground states. In such situations, one needs a multi-modal method to explain the ground state profiles and related properties analytically. We introduce a multi-modal variational method that smoothly

incorporates the kinetic energy contribution and analytically estimates the complete profile of the number density. In the absence of the magnetic field, this variational method not only produces a more accurate prediction for large condensates but also is accurate for condensates with particles as low as 500. For multi-component stationary states, the variational method accurately estimates the tail part of each sub-components ruling out the domain formation possibility in the ground state. We employ the variational method to analytically estimate the phase transition boundaries between the phase-matched and polar states for a condensate with a ferromagnetic type of spin-spin interaction under 3-D isotropic harmonic trapping. This helps to draw a detailed comparison with the same phase transition in a homogeneous system, i.e., in the absence of trapping. There exists universality of these phase boundaries with respect to varying numbers of condensate particles under a scaling of the coordinates that comes out from the analytical calculation of the variational method. The multi-modal variational method introduced in this thesis opens up the route for a range of analytical studies that requires the ground state profiles to start with.

Chapter 1

Introduction

In the late nineteenth century, a major challenge for theoretical physics was to explain the observed specific intensity of the black-body radiation as a function of the wavelength. One of the first major contributions came from Wilhelm Wien. The Wien distribution law partly explained the high-frequency or the low-wavelength region of the curve. In 1900, Lord Rayleigh and Sir James Jeans came up with a classical formulation based on the equipartition theorem which is now known as the Rayleigh-Jeans Law. This was able to explain the low-frequency region of the curve but failed to explain the high-frequency region. The classical formulation also predicted the famous ultraviolet catastrophe, which showed that the classical ideas that were trusted for more than two centuries may not be adequate. Later that year, Max Planck came up with an empirical expression that explained the curve accurately both in the high- and low-frequency range of the spectrum. Planck's blackbody radiation law was based on a hypothesis of quantization of the energy carried by the light, which is widely regarded as the birth of quantum mechanics. Albert Einstein took the concept of quantization further and successfully explained the photoelectric effect in 1905. The underlying principle that led to Planck's radiation law was still a mystery back then.

In 1925, Satyendra Nath Bose, while teaching at the University of Dhaka came to the realization that particle indistinguishability is essential in explaining the celebrated Planck's radiation law. After getting rejections for publishing the results, he sent the manuscript to Albert Einstein, who he thought would understand the implications of this idea. Einstein recognized the importance of this work and submitted this manuscript on

his behalf to *Zeitschrift für Physik* [1].

In Bose-Einstein statistics, the expectation value of the number of particles (bosons) occupying an energy state ϵ_i is [2],

$$\langle n_i \rangle = \frac{1}{e^{\beta(\epsilon_i - \mu)} - 1}, \quad (1.1)$$

where $\beta = \frac{1}{k_B T}$, with k_B being the Boltzmann constant and T is the absolute temperature. At this finite temperature T , the chemical potential μ should be lower than the lowest allowed energy state of the system. Otherwise, the expectation value of the number of particles in the lowest energy state becomes negative. The Bose-Einstein statistics not only provided a concrete picture of Planck's black-body radiation formula, but it also marked the birth of quantum statistics.

1.1 Bose-Einstein Condensation

1.1.1 Theoretical prediction

Albert Einstein extended the Bose-Einstein statistics for particles [3, 4]. All particles with integer spins, i.e., the bosons follow this fundamental quantum statistics. If we consider identical non-interacting free particles in a box of volume $V = L^3$, subjected to periodic boundary conditions, the single-particle wave function can be succinctly written as, $\psi_{\mathbf{k}} = \left(\frac{1}{L}\right)^{3/2} \exp(i\mathbf{k}\mathbf{r})$, where $\mathbf{k} = \frac{2\pi}{L}(n_1, n_2, n_3)$. Here, $n_{(1,2,3)}$ can be any positive or negative integer. If we think in terms of the k -space, states form a three-dimensional grid with regular spacing of $\frac{2\pi}{L}$. So a volume of $\frac{8\pi^3}{V}$ would contain a single particle eigenstate in the k -space. Thus, the density of the plane waves in the k -space is $\frac{V}{8\pi^3}$. When the volume V itself is large, we can treat the problem in a continuum manner. For particles with mass m , the energy is $\epsilon = \frac{\mathbf{p}^2}{2m}$, where \mathbf{p} is the momentum. The momentum \mathbf{p} is related to \mathbf{k} as $\mathbf{p} = \hbar\mathbf{k}$, thus, $\epsilon = \frac{\hbar^2\mathbf{k}^2}{2m}$. The number of single particle eigenstates confined in a small shell in k -space is converted in the small energy range $d\epsilon$ [2] as

$$\begin{aligned} g(\epsilon)d\epsilon &= 4\pi k^2 \left(\frac{d|\mathbf{k}|}{d\epsilon} d\epsilon \right) \left(\frac{V}{8\pi^3} \right) \\ &= \frac{Vm^{3/2}}{\sqrt{2}\pi^2\hbar^3} \epsilon^{1/2} d\epsilon. \end{aligned} \quad (1.2)$$

One can fill the single-particle states being guided by the Bose-Einstein distribution at a given temperature T . At a chemical potential μ , the total number of particles N is,

$$N(\mu) = \int_0^\infty \frac{1}{e^{\beta(\epsilon-\mu)} - 1} g(\epsilon) d\epsilon, \quad (1.3)$$

for $\epsilon - \mu \not\leq 0$. Assuming the lowest energy state to be such that $\epsilon_0 = 0$, the chemical potential should be $\mu \leq 0$. It is interesting to note that, if we increase the chemical potential and make it come closer to the lowest eigenenergy, the expectation of the number of particles in the lowest energy state diverges according to the Bose-Einstein statistics. If we put $\mu = \epsilon_0$ in Eq.1.1, $\langle n_0 \rangle$ diverges. For $\mu = 0$,

$$\begin{aligned} N(\mu = 0) &= \frac{Vm^{3/2}}{\sqrt{2\pi^2\hbar^3}} \int_0^\infty \frac{1}{e^{\beta\epsilon} - 1} \epsilon^{1/2} d\epsilon \\ &= V \left(\frac{\sqrt{2\pi mk_B T}}{h} \right)^3 \frac{2}{\sqrt{\pi}} \int_0^\infty \frac{\sqrt{z}}{e^z - 1} dz, \end{aligned} \quad (1.4)$$

where the last term is the Reimann zeta function $\zeta(3/2)$ and the thermal de Broglie wavelength is defined as, $\lambda_T = \frac{h}{\sqrt{2\pi mk_B T}}$. As a result,

$$\frac{N(\mu = 0)}{V} = \frac{\zeta(3/2)}{\lambda_T^3}, \quad (1.5)$$

is a critical density, which is the maximum allowed density under the continuum approximation [2]. If we add more particles into the system, the chemical potential being zero, or in close proximity to the ground state would only allow the particles to be accommodated in the ground state. This phenomenon is called the Bose-Einstein condensation and it happens at a transition temperature T_c defined as,

$$k_B T_c = \frac{h^2}{2\pi m} \left(\frac{N}{V\zeta(3/2)} \right)^{2/3}. \quad (1.6)$$

When the temperature is further lowered beyond this T_c , the thermal de Broglie wavelength becomes comparable to the interparticle separation. The quantum mechanical wave functions of particles start to overlap. As a result, the particles start to lose their "identity" and behave as a whole. This is the reason Bose-Einstein condensate (BEC) is considered a macroscopic quantum state.

In 1938 Firtz London [5] had proposed Bose-Einstein condensation to be responsible for the superfluidity in Helium. But the effect of interaction on BEC in realistic samples was not clear. In 1947 Bogoliubov [6] answered this question with his new perturbative approach. Later in 1956, the mathematical description of the Bose-Einstein condensation was generalized in the presence of interaction by Oliver Penrose and Lars Onsager [7]. They also proposed a general criterion for the Bose-Einstein condensation, which is also known as the Penrose-Onsager criterion that, the Bose-Einstein condensation is present whenever a single-particle quantum state is occupied by a finite fraction of the particles of the system. One of the most seminal contributions in the theoretical advancement of this field came in 1960 when Eugene Gross [8] and Lev Pitaevskii [9] independently came up with a mean-field analysis and proposed that, due to the macroscopic occupation of the ground state, the BEC can be described in terms of a wave function. The governing equation of this wave function (order parameter) is the celebrated Gross-Pitaevskii equation.

1.1.2 Road Towards Experimental Realization: The cold race

Temperature required for the BEC transition is of the order of 100 nK. We will briefly discuss the scientific pursuit toward achieving such temperatures.

The first modern idea of the cooling mechanism came from Michael Faraday, who noticed that under high-pressure, gas liquefies and when the pressure is released the liquid is again converted to gas. He deduced that the amount of heat needed for this liquid-to-gas transition is provided by the surroundings and thus, this process in principle reduces the surrounding temperature. Michael Faraday liquefied many gases and achieved a temperature of 143 K. He was not able to liquefy hydrogen, nitrogen, and oxygen, thus naming them permanent gases. These were not at all permanent gases, and J. D. van der Waals theoretically showed in low enough temperatures and high enough pressure these gases can be liquefied. Later, the nitrogen and the oxygen gases were liquefied. The remaining piece of the puzzle was hydrogen. Physicist James Dewar and his closest competitor Kamerlingh Onnes were fascinated by this challenge. Both of them worked tirelessly to be the first to liquefy the hydrogen. James Dewar came out to be the first to do so and attained the lowest temperature recorded at that time which was around 21 K. Just after his success, it was realized that the boiling point of the newly found

(on earth) inert gas helium is at an even lower temperature at around 4 K. This time Kamerlingh Onnes won the race to liquefy the Helium gas (in 1908) and attain an even lower temperature of 1.5 K. By immersing a mercury wire in the liquid helium he noticed that the resistance of the mercury in response to the current flow suddenly vanishes, which he termed superconductivity.

The race towards absolute zero led to this observation of the phenomenon known as superconductivity, which in turn gave a hint that new properties of matter await in the low-temperature regions. This was achieved more than a decade before the first prediction of the Bose-Einstein condensation.

1.1.3 Experimental Observation of the Bose-Einstein condensate

After the theoretical prediction of the Bose-Einstein condensation phenomenon, the scientific community tried to get this new phase experimentally. But to get to even lower temperatures towards absolute zero, it required new cooling technologies.

To experimentally realize the Bose-Einstein condensate, hydrogen is a suitable element. Being the lightest atom, the BEC transition temperature (Eq.1.6) for hydrogen is expected to be larger than other elements. Still, it needed to cool down to μK range. The first step towards this goal came from the laser cooling technique [10, 11].

In laser cooling, carefully tuned lasers are employed that can cool down atoms. If we tune the laser slightly below the transition frequency allowed by the atom, only atoms coming toward the laser source would see it blue-shifted due to the Doppler effect. If the blue-shifted laser light is resonant with the allowed transition frequency, the atoms absorb it and later release photons with greater energy. This way atoms cool down even further. But this method can only reduce the temperature of the sample to the mK region.

A magnetic trap that confines such a system relies on the fact that the energy of an atom carrying a magnetic moment $\boldsymbol{\mu}$ placed under the magnetic field \mathbf{B} varies as $E = -\boldsymbol{\mu} \cdot \mathbf{B}$. If the magnetic field varies in space, then the atoms with hyperfine projections for which $\boldsymbol{\mu}$ becomes parallel to the magnetic field, would cluster around the higher magnetic field to reduce its energy (high-field seeking states). Similarly atoms with low-field seeking

hyperfine projections for which the contribution in energy is positive would try to cluster in the lower magnetic field strength. In free space, there can be a minimum of the varying magnetic field but there cannot be any maximum [12]. As a result, only low-field seeking states with magnetic moment anti-parallel to the magnetic field get trapped inside a magnetic trapping[13].

The last stage of the cooling process is the evaporative cooling technique [14]. This is quite similar to the way a cup of coffee cools down. The molecules carrying more energy leave the coffee cup, and the remaining molecules redistribute. In this way, the temperature of the coffee gets reduced. In a very similar manner, an additional radio-frequency field is applied to the system which assists the high-energy particles to escape the system and thus, reduces temperature to attain the Bose-Einstein condensate. The only issue with this method is that a significant amount of the trapped particles are lost in the process. Using the dimple trap [15], it was shown that this limitation can be avoided.

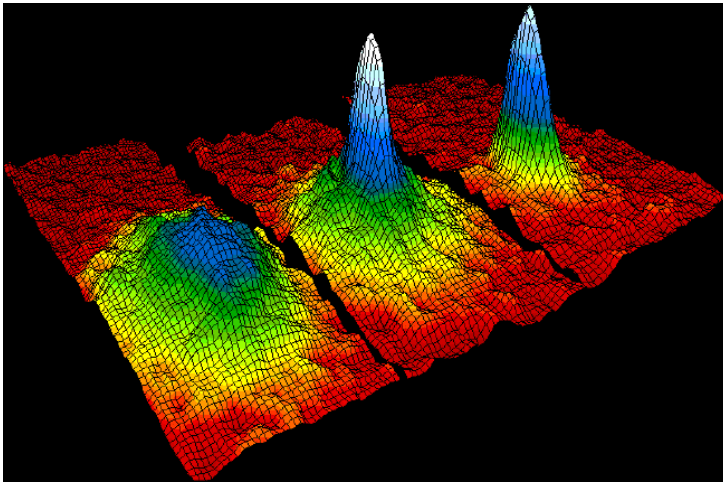


Figure 1.1: The velocity distribution in a two-dimensional plane for Rb-87 for three different temperatures, first observed in JILA [16]. (left image) When the temperature is slightly above the critical temperature, the velocity distribution is smooth and is Maxwell-Boltzmann-like. (middle image) Just below the critical temperature, a sharp peak in the velocity distribution can be observed which is indicative of a large population in the ground state, hence the indication of BEC. (right image) Reduction in temperature further only makes the peak more pronounced and it can be deduced that a pure BEC has formed. Image source- Wikipedia (https://en.wikipedia.org/wiki/Bose-Einstein_condensate).

As expected, the effort to get to a Bose-Einstein condensate started with hydrogen atoms. But, due to technical issues, it was difficult for the MIT group of Greytak and

Kleppner to overcome the challenge to cool down to the BEC transition temperature. Later, following a "gut intuition" Eric Cornell and Carl Wieman selected the heavier ^{87}Rb for this purpose [17]. In 1995 the BEC was first observed by them with only 3000 atoms [16] at around a transition temperature of 170 nK. A few months later, Wolfgang Ketterle managed to get the Bose-Einstein condensate with almost half a million ^{23}Na particles [18]. In the same year, ^7Li was Bose-condensed [19] which had a very low density and is generally very unstable due to the attractive interaction. Finally, in 1998, after a long battle of almost two decades, the Greytak-Kleppner group achieved the BEC of hydrogen atoms [20] at a much higher transition temperature of $50\mu\text{K}$.

The experimental success rekindled theoretical interests [21–23] and attracted a lot of attention from both atomic- and condensed-matter physics communities. The unprecedented experimental control of BEC allows for the precision measurements [24–29]. In recent times, BEC is often hailed for being the ideal candidate as a quantum simulator [30–37]. To this date, not only other alkali isotopes of Potassium [38, 39] and Cesium [40] but strontium [15] and some rare-earth metal isotopes of Erbium (^{168}Er) [41], Dysprosium (^{160}Dy , ^{162}Dy , and ^{164}Dy) [42, 43], and Ytterbium (^{170}Yb) [44] have also been successfully Bose-condensed.

1.2 Spinor Bose-Einstein Condensate

The magnetic trapping technique only allows for the formation of the BEC with the low-field seeking hyperfine projections [45, 46]. As a result, all the constituent atoms in the BEC are of a single spin type. After the formation of BEC inside the magnetic trap, if the BEC can be held in some other way that does not energetically prefer a single spin state, then the spin degrees of freedom on top of the density variation can result in a richer system. The optical trap [47], which uses the electric dipole moment of the constituent atoms induced by the optical electric field [48], does this job. Furthermore, with a radio-frequency sweep [47], the atoms undergo a spin-flip transition which leads to atoms relaxing toward the equilibrium distribution [49]. Such a BEC with spin degrees of freedom is often referred to as spinor BEC. The BEC with no spin degrees of freedom is called a scalar BEC. Creation of spinor BEC [49–53] led to significant theoretical research [54, 55] on the ground state properties of the spinor condensates with particles having

hyperfine unity (spin-1).

1.2.1 Some unique features of spinor condensate

For a spinor BEC with all possible hyperfine projections corresponding to spin- f (with integer f), the BEC will have a vector order parameter with $(2f + 1)$ components [47, 56]. The density distributions for various spin degrees of freedom open up the possibility of having rich spin-textures [57–60] which could show some unique topological features [61–64]. Due to the spin-gauge symmetry [48], spinor-BEC supports some unique vortex structures like fractional vortices [65], Alice vortices [66–68] and also non-Abelian vortices [69, 70].

The soliton structure appearing in the spinor condensate has some unique features, where having more than one component allows for the formation of dark-bright soliton complexes [71–74]. Spinor condensates can support quasiparticles like magnons [75–77] and magnetic solitons [78, 79] along with some interesting skyrmion structures [80–82].

Under spin-spin interactions, spinor condensates provide a rich ground state phase diagram [83]. The controllable parameters like magnetic fields can be tuned to force the system to undergo phase transitions. The spinor condensate prepared in a non-equilibrium state also undergoes spin oscillation dynamics [48], which is a subject of intense study as it occurs on a time scale that is much slower than that in solids. The spin oscillation dynamics [83–88] also depends on the external magnetic field that can be controlled with excellent precision. This sensitivity to the magnetic field opens up the possibility of using the spinor condensate in sensing for example as a magnetometer [89–93] and as an interferometer [94].

In this thesis, we focus on ground state structures of trapped spin-1 BEC, i.e., the condensate atoms have hyperfine spin-1. Domain structure arising in a spin-1 condensate in different situations is an active area of research [95–113]. We understood that there is a need to develop an analytical method that can predict different domain formation possibilities of a trapped spin-1 BEC in a unified way. We show that it is, in general, possible under the Thomas-Fermi approximation to analytically predict (in Chapter 3) a plethora of domain formation possibilities that arise due to the interplay of the interactions, trapping potential, and external magnetic fields. We show that under a single essential con-

straint of the same chemical potential for all the stationary states, the Thomas-Fermi approximated energy density can reveal a rich variety of domain structures in a general manner. The Thomas-Fermi approximation applies to large condensates where the kinetic energy contribution could be neglected in comparison to the contribution coming from the interaction terms.

Although the Thomas-Fermi approximation is generally more or less accurate in the central region of the trap where the condensate density is large, away from the trap center as the trapping potential increases, the Thomas-Fermi approximation gives an inaccurate condensate profile. This is due to the fact that the Thomas-Fermi approximation throws away the kinetic energy contribution. So there is obviously a need for a better analytical method. In Chapter 4, we construct a multi-modal variational method that overcomes all these limitations of the Thomas-Fermi approximation and produces accurate results for situations where the kinetic energy contribution must be included.

In Chapter 4, we probe the ground state property of the spin-1 system inside harmonic confinement and in the absence of the magnetic field. In such a system, the Thomas-Fermi approximated energy difference of the competing stationary states is very small for an anti-ferromagnetic type of spin-spin interaction. Even for large condensates, the relative energy difference is so small that the kinetic energy contribution (which the Thomas-Fermi approximation disregards) can alter the conclusion about the ground state. As a result, the Thomas-Fermi approximation is inconclusive in such a situation even for large condensates. Our variational method overcomes this problem and finds the ground state much more accurately. The condensate profile that the variational method estimates is in excellent agreement with numerically simulated accurate profiles for large condensates as well as for small condensates with particle numbers as low as 500.

In Chapter 5, we demonstrate the multi-modal nature of the variational method in more details by dealing with the multi-component stationary states. The Thomas-Fermi approximation actually breaks down and indicates the wrong physical scenario of domain formation in such situations. On top of that, the widely used single-mode approximation is also incapable of producing an accurate sub-component density distribution. Situations like this force one to rely on numerical simulation in the absence of a trustworthy analytical method. However, numerical analysis in higher dimensional space is also computa-

tionally very expensive. We demonstrate that in the presence of the magnetic field, our multi-modal variational method produces an accurate description of the multi-component ground state structures. We show that the method estimates the phase transition boundaries between different ground states for a condensate under harmonic confinement. For a condensate with a ferromagnetic type of spin-spin interaction, the phase transition boundaries between the phase-matched and the polar states are estimated for different particle numbers. We demonstrate the similarity and the contrast of this phase transition for trapped condensate with that of the homogeneous situation (in the absence of trapping). We also show the universality of the phase-transition boundaries with respect to the number of condensate particles.

The motivation of the thesis is to produce an alternative and accurate analytical method that can be relied upon to probe the ground state structures of a spin-1 BEC under confinement. The methods shown in this thesis may be used in other analyses that require accurate ground state density profiles, on which depends the values of the total energy and energy density distribution. Our method, being a fairly general one, could be extended easily to higher spin systems as well.

Chapter 2

Spin-1 Bose-Einstein Condensate: Basic formalism

In this chapter, we will briefly discuss some basic and known theoretical aspects of spin-1 BEC which are used in the subsequent chapters. The contents of this chapter are mainly compiled from the nice review article by Kawaguchi and Ueda [83].

2.1 Hamiltonian for contact interaction

The field operator for a spin-1 BEC has three components corresponding to three Zeeman projections. Under mean-field approximation, one can express these field operators in terms of the mean fields (complex numbers) or the wave functions. Assuming the fluctuations are negligible, one can get to the equation of motion corresponding to these mean fields that is the Gross-Pitaevskii (GP) Equation [83].

The second-quantized Hamiltonian for the field operators can be written as a sum of the non-interacting and interaction terms,

$$\hat{\mathcal{H}} = \hat{\mathcal{H}}_{sp} + \hat{\mathcal{H}}_{int}. \quad (2.1)$$

The non-interacting or single-particle Hamiltonian accommodates the kinetic energy contribution, potential energy due to confinement, and also includes the effect of the magnetic

field,

$$\hat{\mathcal{H}}_{sp} = \int d\mathbf{r} \sum_{m,m'=-1}^1 \hat{\psi}_m^\dagger \left[-\frac{\hbar^2}{2M} \nabla^2 + U(\mathbf{r}) - p(f_z)_{mm'} + q(f_z^2)_{mm'} \right] \hat{\psi}_{m'}, \quad (2.2)$$

where M is the mass of a boson undergoing Bose-Einstein condensation and $U(\mathbf{r})$ is the trapping potential. The effect of a small magnetic field B is captured in the last two terms, where p and q are the linear and quadratic Zeeman terms. The linear term is defined as $p = -g\mu_B B$, where g is the Landé g -factor and μ_B is the Bohr magneton. The quadratic Zeeman term is a combination of the contributions coming from the magnetic field B and from a microwave or light field, i.e., $q = q_B + q_{MW}$. For a hyperfine energy splitting, $\Delta\mathcal{E} = \mathcal{E}_{int} - \mathcal{E}_i$, which is the energy difference between the initial (\mathcal{E}_i) and intermediate energies (\mathcal{E}_{int}), the second order perturbation determines, $q_B = \frac{(g\mu_B B)^2}{\Delta\mathcal{E}}$. Due to the other contribution coming from q_{MW} , which can be implemented by shining a linearly polarized microwave field that is off-resonant with the other hyperfine states, one can tune the linear (p) and quadratic (q) Zeeman terms independently. The f_z in the last two terms of Eq.(2.2) is the z -component of the Pauli spin-1 matrices [83],

$$f_x = \frac{1}{\sqrt{2}} \begin{bmatrix} 0 & 1 & 0 \\ 1 & 0 & 1 \\ 0 & 1 & 0 \end{bmatrix}, \quad f_y = \frac{i}{\sqrt{2}} \begin{bmatrix} 0 & -1 & 0 \\ 1 & 0 & -1 \\ 0 & 1 & 0 \end{bmatrix}, \quad f_z = \begin{bmatrix} 1 & 0 & 0 \\ 0 & 0 & 0 \\ 0 & 0 & -1 \end{bmatrix}. \quad (2.3)$$

We assume the system to be dilute so that only two-body contact interaction is present. If two identical spin- f particles are exchanged, the many-body wave function changes by a phase factor $(-1)^{2f}$. For the combined hyperfine spin \mathcal{F} and the relative angular momentum \mathcal{L} of such a pair, a two-body interaction will change the spin and the orbital part of the wave function by $(-1)^{\mathcal{F}+2f}$ and $(-1)^\mathcal{L}$ respectively [83]. So, in such an interaction $\mathcal{F} + \mathcal{L}$ should be an even number. For low-energy collisions, it can be safely assumed that $\mathcal{L} = 0$, or a s -wave scattering. As a result, for a spin-1 BEC the interaction can only happen when the combined hyperfine spin is either $\mathcal{F} = 0$, or $\mathcal{F} = 2$. Interaction through $\mathcal{F} = 1$ channel is prohibited.

The Hamiltonian for the two-body contact interaction can be modeled as

$$\hat{\mathcal{H}}_{int} = \sum_{\mathcal{F}=0,2} \left[\frac{1}{2} \int d\mathbf{r} \int d\mathbf{r}' g_{\mathcal{F}} \delta(\mathbf{r} - \mathbf{r}') \sum_{\mathcal{M}=-\mathcal{F}}^{\mathcal{F}} \hat{\mathcal{A}}_{\mathcal{F},\mathcal{M}}^\dagger(\mathbf{r}, \mathbf{r}') \hat{\mathcal{A}}_{\mathcal{F},\mathcal{M}}(\mathbf{r}, \mathbf{r}') \right], \quad (2.4)$$

where $\delta(\mathbf{r} - \mathbf{r}')$ is a delta function, $\hat{\mathcal{A}}_{\mathcal{F}\mathcal{M}}(\mathbf{r}, \mathbf{r}')$ is a pair-annihilating operator that annihilates a pair of bosons at a position \mathbf{r} and \mathbf{r}' with total spin \mathcal{F} and projection \mathcal{M} , i.e.,

$$\hat{\mathcal{A}}_{\mathcal{F}\mathcal{M}}(\mathbf{r}, \mathbf{r}') = \sum_{m_1, m_2=-1}^1 \langle \mathcal{F}, \mathcal{M} | 1, m_1, 1, m_2 \rangle \hat{\psi}_{m_1}(\mathbf{r}) \hat{\psi}_{m_2}(\mathbf{r}'), \quad (2.5)$$

and the $g_{\mathcal{F}}$ is the interaction strength in spin- \mathcal{F} channel which is related to the s -wave scattering length $a_{\mathcal{F}}$ as $g_{\mathcal{F}} = \frac{4\pi\hbar^2}{M} a_{\mathcal{F}}$.

The interaction Hamiltonian can be further simplified and expressed as [83]

$$\hat{\mathcal{H}}_{int} = \frac{1}{2} \int d\mathbf{r} \left(c_0 : \hat{n}^2(\mathbf{r}) : + c_1 : \hat{F}^2(\mathbf{r}) : \right), \quad (2.6)$$

using \hat{n} and \hat{F}_i which are the number- and spin density operators respectively,

$$\hat{n}(\mathbf{r}) = \sum_{m=-1}^1 \hat{\psi}_m^\dagger(\mathbf{r}) \hat{\psi}_m(\mathbf{r}), \quad (2.7)$$

$$\hat{F}_i = \sum_{m, m'=-1}^1 (f_i)_{mm'} \hat{\psi}_m^\dagger(\mathbf{r}) \hat{\psi}_{m'}(\mathbf{r}), \quad (2.8)$$

where f_i (for $i = x, y, z$) are the Pauli spin-1 matrices defined earlier in Eq.2.3. The notation $::$ in Eq.2.6 represents the usual normal ordering. Written in this way, c_0 and c_1 are the combinations of the s -wave scattering lengths in spin-0 and spin-2 channels, i.e.,

$$c_0 = \frac{4\pi\hbar^2}{M} \frac{a_0 + 2a_2}{3}, \quad c_1 = \frac{4\pi\hbar^2}{M} \frac{a_2 - a_0}{3}, \quad (2.9)$$

which can be identified as the spin-independent and spin-dependent interaction coefficients respectively.

2.2 Mean-field theory

To construct the mean-field theory, the field operators can be expressed as complex numbers,

$$\hat{\psi}_m(\mathbf{r}) = \sum_i \Phi_{mi}(\mathbf{r}) \hat{a}_{mi}, \quad (2.10)$$

where $\Phi_{mi}(\mathbf{r})$ takes care of the spatial dependence for a magnetic quantum number m and spatial mode i . Thus, $\{\Phi_{mi}(\mathbf{r})\}$ denotes a complete set of orthonormal basis functions

that satisfy the completeness relation,

$$\sum_i \Phi_{mi}^*(\mathbf{r})\Phi_{mi}(\mathbf{r}') = \delta(\mathbf{r} - \mathbf{r}'). \quad (2.11)$$

The basis functions also satisfy the orthonormality condition, i.e.,

$$\int d\mathbf{r} \Phi_{mi}^*(\mathbf{r})\Phi_{mj}(\mathbf{r}) = \delta_{ij}. \quad (2.12)$$

The bosonic annihilating operators follow a commutation relation,

$$[\hat{a}_{mi}, \hat{a}_{m'j}^\dagger] = \delta_{ij}\delta_{mm'}, \quad [\hat{a}_{mi}, \hat{a}_{m'j}] = [\hat{a}_{mi}^\dagger, \hat{a}_{m'j}^\dagger] = 0, \quad (2.13)$$

which ensures that the field operators also satisfy the following computation relations,

$$\begin{aligned} [\hat{\psi}_m(\mathbf{r}), \hat{\psi}_{m'}(\mathbf{r}')] &= 0, & [\hat{\psi}_m^\dagger(\mathbf{r}), \hat{\psi}_{m'}^\dagger(\mathbf{r}')] &= 0, \\ [\hat{\psi}_m(\mathbf{r}), \hat{\psi}_{m'}^\dagger(\mathbf{r}')] &= \delta_{mm'}\delta(\mathbf{r} - \mathbf{r}'). \end{aligned} \quad (2.14)$$

In mean-field approximation, one can safely assume that all the bosons occupy a single spatial mode $i = 0$ given the magnetic quantum number m . As a result, the spin state can be written as,

$$|\xi\rangle = \frac{1}{\sqrt{N!}}\hat{\mathcal{O}}^N|vac\rangle, \quad (2.15)$$

where N is the number of particles in the condensate and $|vac\rangle$ is the particle vacuum.

The operator \mathcal{O} is defined as

$$\hat{\mathcal{O}} = \sum_{m=-1}^1 \xi_m \hat{a}_{m0}^\dagger, \quad (2.16)$$

subjected to the normalization condition of the spinor, $\sum_{m=-1}^1 |\xi_m|^2 = 1$. Following the commutation relation Eq.2.13, it is straightforward to show that, $[\hat{a}_{m0}, \hat{\mathcal{O}}] = \xi_m$. This can be used to get to the relation,

$$\hat{a}_{m0}\hat{\mathcal{O}}^N = N\xi_m\hat{\mathcal{O}}^{N-1} + \hat{\mathcal{O}}^N\hat{a}_{m0}, \quad (2.17)$$

that one can use to calculate the mean values corresponding to the field operators and correlation functions [83]. If we assume the following definition for the wave function, $\psi_m(\mathbf{r}) = \sqrt{N}\xi_m\Phi_{m0}(\mathbf{r})$, the mean values of the field operator and the correlation functions

can be succinctly expressed in terms of the wave functions as

$$\begin{aligned}
 \langle \xi | \hat{\psi}_m(\mathbf{r}) | \xi \rangle &= \langle \xi | \hat{\psi}_m^\dagger(\mathbf{r}) | \xi \rangle = 0, \\
 \langle \xi | \hat{\psi}_m^\dagger(\mathbf{r}) \hat{\psi}_{m'}(\mathbf{r}') | \xi \rangle &= \psi_m^*(\mathbf{r}) \psi_{m'}(\mathbf{r}'), \\
 \langle \xi | \hat{\psi}_{m_1}^\dagger(\mathbf{r}_1) \hat{\psi}_{m_2}^\dagger(\mathbf{r}_2) \hat{\psi}_{m_3}(\mathbf{r}_3) \hat{\psi}_{m_4}(\mathbf{r}_4) | \xi \rangle &= \left(1 - \frac{1}{N}\right) \psi_{m_1}^*(\mathbf{r}_1) \psi_{m_2}^*(\mathbf{r}_2) \psi_{m_3}(\mathbf{r}_3) \psi_{m_4}(\mathbf{r}_4).
 \end{aligned} \tag{2.18}$$

The expectation value of the field operator vanishes but the experimentally observable correlation functions are non-zero, which makes this mean-field construct particularly important as it becomes a number-conserving theory [83]. Using the mean-field construct one arrives at Eq.2.18, which will be used to get the mean-field approximated Hamiltonian from the second-quantized Hamiltonian that was constructed in the last section. From the mean-field Hamiltonian, one can get to the GP equations, which we will see in the next section.

2.3 Gross-Pitaevskii equation

Using the mean-field theory one can replace the Hamiltonian, comprising of the interacting (Eq.2.6) and non-interacting parts (Eq.2.2), with its expectation value,

$$\begin{aligned}
 \langle \xi | \hat{\mathcal{H}} | \xi \rangle = E[\psi] = \int d\mathbf{r} \left[\sum_{m, m'=-1}^1 \psi_m^*(\mathbf{r}) \left(-\frac{\hbar^2}{2M} \nabla^2 + U(\mathbf{r}) - p m + q m^2 \right) \psi_m(\mathbf{r}) \right. \\
 \left. + \frac{c_0}{2} n^2(\mathbf{r}) + \frac{c_1}{2} |\mathbf{F}(\mathbf{r})|^2 \right],
 \end{aligned} \tag{2.19}$$

where the $1/N$ term in Eq.2.18 is neglected assuming that the number of condensate particles, N , is very large. The number- and spin-density expectation values follow from Eq.2.7-2.8,

$$\begin{aligned}
 n(\mathbf{r}) &= \langle \xi | \hat{n}(\mathbf{r}) | \xi \rangle = \sum_{m=-1}^1 \psi_m^*(\mathbf{r}) \psi_m(\mathbf{r}) \\
 F_i(\mathbf{r}) &= \langle \xi | \hat{F}_i(\mathbf{r}) | \xi \rangle = \sum_{m, m'=-1}^1 \psi_m^*(\mathbf{r}) (f_i)_{mm'} \psi_{m'}(\mathbf{r}),
 \end{aligned} \tag{2.20}$$

where $(f_i)_{mm'}$ is the mm' element of the $i = (x, y, z)$ spin-1 Pauli matrices (Eq.2.3). One can get to the Gross-Pitaevskii (GP) equation that dictates the dynamics of the mean

fields $(\psi_m(\mathbf{r}, t))$ from the energy functional Eq.2.19 [83],

$$\begin{aligned} i\hbar \frac{\partial \psi_m(\mathbf{r}, t)}{\partial t} &= \frac{\delta E[\psi]}{\delta \psi_m^*(\mathbf{r}, t)} \\ &= \left(-\frac{\hbar^2}{2M} \nabla^2 + U(\mathbf{r}) - p m + q m^2 \right) \psi_m(\mathbf{r}, t) \\ &\quad + c_0 n(\mathbf{r}, t) \psi_m(\mathbf{r}, t) + c_1 \sum_{m'=-1}^1 \mathbf{F}(\mathbf{r}, t) \cdot \mathbf{f}_{mm'} \psi_{m'}(\mathbf{r}, t). \end{aligned} \quad (2.21)$$

This time-dependent GP equation is a set of three coupled equations corresponding to the elements of the vector order parameter, i.e., $\psi_1(\mathbf{r}, t)$, $\psi_0(\mathbf{r}, t)$, and $\psi_{-1}(\mathbf{r}, t)$, which are the time-dependent wave functions for three possible Zeeman projections.

2.4 Stationary states and Phase Diagram in absence of trapping

The time-dependent wave function can be written as a combination of a time-independent part and a time-dependent part following the ansatz,

$$\psi_m(\mathbf{r}, t) = \psi_m(\mathbf{r}) \exp\left(-\frac{i\mu t}{\hbar}\right), \quad (2.22)$$

where μ is the chemical potential. The GP equation Eq.2.21 can be further simplified following this ansatz, which yields three coupled time-independent GP equations,

$$\left(-\frac{\hbar^2}{2M} \nabla^2 + U(\mathbf{r}) - p + q - \mu + c_0 n(\mathbf{r}) + c_1 F_z(\mathbf{r}) \right) \psi_1(\mathbf{r}) + \frac{c_1}{\sqrt{2}} F_-(\mathbf{r}) \psi_0(\mathbf{r}) = 0, \quad (2.23)$$

$$\left(-\frac{\hbar^2}{2M} \nabla^2 + U(\mathbf{r}) - \mu + c_0 n(\mathbf{r}) \right) \psi_0(\mathbf{r}) + \frac{c_1}{\sqrt{2}} F_-(\mathbf{r}) \psi_{-1}(\mathbf{r}) + \frac{c_1}{\sqrt{2}} F_+(\mathbf{r}) \psi_1(\mathbf{r}) = 0, \quad (2.24)$$

$$\left(-\frac{\hbar^2}{2M} \nabla^2 + U(\mathbf{r}) + p + q - \mu + c_0 n(\mathbf{r}) - c_1 F_z(\mathbf{r}) \right) \psi_{-1}(\mathbf{r}) + \frac{c_1}{\sqrt{2}} F_+(\mathbf{r}) \psi_0(\mathbf{r}) = 0, \quad (2.25)$$

where $F_z(\mathbf{r}) = |\psi_1(\mathbf{r})|^2 - |\psi_{-1}(\mathbf{r})|^2$, and the function $F_{\pm}(\mathbf{r})$ follows the usual definition,

$$\begin{aligned} F_+(\mathbf{r}) &= F_x(\mathbf{r}) + iF_y(\mathbf{r}) = \sqrt{2} \left[\psi_1^*(\mathbf{r}) \psi_0(\mathbf{r}) + \psi_0^*(\mathbf{r}) \psi_{-1}(\mathbf{r}) \right], \\ F_-(\mathbf{r}) &= F_x(\mathbf{r}) - iF_y(\mathbf{r}) = \sqrt{2} \left[\psi_1(\mathbf{r}) \psi_0^*(\mathbf{r}) + \psi_0(\mathbf{r}) \psi_{-1}^*(\mathbf{r}) \right]. \end{aligned} \quad (2.26)$$

The time-independent GP equations can be solved to get the possible stationary states and the energy and other parameters characterizing the stationary states. A simple situation can be in the absence of confinement, $U(\mathbf{r}) = 0$. In such a situation, the system will have a constant number density (homogeneous) and thus, one can ignore the kinetic energy term as well. Note that, in the next chapter, we will derive all the details of the stationary states in a more realistic condition, that is in the presence of the trapping potential. So, for brevity, we will not include the detailed derivations of the standard results of homogeneous condensate. We list the results of the homogeneous condensate in the following.

In the absence of trapping, there can be a total of five possible stationary states. There can be two ferromagnetic states, one with all the atoms in the $m = 1$ spin projection (let us call it (1,0,0)), and another with all the atoms in $m = -1$ denoted as (0,0,1). The stationary state for which all the atoms are in $m = 0$ is known as the polar state, which is denoted as (0,1,0). The other two states are the anti-ferromagnetic state denoted as (1,0,1), for which $m = 0$ spin projection is empty with the other two filled, and another stationary state with all the spin projections populated or (1,1,1) state. The reason for such a notation for the stationary states will be discussed later in the next chapter.

States	chemical potential	energy desity
(1,0,0) <i>Ferro1</i>	$c_0n - p + q + c_1n$	$\frac{1}{2}c_0n^2 - pn + qn + \frac{1}{2}c_1n^2$
(0,1,0) <i>Polar</i>	c_0n	$\frac{1}{2}c_0n^2$
(0,0,1) <i>Ferro2</i>	$c_0n + p + q + c_1n$	$\frac{1}{2}c_0n^2 + pn + qn + \frac{1}{2}c_1n^2$
(1,0,1) <i>Anti</i> – <i>Ferro</i>	$c_0n + q$	$\frac{1}{2}c_0n^2 + qn - \frac{p^2}{2c_1}$
(1,1,1)	$c_0n + c_1n - \frac{(p^2 - q^2)}{2q}$	$\frac{1}{2}c_0n^2 + \frac{(q^2 - p^2 + 2qc_1n)^2}{8c_1q^2}$

Table 2.1: The energy and chemical potential for the possible stationary states for spin-1 condensates in the absence of trapping.

The detailed derivation for the stationary states for the homogeneous spinor condensate is given in [83]. We summarize the energy density and the chemical potential corresponding to all the stationary states in Table 2.1. Note that the linear and the quadratic Zeeman terms can be tuned independently, which we have discussed previously. So, by comparing the energy of the stationary states, one can draw a set of phase diagrams of the condensate ground states in the (q, p) parameter space which are shown in Fig.2.1.

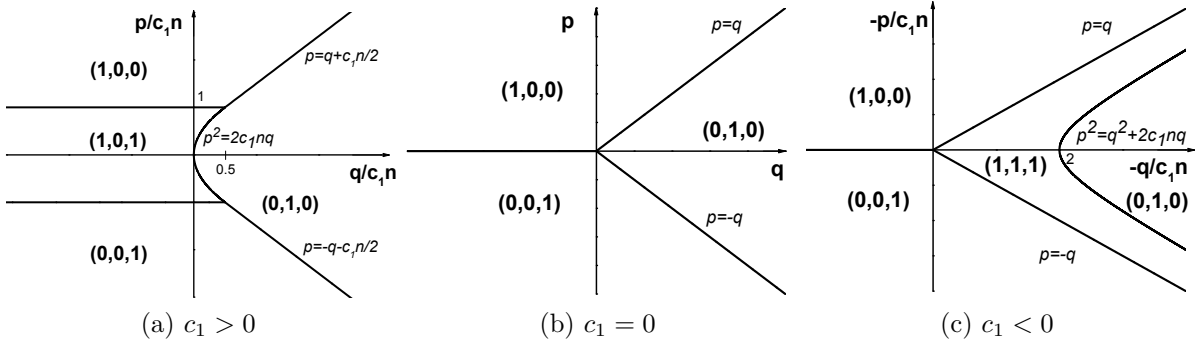


Figure 2.1: Phase diagram in (q, p) parametric space of a spin-1 BEC in absence of any confinement with (a) anti-ferromagnetic ($c_1 > 0$), (b) absent ($c_1 = 0$), and (c) ferromagnetic ($c_1 < 0$) spin-dependent interaction. The linear and quadratic Zeeman term is represented as p and q respectively.

For an anti-ferromagnetic type of spin-spin interaction, the ferromagnetic, polar, and anti-ferromagnetic states become the ground state for different parameter regions depending on the strength of p and q values (Fig.2.1(a)). The phase transition between the anti-ferromagnetic to ferromagnetic state(s) is of second-order in nature in the sense that the first derivative of energy with respect to p changes in a continuous manner across the phase boundary [83]. Across other transition boundaries for this case, the first derivative of energy with respect to p and q change abruptly. In the absence of the spin-dependent interaction (Fig.2.1(b)), only the polar state and the ferromagnetic states become the ground state. For positive values of the quadratic Zeeman term, the polar state becomes the ground state in the region where $|q| > |p|$. The ferromagnetic state $(1,0,0)$ is preferred to become the ground state if the linear term is positive and the other ferromagnetic state $(0,0,1)$ becomes the ground state for negative values of the linear Zeeman term. For all the possible phase transitions in this case, the first derivative of energy with respect to p and q changes discontinuously across the phase boundaries. If the spin-spin interaction is of the ferromagnetic type ($c_1 < 0$), the $(1,1,1)$ state becomes the ground state for a range of positive values of p and q (Fig.2.1(c)). Other than this state, the ferromagnetic states

or the polar state are favored to become the ground state for different regions of the (q, p) parameter space. Note that the first derivative of total energy with respect to p changes abruptly across the phase boundaries between the ferromagnetic state ($p = 0$ line), while the same changes smoothly across the other phase boundaries shown in Fig.2.1(c). In that sense, the phase transition between the PM to polar or PM to ferromagnetic states are second-order phase transition for a homogeneous condensate [83].

Interesting to note that, one can have a phase transition between the polar and ferromagnetic states for the anti-ferromagnetic type of spin interaction, as can be seen in Fig.2.1(a). But, a similar phase transition does not happen when the spin interaction is of ferromagnetic type (Fig.2.1(c)). The number density n , for a homogeneous condensate, can be treated as a free parameter, which is used to scale the linear and quadratic terms in Fig.2.1(a) and Fig.2.1(c). The situation would be different for a trapped condensate where the number density varies over space.

In the next and subsequent chapters, we will focus on the realistic situation of the condensate under confinement. The energy and the phase diagram given in this section are important in the sense that they can be compared with the results that we will get in the subsequent chapters, to apprehend the contrast between the trapped and untrapped scenario.

Chapter 3

Domain formation in a trapped spin-1 BEC

In the previous chapter, we discussed the basic formalism of mean-field theory for spin-1 BEC, from which we got to the Gross-Pitaevskii equation. From the time-independent GP equation, the stationary states were obtained in the absence of trapping. Energy densities of the stationary states revealed phase diagrams in (q, p) parameter space, under the assumption of a constant number density for all the stationary states.

However, in a realistic scenario, the BEC is formed inside a confining potential, which is, in general, harmonic and unless the potential is switched off, there is no way to neglect the trapping. The constant number density assumption is thus invalid, as the trapping geometry dictates the number density of the condensate. However, the GP equation being non-linear, it is difficult to find the density profile in the presence of derivatives. In this chapter, we investigate the stationary state structures in the presence of generic trapping. We employ the Thomas-Fermi approximation that is typically valid for condensates with large enough density to neglect the kinetic energy contribution compared to the interaction energies. Under this approximation, we find out the energy density profile for each stationary state as a function of space. This would allow us to compare the energy densities of all the stationary states locally, which is required to understand possible domain formation scenarios. We would use terms like 'phase separation' or 'phase-coexistence' or 'domain formation' equivalently in what follows.

Phase separation over space of multi-component BEC under trapping was theoretically investigated by Timmermans [95] who named it "potential separation", as opposed to the phase separation which does not require any external fields. A common example of phase separation that does not require any external field is oil-water separation. In contrast, fluids of different specific weights undergo a phase separation which is the "potential separation", that requires the presence of external fields, e.g., the gravitational field. In an optically trapped sodium spinor condensate, spin domain formation was reported by Stenger et. al., [49] which was followed by a detailed theoretical justification by Isoshima et. al., [99]. Since then, it has been an active area of interest to understand the spin domain formation of trapped spin-1 condensate [96, 100, 101, 114], even at zero magnetic fields [115, 116]. The spinor condensate is not unique when it comes to phase separation, it has also been observed in binary condensates where the interplay between intra- and inter-species interaction is responsible for this phenomenon [97, 98, 102, 104–107, 109, 110, 112, 117]. The instability induced phase separation in spin-orbit coupled condensates [103, 108, 111, 118] has also attracted a lot of attention in recent years.

To get to the spin domain formation in the ground state of a spinor BEC, the Thomas-Fermi (T-F) approximation has been extensively used in literature [54, 99, 102, 104, 119] on a case to case basis. The analytical ease that the T-F approximation provides is a reasonable first step to understand phase separation under entrapment when the trap size is bigger than the healing length [114]. While the domain formation studies have been mainly carried out on a case-by-case basis, in this chapter, we will show that under the essential constraint of constant chemical potential, the GP dynamics in T-F approximation is capable of capturing the full spectrum of possible phase-coexistence scenarios in a unified manner, for any trapping geometry.

3.1 Stationary states in the presence of trapping potential

One needs to know the details of all the possible stationary states to get to the ground state structure under given conditions. The solution of the time-independent GP equation Eq.2.23-2.25 provides all the necessary details of the stationary states. In presence of a

generic trapping potential $U(\mathbf{r})$ we follow the ansatz,

$$\psi_m(\mathbf{r}) = \sqrt{n_m(\mathbf{r})} \exp(-i\theta_m) \exp\left(\frac{-i\mu t}{\hbar}\right), \quad (3.1)$$

where the real part of the mean-field corresponds to the sub-component density. The chemical potential μ and the individual phase θ_m constitute the imaginary part of it. By stationary state, we mean here the stationarity of $n_m(\mathbf{r})$, where the phase oscillation due to the chemical potential is always present. One does not consider here the spatial dependence of θ_m as well, because that will result in velocity, which will go against the stationarity of phase.

Following this ansatz, one can equate the real and the imaginary part of each time-dependent GP equation separately. The imaginary part (plugging in the ansatz Eq.3.1 in the GP equation given in Eq.2.21) produces the evolution equations of the sub-component number densities, which are the amplitude of the mean-fields,

$$\dot{n}_0(\mathbf{r}) = -\frac{4c_1 n_0 \sqrt{n_1 n_{-1}} \sin \theta_r}{\hbar}, \quad (3.2)$$

$$\dot{n}_{\pm 1}(\mathbf{r}) = \frac{2c_1 n_0 \sqrt{n_1 n_{-1}} \sin \theta_r}{\hbar}, \quad (3.3)$$

where the θ_r is the relative phase defined as, $\theta_r = \theta_1 + \theta_{-1} - 2\theta_0$. For a stationary state, the sub-component densities do not change with time, so the temporal derivatives on the left side of the equations are zero. If the spin-spin interaction is absent (i.e., $c_1 = 0$), these equations are trivially satisfied. But in the presence of spin-spin interaction (i.e., $c_1 \neq 0$), for stationary states, at least one of the sub-components has to be empty (i.e., n_1 or n_0 or n_{-1} is zero). On the other hand, if all the sub-components are filled then $\sin \theta_r = 0$ must be satisfied, which implies that the relative phase should be 0 or π . The stationary state where all the sub-components are filled with the relative phase $\theta_r = 0$ is called the phase-matched (PM) state and the same with $\theta_r = \pi$ is called the anti-phase-matched (APM) state. In what follows, we will represent the stationary states as $(\mathbf{n}_1, \mathbf{n}_0, \mathbf{n}_{-1})$, where \mathbf{n}_m is the placeholder for the binary notation, 0 or 1. If the sub-component is populated we represent it as 1, and 0 if it is empty. In this notation, for example, the anti-ferromagnetic state is represented as $(1, 0, 1)$ where the sub-components corresponding to $m = 1$ and $m = -1$ are populated.

Similarly, the phase dynamics equations are obtained from the real part of the time-dependent GP equation following the same ansatz,

$$\hbar\sqrt{n_0(\mathbf{r})}\dot{\theta}_0 = \left(-\frac{\hbar^2\nabla^2}{2M} + U(\mathbf{r}) + c_0n - \mu \right) \sqrt{n_0(\mathbf{r})} + c_1\sqrt{n_0(\mathbf{r})}(n_1 + n_{-1} + 2\sqrt{n_{-1}n_1}\cos\theta_r), \quad (3.4)$$

$$\begin{aligned} \hbar\sqrt{n_{\pm 1}(\mathbf{r})}\dot{\theta}_{\pm 1} = & \left(-\frac{\hbar^2\nabla^2}{2M} + U(\mathbf{r}) + c_0n - \mu + q \mp p \right) \sqrt{n_{\pm 1}(\mathbf{r})} \pm c_1\sqrt{n_{\pm 1}(\mathbf{r})}(n_1 - n_{-1}) \\ & + c_1n_0 \left(\sqrt{n_{\pm 1}(\mathbf{r})} + \sqrt{n_1(\mathbf{r})n_{-1}(\mathbf{r})}\cos\theta_r \right). \end{aligned} \quad (3.5)$$

Here, we have assumed that the phases have negligible variations over space. The spatial variation is significant in vortex solutions. But, in what follows, we are not considering any vortex solution. Now, assuming that the sub-components are populated, one can re-write the corresponding phase equations as

$$\hbar\dot{\theta}_0 = \frac{1}{\sqrt{n_0(\mathbf{r})}} \left(-\frac{\hbar^2\nabla^2}{2M} + U(\mathbf{r}) + c_0n - \mu \right) \sqrt{n_0(\mathbf{r})} + c_1(n_1 + n_{-1} + 2\sqrt{n_{-1}n_1}\cos\theta_r), \quad (3.6)$$

$$\begin{aligned} \hbar\dot{\theta}_{\pm 1} = & \frac{1}{\sqrt{n_{\pm 1}(\mathbf{r})}} \left(-\frac{\hbar^2\nabla^2}{2M} + U(\mathbf{r}) + c_0n - \mu \right) \sqrt{n_{\pm 1}(\mathbf{r})} \pm c_1(n_1 - n_{-1}) + q \mp p \\ & + c_1n_0 \left(1 + \sqrt{\frac{n_{\mp 1}(\mathbf{r})}{n_{\pm 1}(\mathbf{r})}} \cos\theta_r \right). \end{aligned} \quad (3.7)$$

Having known the structure of the stationary states from the density dynamics equations Eq.3.2-3.3, one can solve the phase equations under the stationarity conditions that reveals the sub-component density profiles over space. The same ansatz also simplifies the energy expression given in Eq.2.19,

$$\begin{aligned} E = & \int d\mathbf{r} e(\mathbf{r}) \\ = & \int d\mathbf{r} \left[-\sum_{m=-1}^1 \sqrt{n_m(\mathbf{r})} \frac{\hbar^2\nabla^2}{2M} \sqrt{n_m(\mathbf{r})} + U(\mathbf{r})n(\mathbf{r}) - p(n_1 - n_{-1}) + q(n_1 + n_{-1}) \right. \\ & \left. + \frac{c_0}{2}n^2(\mathbf{r}) + \frac{c_1}{2}(n_1 - n_{-1})^2 + c_1n_0(n_1 + n_{-1} + 2\sqrt{n_1n_{-1}}\cos\theta_r) \right], \end{aligned} \quad (3.8)$$

where $e(\mathbf{r})$ is the energy density. Plugging the expressions of sub-component densities in the above equation, one can get to energy density and the total energy corresponding to each stationary state.

To get a detailed picture of the possible stationary states under confinement, one has to solve the phase equations Eq.3.6-3.7. For that, one can use the Thomas-Fermi approximation, where it is assumed that the number of particles present in the condensate is so large that the interaction energy is much bigger than the kinetic energy.

3.1.1 Single-component states

The stationary state where only one of the sub-components is populated and the other two are empty are termed as a single-component state. There are a total of three possible single-component states, the polar state is the one where the $m = 0$ component is populated only. The other two are the ferromagnetic stationary states. Among the ferromagnetic states, if $m = 1$ is populated and the other two are empty, we denote it as F1 or (1,0,0) and if $m = -1$ is only populated, this is denoted as (0,0,1) or F2.

Ferromagnetic state F1 or (1,0,0) state

For this stationary state, the phase equation Eq.3.7 corresponding to $\dot{\theta}_1$ under the stationarity condition reads,

$$\begin{aligned} \hbar\dot{\theta}_1 = 0 = \frac{1}{\sqrt{n_1(\mathbf{r})}} \left(-\frac{\hbar^2\nabla^2}{2M} + U(\mathbf{r}) + c_0n - \mu \right) \sqrt{n_1(\mathbf{r})} + c_1(n_1 - n_{-1}) + q - p \\ + c_1n_0 \left(1 + \sqrt{\frac{n_{-1}(\mathbf{r})}{n_1(\mathbf{r})}} \cos \theta_r \right). \end{aligned} \quad (3.9)$$

In this state, only the n_1 component is populated, with $n_0 = n_{-1} = 0$. As a result, $n_1 = n$, where n is the total number density. Under the T-F approximation, the kinetic energy term can be neglected, and the solution provides the number density,

$$n(\mathbf{r}) = n_1(\mathbf{r}) = \frac{\mu + p - q - U(\mathbf{r})}{c_0 + c_1}. \quad (3.10)$$

This can be used to get the T-F approximated energy density (neglecting the first term in the energy density expression given in Eq.3.8) of this stationary state,

$$\begin{aligned} e_{F1}^{TF}(\mathbf{r}) &= (U(\mathbf{r}) - p + q)n(\mathbf{r}) + \frac{c_0}{2}n^2(\mathbf{r}) + \frac{c_1}{2}n^2(\mathbf{r}) \\ &= (U(\mathbf{r}) - p + q) \left(\frac{\mu + p - q - U(\mathbf{r})}{c_0 + c_1} \right) + \frac{(\mu + p - q - U(\mathbf{r}))^2}{2(c_0 + c_1)}. \end{aligned} \quad (3.11)$$

The spatial variation of the T-F approximated energy density is only dictated by the trapping potential.

Ferromagnetic state F2 or (0,0,1) state

For this state, only the n_{-1} is populated thus, $n_{-1} = n$, where n is the total density. Under the T-F approximation the phase equation for $\dot{\theta}_{-1}$ can be solved using stationarity condition to get the spatial variation of the number density,

$$n(\mathbf{r}) = n_{-1}(\mathbf{r}) = \frac{\mu - p - q - U(\mathbf{r})}{c_0 + c_1}. \quad (3.12)$$

Using this number density expression one can get to the energy density for this stationary state,

$$\begin{aligned} e_{F2}^{TF}(\mathbf{r}) &= (U(\mathbf{r}) + p + q)n(\mathbf{r}) + \frac{c_0}{2}n^2(\mathbf{r}) + \frac{c_1}{2}n^2(\mathbf{r}) \\ &= (U(\mathbf{r}) + p + q) \left(\frac{\mu - p - q - U(\mathbf{r})}{c_0 + c_1} \right) + \frac{(\mu - p - q - U(\mathbf{r}))^2}{2(c_0 + c_1)}. \end{aligned} \quad (3.13)$$

Note that, the difference between the number- and energy density of the ferromagnetic states is the sign of the linear Zeeman term p , which can be positive or negative depending on the direction of the magnetic field. It is only natural that the direction of the magnetic field will favor one of the ferromagnetic states.

Polar state

The polar state is a single-component state, where $n_0 \neq 0$ and the other two sub-components are empty i.e., $n_{\pm 1} = 0$. Imposing stationarity condition, the T-F approxi-

mated Eq.3.6 provides the number density expression,

$$n_0(\mathbf{r}) = n(\mathbf{r}) = \frac{\mu - U(\mathbf{r})}{c_0}. \quad (3.14)$$

The energy density for this stationary state is,

$$\begin{aligned} e_{Pol}^{TF}(\mathbf{r}) &= U(\mathbf{r})n(\mathbf{r}) + \frac{c_0}{2}n^2(\mathbf{r}) \\ &= U(\mathbf{r})\left(\frac{\mu - U(\mathbf{r})}{c_0}\right) + \frac{(\mu - U(\mathbf{r}))^2}{2c_0}. \end{aligned} \quad (3.15)$$

3.1.2 Multi-component states

If more than one sub-components are populated, the stationary state can be classified as a multi-component state. There are a total of five possible multi-component states for this spin-1 case. Out of these, there can be three stationary states for which two sub-components are populated while one of the components is empty. This is the case for the anti-ferromagnetic state and the two possible mixed-ferromagnetic states (1,1,0) and (0,1,1). The other possibility is when all three components are populated, which is the case for the PM and the APM state.

Anti-ferromagnetic (AF) state or (1,0,1)

In this stationary state, the $m = 0$ component is empty and the other two components are occupied, i.e. $n_0 = 0$ and $n_{\pm 1} \neq 0$. So, the phase equations corresponding to $\dot{\theta}_1$ and $\dot{\theta}_{-1}$ under the T-F approximation are,

$$U(\mathbf{r}) + c_0 n - \mu + c_1(n_1 - n_{-1}) + q - p = 0 \quad (\text{corresponding to } \dot{\theta}_1), \quad (3.16a)$$

$$U(\mathbf{r}) + c_0 n - \mu - c_1(n_1 - n_{-1}) + q + p = 0 \quad (\text{corresponding to } \dot{\theta}_{-1}), \quad (3.16b)$$

which can be solved to get to the sub-component densities $n_{\pm 1}$. Firstly, the summation of these two equations yields the total number density,

$$n(\mathbf{r}) = \frac{\mu - q - U(\mathbf{r})}{c_0}. \quad (3.17)$$

Now subtracting Eq.3.16b from Eq.3.16a one can get the magnetization density, i.e.,

$$n_1 - n_{-1} = \frac{p}{c_1}. \quad (3.18)$$

The total number density is the sum of the sub-component densities, i.e., $n(\mathbf{r}) = n_1 + n_{-1}$. Now using the total number density and the magnetization density, one can write the sub-component densities as

$$n_1(\mathbf{r}) = \frac{\mu - q - U(\mathbf{r})}{2c_0} + \frac{p}{2c_1}, \quad (3.19a)$$

$$n_{-1}(\mathbf{r}) = \frac{\mu - q - U(\mathbf{r})}{2c_0} - \frac{p}{2c_1}. \quad (3.19b)$$

The corresponding energy density for this stationary state is

$$\begin{aligned} e_{AF}^{TF}(\mathbf{r}) &= U(\mathbf{r})n(\mathbf{r}) + qn(\mathbf{r}) + \frac{c_0}{2}n^2(\mathbf{r}) - \frac{p^2}{2c_1} \\ &= \left(U(\mathbf{r}) + q \right) \left(\frac{\mu - q - U(\mathbf{r})}{c_0} \right) + \frac{(\mu - q - U(\mathbf{r}))^2}{2c_0} - \frac{p^2}{2c_1}. \end{aligned} \quad (3.20)$$

Mixed-ferromagnetic state: MF1 or (1,1,0)

If the sub-components corresponding to the Zeeman projections $m = 0$ and $m = 1$ are only populated with $m = -1$ sub-component being empty ($n_{-1} = 0$), the stationary state is of the mixed-ferromagnetic type represented as (1,1,0). For this stationary state, the phase equations corresponding to $\dot{\theta}_1$ and $\dot{\theta}_0$ under the T-F approximation read,

$$U(\mathbf{r}) + c_0n - \mu + c_1n_1 + q - p + c_1n_0 = 0 \quad (\text{corresponding to } \dot{\theta}_1), \quad (3.21a)$$

$$U(\mathbf{r}) + c_0n - \mu + c_1n_1 = 0 \quad (\text{corresponding to } \dot{\theta}_0). \quad (3.21b)$$

The total number density for this state, $n(\mathbf{r}) = n_1(\mathbf{r}) + n_0(\mathbf{r})$. Using this relation in Eq.3.21a, the total number density expression is obtained as

$$n(\mathbf{r}) = \frac{\mu + p - q - U(\mathbf{r})}{c_0 + c_1}. \quad (3.22)$$

Now, Eq.3.21b can be rewritten as,

$$U(\mathbf{r}) + c_0n - \mu + c_1(n - n_0) = 0, \quad (3.23)$$

where the total density expression (Eq.3.22) can be plugged in, which yields the sub-component density expressions

$$n_0(\mathbf{r}) = \frac{p - q}{c_1}, \quad (3.24a)$$

$$n_1(\mathbf{r}) = \frac{\mu + p - q - U(\mathbf{r})}{c_0 + c_1} - \frac{p - q}{c_1}. \quad (3.24b)$$

Using these expressions the energy density can be easily obtained as

$$\begin{aligned} e_{MF1}^{TF}(\mathbf{r}) &= U(\mathbf{r})n(\mathbf{r}) - pn_1 + qn_1 + \frac{c_0}{2}n^2(\mathbf{r}) + \frac{c_1}{2}n_1^2 + c_1n_0n_1 \\ &= U(\mathbf{r})\frac{(\mu + p - q - U(\mathbf{r}))}{c_0 + c_1} + \frac{c_0(\mu + p - q - U(\mathbf{r}))^2}{2(c_0 + c_1)^2} \\ &\quad + \frac{c_1}{2}\left(\frac{\mu + p - q - U(\mathbf{r})}{c_0 + c_1} - \frac{p - q}{c_1}\right)^2. \end{aligned} \quad (3.25)$$

Mixed-ferromagnetic state: MF2 or (0,1,1)

For this stationary state, $n_1(\mathbf{r}) = 0$, and the other two components are populated. The phase equations corresponding to the filled components under the T-F approximation

$$U(\mathbf{r}) + c_0n - \mu + c_1n_{-1} + q + p + c_1n_0 = 0 \quad (\text{corresponding to } \dot{\theta}_{-1}), \quad (3.26a)$$

$$U(\mathbf{r}) + c_0n - \mu + c_1n_{-1} = 0 \quad (\text{corresponding to } \dot{\theta}_0), \quad (3.26b)$$

can be solved to get to the total number and sub-component density distributions. The sub-component densities can be added to get total density i.e., $n(\mathbf{r}) = n_0(\mathbf{r}) + n_{-1}(\mathbf{r})$. Following the similar approach as discussed for the case MF1 state, one obtains

$$n(\mathbf{r}) = \frac{\mu - p - q - U(\mathbf{r})}{c_0 + c_1}, \quad (3.27a)$$

$$n_0(\mathbf{r}) = \frac{-p - q}{c_1}, \quad (3.27b)$$

$$n_{-1}(\mathbf{r}) = \frac{\mu - p - q - U(\mathbf{r})}{c_0 + c_1} + \frac{p + q}{c_1}. \quad (3.27c)$$

The energy density for this state is

$$\begin{aligned}
e_{MF2}^{TF}(\mathbf{r}) &= U(\mathbf{r})n(\mathbf{r}) + pn_{-1} + qn_{-1} + \frac{c_0}{2}n^2(\mathbf{r}) + \frac{c_1}{2}n_{-1}^2 + c_1n_0n_{-1} \\
&= U(\mathbf{r})\frac{(\mu - p - q - U(\mathbf{r}))}{c_0 + c_1} + \frac{c_0(\mu - p - q - U(\mathbf{r}))^2}{2(c_0 + c_1)^2} \\
&\quad + \frac{c_1}{2}\left(\frac{\mu - p - q - U(\mathbf{r})}{c_0 + c_1} + \frac{p + q}{c_1}\right)^2.
\end{aligned} \tag{3.28}$$

Just like the ferromagnetic states, the number- and the energy density of the mixed-ferromagnetic states only differ in the sign of the linear Zeeman term p .

Phase-matched (PM) state or (1,1,1) with $\theta_r = 0$

As discussed earlier, for a stationary state with all the sub-components occupied, the relative phase has to assume the value $\theta_r = 0$ or π . Such a stationary state corresponding to $\theta_r = 0$ is also known as the phase-matched (PM) state. In such a situation, the phase equations under T-F approximation reads

$$U(\mathbf{r}) + c_0n - \mu + c_1(n_1 + n_{-1} + 2\sqrt{n_{-1}n_1}) = 0, \tag{3.29a}$$

$$U(\mathbf{r}) + c_0n - \mu + c_1(n_1 - n_{-1}) + q - p + c_1n_0\left(1 + \sqrt{\frac{n_{-1}(\mathbf{r})}{n_1(\mathbf{r})}}\right) = 0, \tag{3.29b}$$

$$U(\mathbf{r}) + c_0n - \mu - c_1(n_1 - n_{-1}) + q + p + c_1n_0\left(1 + \sqrt{\frac{n_1(\mathbf{r})}{n_{-1}(\mathbf{r})}}\right) = 0, \tag{3.29c}$$

corresponding to $m = 0, 1, -1$ components. Now, to solve these equations, we can define a new parameter $k(\mathbf{r}) = \sqrt{\frac{n_1(\mathbf{r})}{n_{-1}(\mathbf{r})}}$ which simplifies these equations further as

$$\mu - c_0n - U(\mathbf{r}) = c_1n_{-1}(1 + k(\mathbf{r}))^2, \tag{3.30a}$$

$$U(\mathbf{r}) + c_0n - \mu + c_1n_{-1}(k^2(\mathbf{r}) - 1) + q - p + c_1n_0\left(1 + \frac{1}{k(\mathbf{r})}\right) = 0, \tag{3.30b}$$

$$U(\mathbf{r}) + c_0n - \mu - c_1n_{-1}(k^2(\mathbf{r}) - 1) + q + p + c_1n_0\left(1 + k(\mathbf{r})\right) = 0, \tag{3.30c}$$

where $k(\mathbf{r})$ is a positive quantity. As all the sub-components are populated in this state, this parameter cannot be zero, i.e, $k(\mathbf{r}) > 0$. Now, subtracting Eq.3.30b from Eq.3.30c, one can get the relation

$$-2c_1n_{-1}(k^2(\mathbf{r}) - 1) + 2p + c_1n_0\left(k(\mathbf{r}) - \frac{1}{k(\mathbf{r})}\right) = 0. \quad (3.31)$$

One can rearrange this equation to write the $n_0(\mathbf{r})$ component in terms of the $n_{-1}(\mathbf{r})$ and $k(\mathbf{r})$ as

$$c_1n_0 = \frac{2c_1n_{-1}(k^2(\mathbf{r}) - 1) - 2p}{k(\mathbf{r}) - \frac{1}{k(\mathbf{r})}}. \quad (3.32)$$

On the other hand, the addition of Eq.3.30b and Eq.3.30c leads to

$$2U(\mathbf{r}) + 2c_0n - 2\mu + 2q + c_1n_0\left(2 + k(\mathbf{r}) + \frac{1}{k(\mathbf{r})}\right) = 0, \quad (3.33)$$

which can also be rearranged to get to another expression of $n_0(\mathbf{r})$ as a function of the same $n_{-1}(\mathbf{r})$ and $k(\mathbf{r})$ as

$$\begin{aligned} c_1n_0 &= \frac{2k(\mathbf{r})(\mu - c_0n - U(\mathbf{r}) - q)}{(1 + k(\mathbf{r}))^2} \\ &= \frac{2k(\mathbf{r})(c_1n_{-1}(1 + k(\mathbf{r}))^2 - q)}{(1 + k(\mathbf{r}))^2}, \end{aligned} \quad (3.34)$$

where we have used the relation Eq.3.30a to write it in a more simplified form.

Now, equating the right side of Eq.3.32 and Eq.3.34,

$$\frac{(c_1n_{-1}(k^2(\mathbf{r}) - 1) - p)}{k^2(\mathbf{r}) - 1} = \frac{(c_1n_{-1}(1 + k(\mathbf{r}))^2 - q)}{(1 + k(\mathbf{r}))^2}, \quad (3.35)$$

which provides the allowed value of $k(\mathbf{r})$,

$$k(\mathbf{r}) = \frac{q + p}{q - p}, \quad (3.36)$$

while the other solution $k(\mathbf{r}) = -1$ is unphysical as this parameter is strictly positive

(by definition, $0 < k(\mathbf{r}) < \infty$). This also restricts the PM state in a region, $|q| > |p|$ in the (q, p) parameter space. As the total density is the sum of the sub-component densities, i.e., $n(\mathbf{r}) = n_1(\mathbf{r}) + n_0(\mathbf{r}) + n_{-1}(\mathbf{r})$, one can also write the n_0 component as, $n_0 = (n - (1 + k^2(\mathbf{r}))n_{-1})$. Now using this, Eq.3.32 can be rewritten as

$$c_1 \left(n - (1 + k^2(\mathbf{r}))n_{-1} \right) = \frac{2c_1 n_{-1} (k^2(\mathbf{r}) - 1) - 2p}{k(\mathbf{r}) - \frac{1}{k(\mathbf{r})}}, \quad (3.37)$$

which can be easily solved by using $k(\mathbf{r}) = \frac{q+p}{q-p}$ that yields the sub-component density $n_{-1}(\mathbf{r})$. Using the expression for $n_{-1}(\mathbf{r})$, the $n_0(\mathbf{r})$ can be obtained using Eq.3.34 and $n_1(\mathbf{r})$ from the relation, $n_1(\mathbf{r}) = k^2(\mathbf{r})n_{-1}(\mathbf{r})$. So, the sub-component densities of the PM state are

$$n_{-1}(\mathbf{r}) = \frac{(q-p)^2}{4q^2} \left(n(\mathbf{r}) + \frac{q^2 - p^2}{2c_1 q} \right), \quad (3.38a)$$

$$n_{+1}(\mathbf{r}) = \frac{(q+p)^2}{4q^2} \left(n(\mathbf{r}) + \frac{q^2 - p^2}{2c_1 q} \right), \quad (3.38b)$$

$$n_0(\mathbf{r}) = \frac{(q^2 - p^2)}{2q^2} \left(n(\mathbf{r}) - \frac{q^2 + p^2}{2c_1 q} \right), \quad (3.38c)$$

where $n(\mathbf{r})$ is the total density,

$$n(\mathbf{r}) = \frac{\mu - U(\mathbf{r}) + \frac{(p^2 - q^2)}{2q}}{(c_0 + c_1)}. \quad (3.39)$$

The energy density expression for this state can be easily found using the number density expressions,

$$\begin{aligned} e_{PM}^{TF}(\mathbf{r}) &= U(\mathbf{r})n(\mathbf{r}) - p(n_1 - n_{-1}) + q(n_1 + n_{-1}) + \frac{c_0}{2}n^2(\mathbf{r}) + \frac{c_1}{2}(n_1 - n_{-1})^2 \\ &\quad + c_1 n_0 (n_1 + n_{-1} + 2\sqrt{n_1 n_{-1}}) \\ &= U(\mathbf{r}) \left[\frac{k_1 - U(\mathbf{r})}{c_0 + c_1} \right] + \frac{c_0}{2} \left[\frac{k_1 - U(\mathbf{r})}{c_0 + c_1} \right]^2 + \frac{c_1}{2} \left[\frac{k_1 - U(\mathbf{r})}{c_0 + c_1} - \frac{p^2 - q^2}{2qc_1} \right]^2, \end{aligned} \quad (3.40)$$

where, $k_1 = \mu + \frac{(p^2 - q^2)}{2q}$.

Anti-phase-matched (APM) state or (1,1,1) with $\theta_r = \pi$

The stationary state corresponding to the relative phase $\theta_r = \pi$, with non-empty sub-components, is known as the APM state. For this state, we follow a similar strategy as used for the PM state to get the number and energy density expressions. The T-F approximated phase equations,

$$U(\mathbf{r}) + c_0 n - \mu + c_1(n_1 + n_{-1} - 2\sqrt{n_{-1}n_1}) = 0, \quad (3.41a)$$

$$U(\mathbf{r}) + c_0 n - \mu + c_1(n_1 - n_{-1}) + q - p + c_1 n_0 \left(1 - \sqrt{\frac{n_{-1}(\mathbf{r})}{n_1(\mathbf{r})}}\right) = 0, \quad (3.41b)$$

$$U(\mathbf{r}) + c_0 n - \mu - c_1(n_1 - n_{-1}) + q + p + c_1 n_0 \left(1 - \sqrt{\frac{n_1(\mathbf{r})}{n_{-1}(\mathbf{r})}}\right) = 0, \quad (3.41c)$$

can be simplified by introducing the parameter $k(\mathbf{r}) = \sqrt{\frac{n_1(\mathbf{r})}{n_{-1}(\mathbf{r})}}$,

$$\mu - c_0 n - U(\mathbf{r}) = c_1 n_{-1} (1 - k(\mathbf{r}))^2, \quad (3.42a)$$

$$U(\mathbf{r}) + c_0 n - \mu + c_1 n_{-1} (k^2(\mathbf{r}) - 1) + q - p + c_1 n_0 \left(1 - \frac{1}{k(\mathbf{r})}\right) = 0, \quad (3.42b)$$

$$U(\mathbf{r}) + c_0 n - \mu - c_1 n_{-1} (k^2(\mathbf{r}) - 1) + q + p + c_1 n_0 \left(1 - k(\mathbf{r})\right) = 0. \quad (3.42c)$$

The case when $k(\mathbf{r}) \neq 1$: Following the same procedure, first we add Eq.3.42b and Eq.3.42c,

$$2U(\mathbf{r}) + 2c_0 n - 2\mu + 2q - c_1 n_0 \left(k(\mathbf{r}) + \frac{1}{k(\mathbf{r})} - 2\right) = 0, \quad (3.43)$$

where Eq.3.42a can be used to get the relation between the sub-component $n_0(\mathbf{r})$ and $n_{-1}(\mathbf{r})$,

$$c_1 n_0 = 2k(\mathbf{r}) \frac{q - c_1 n_{-1} (1 - k(\mathbf{r}))^2}{(1 - k(\mathbf{r}))^2}, \quad (3.44)$$

To get to the above relation, we have assumed that $k(\mathbf{r}) \neq 1$. Similarly subtracting Eq.3.42b from Eq.3.42c one gets to

$$-2c_1 n_{-1} (k^2(\mathbf{r}) - 1) + 2p - c_1 n_0 \left(k(\mathbf{r}) - \frac{1}{k(\mathbf{r})}\right) = 0, \quad (3.45)$$

which can be rearranged to find another relation between $n_0(\mathbf{r})$ and $n_{-1}(\mathbf{r})$,

$$c_1 n_0 = 2k(\mathbf{r}) \frac{\left(p - c_1 n_{-1} (k^2(\mathbf{r}) - 1)\right)}{(k^2(\mathbf{r}) - 1)}. \quad (3.46)$$

Now equating the right side of the Eq.3.44 and Eq.3.46, one can rearrange and get to the relation

$$(p - q)k^2(\mathbf{r}) - 2pk(\mathbf{r}) + (p + q) = 0, \quad (3.47)$$

which leads to the solution for $k(\mathbf{r})$,

$$k(\mathbf{r}) = \frac{p + q}{p - q}, \quad (3.48)$$

while the other solution is $k(\mathbf{r}) = 1$. Note that, we have already considered $k(\mathbf{r}) \neq 1$. Now, one can rewrite Eq.3.44 by replacing the n_0 component as, $n_0(\mathbf{r}) = n(\mathbf{r}) - (1 + k^2(\mathbf{r}))n_{-1}(\mathbf{r})$ and then substituting $k(\mathbf{r})$ one can determine the $n_{-1}(\mathbf{r})$ component which in turn determines the other sub-component densities as well. For this state, the sub-component densities are

$$n_{-1}(\mathbf{r}) = \frac{(q - p)^2}{4q^2} \left(n(\mathbf{r}) + \frac{q^2 - p^2}{2c_1 q} \right), \quad (3.49a)$$

$$n_{+1}(\mathbf{r}) = \frac{(q + p)^2}{4q^2} \left(n(\mathbf{r}) + \frac{q^2 - p^2}{2c_1 q} \right), \quad (3.49b)$$

$$n_0(\mathbf{r}) = \frac{(q^2 - p^2)}{2q^2} \left(n(\mathbf{r}) - \frac{q^2 + p^2}{2c_1 q} \right), \quad (3.49c)$$

and the total density $n(\mathbf{r})$ comes out to be,

$$n(\mathbf{r}) = \frac{\mu - U(\mathbf{r}) + \frac{(p^2 - q^2)}{2q}}{(c_0 + c_1)}. \quad (3.50)$$

The energy density expression for this state can be easily found using the expressions of number density

$$\begin{aligned}
e_{APM}^{TF}(\mathbf{r}) &= U(\mathbf{r})n(\mathbf{r}) - p(n_1 - n_{-1}) + q(n_1 + n_{-1}) + \frac{c_0}{2}n^2(\mathbf{r}) + \frac{c_1}{2}(n_1 - n_{-1})^2 \\
&\quad + c_1n_0(n_1 + n_{-1} - 2\sqrt{n_1n_{-1}}) \quad (3.51) \\
&= U(\mathbf{r}) \left[\frac{k_1 - U(\mathbf{r})}{c_0 + c_1} \right] + \frac{c_0}{2} \left[\frac{k_1 - U(\mathbf{r})}{c_0 + c_1} \right]^2 + \frac{c_1}{2} \left[\frac{k_1 - U(\mathbf{r})}{c_0 + c_1} - \frac{p^2 - q^2}{2qc_1} \right]^2,
\end{aligned}$$

where, $k_1 = \mu + \frac{(p^2 - q^2)}{2q}$. Note that, the number density and the energy density expressions for the APM state are similar to that of the PM state. The only difference is that, due to the positivity of the parameter $k(\mathbf{r}) = \frac{p+q}{p-q}$, the APM state is restricted in the $|p| > |q|$ region of the (q, p) parameter space.

The case when $k(\mathbf{r}) = 1$: This condition is met when $n_1(\mathbf{r}) = n_{-1}(\mathbf{r})$ is satisfied, which also makes the magnetization density (defined as, $n_1(\mathbf{r}) - n_{-1}(\mathbf{r})$) to go to zero. For this condition the Eq.3.42a-3.42c can be written as

$$\mu - c_0n - U(\mathbf{r}) = 0, \quad (3.52a)$$

$$U(\mathbf{r}) + c_0n - \mu + q - p = 0, \quad (3.52b)$$

$$U(\mathbf{r}) + c_0n - \mu + q + p = 0. \quad (3.52c)$$

Now, Eq.3.52a itself, determines the total number density,

$$n(\mathbf{r}) = \frac{\mu - U(\mathbf{r})}{c_0}, \quad (3.53)$$

which imposes the condition that this case is only restricted to the situation (from the other two equations) when $p = 0$ and $q = 0$ (zero magnetic field). In this case, the $m = 1$ and $m = -1$ are equally populated. The energy density for this special case is,

$$\begin{aligned}
e_{APM}^{TF}(\mathbf{r}) \Big|_{n_1=n_{-1}, p=0, q=0} &= U(\mathbf{r})n(\mathbf{r}) + \frac{c_0}{2}n^2(\mathbf{r}) \\
&= U(\mathbf{r}) \left(\frac{\mu - U(\mathbf{r})}{c_0} \right) + \frac{(\mu - U(\mathbf{r}))^2}{2c_0}. \quad (3.54)
\end{aligned}$$

Note that for $p = 0$ and $q = 0$, the sub-component number densities of the APM state can be described by a one-parameter family of solutions. We will discuss the situation in Chapter 4 in a more detailed manner.

3.2 Domain formation possibilities:

In the last section, we have found all possible stationary states and their details regarding the number density distribution and associated energy density expressions. One can compare these energy density expressions that reveal which stationary state is energetically favored locally. This will reveal the domain-forming structures if any, but to ensure the stability of such domain structures, the chemical potential of the neighboring stationary states should be the same. So, under a single essential constraint of the constant chemical potential, one can compare the energy densities of all the stationary states to get to the domain structures.

3.2.1 In the absence of spin interaction

We will start with the simplest possible case, where the spin interaction is absent or negligibly present, i.e., $c_1 \simeq 0$. This is the situation sitting at the boundary of the two broad regimes namely $c_1 > 0$ (anti-ferromagnetic type of interaction) and $c_1 < 0$ (ferromagnetic type of spin interaction). We follow here the standard scheme of dividing the parameter regime of spin interactions as is done for the free condensate [83] to have a direct comparison (Fig.2.1). Note that, the stationary state structures that we have discussed so far are present when the spin interaction is present. For $c_1 = 0$, the right side of the Eq.3.2-3.3 become zero for any sub-component population, a necessary condition for the stationary states. Notice that one can relax the PM and APM phase criteria here. The phase equations Eq.3.6-3.7 for the stationary state under the T-F approximation become even simpler to solve for $c_1 \simeq 0$. Setting $c_1 = 0$, under the T-F approximation, one can now easily get the corresponding energy densities of the seven basic spin configurations following the similar analysis shown in the previous section. As an example, for the anti-ferromagnetic state n_0 component is empty, so for $c_1 \simeq 0$, the solution should obey the stationarity of the sub-component phases, i.e., $\dot{\theta}_{\pm 1} = 0$ (from Eq.3.7) resulting in,

$$U(\mathbf{r}) + c_0 n - \mu \mp p + q = 0, \quad (3.55)$$

when $n = n_1 + n_{-1}$. Thus, the T-F profile for the AF state in the absence of spin interaction would be,

$$c_0 n(\mathbf{r}) = \mu - q - U(\mathbf{r}), \quad (3.56)$$

when $p = 0$. Here $p = 0$ is the condition for the existence of this phase. Following the similar approach that we have already discussed in the previous section, one can get to the number density and energy density expressions, and also the parameter restrictions (if any) for all the stationary states for $c_1 = 0$ (summarized in Table 3.1).

States	Variation of density	Energy density	Restriction
(1,0,0) F1	$c_0 n(\mathbf{r}) = \mu + p - q - U(\mathbf{r})$	$e_1 = \frac{[U(\mathbf{r})-p+q][\mu+p-q-U(\mathbf{r})]}{c_0} + \frac{[\mu+p-q-U(\mathbf{r})]^2}{2c_0}$	<i>none</i>
(0,1,0) P	$c_0 n(\mathbf{r}) = \mu - U(\mathbf{r})$	$e_2 = \frac{U(\mathbf{r})[\mu-U(\mathbf{r})]}{c_0} + \frac{[\mu-U(\mathbf{r})]^2}{2c_0}$	<i>none</i>
(0,0,1) F2	$c_0 n(\mathbf{r}) = \mu - p - q - U(\mathbf{r})$	$e_3 = \frac{[U(\mathbf{r})+p+q][\mu-p-q-U(\mathbf{r})]}{c_0} + \frac{[\mu-p-q-U(\mathbf{r})]^2}{2c_0}$	<i>none</i>
(1,1,0)	$c_0 n(\mathbf{r}) = \mu - U(\mathbf{r})$	$e_4 = \frac{U(\mathbf{r})[\mu-U(\mathbf{r})]}{c_0} + \frac{[\mu-U(\mathbf{r})]^2}{2c_0}$	$p = q$
(1,0,1)	$c_0 n(\mathbf{r}) = \mu - q - U(\mathbf{r})$	$e_5 = \frac{[U(\mathbf{r})+q][\mu-q-U(\mathbf{r})]}{c_0} + \frac{[\mu-q-U(\mathbf{r})]^2}{2c_0}$	$p = 0$
(0,1,1)	$c_0 n(\mathbf{r}) = \mu - U(\mathbf{r})$	$e_6 = \frac{U(\mathbf{r})[\mu-U(\mathbf{r})]}{c_0} + \frac{[\mu-U(\mathbf{r})]^2}{2c_0}$	$p = -q$
(1,1,1)	$c_0 n(\mathbf{r}) = \mu - U(\mathbf{r})$	$e_7 = \frac{U(\mathbf{r})[\mu-U(\mathbf{r})]}{c_0} + \frac{[\mu-U(\mathbf{r})]^2}{2c_0}$	$p = q = 0$

Table 3.1: Number density and energy density of the stationary states at $c_1 = 0$. All the mixed states are restricted in p, q parameter states.

Note that, the restrictions present on the parameters corresponding to the last four

phases in Table 3.1, which are $p = q$, $p = 0$, $p = -q$, and $p = q = 0$ arise from the solutions of phase equations in the absence of spin interaction. An immediate consequence of these parameter restrictions is that, except for the case i.e. $p = q = 0$, the states $(1, 1, 0)$, $(1, 0, 1)$, and $(0, 1, 1)$ cannot exist together. So, there is no domain formation for these phases anywhere over the (q, p) parameter space except at the origin.

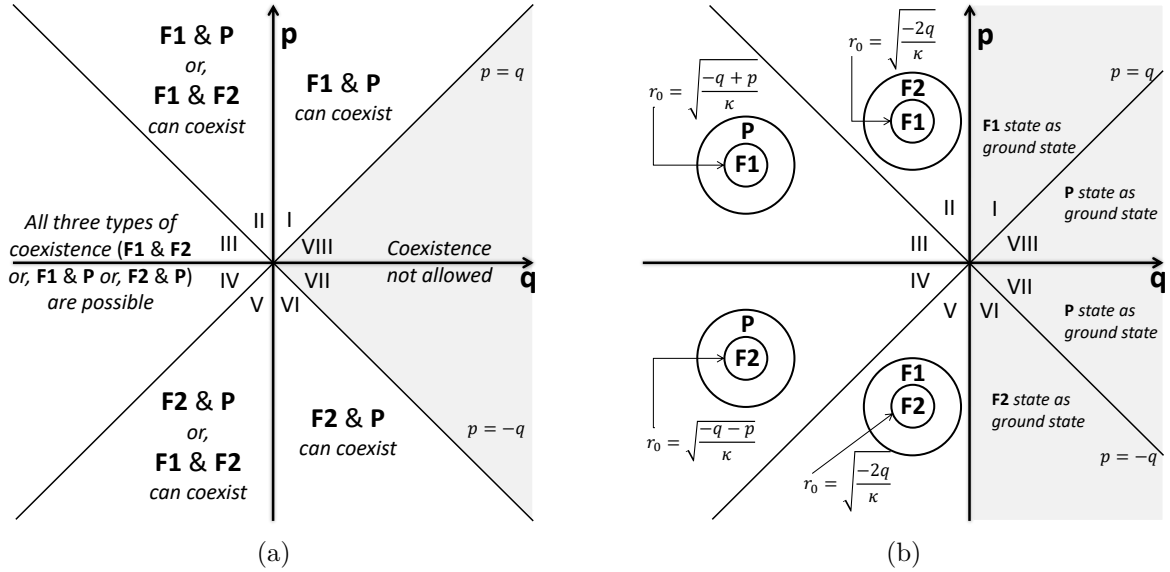


Figure 3.1: (a) Possibility of coexisting phases and domain formation in (q, p) parameter space of trapped spin-1 BEC for $c_1 = 0$. The states $(1, 0, 0)$, $(0, 0, 1)$ and $(0, 1, 0)$ are represented by $F1$, $F2$ and P for better visibility. Phase separation is not possible in the shaded region ($q > 0$ with $|q| > |p|$). (b) For a uniform two-dimensional harmonic trap, the distance (r_0) from the center of the trap where the phase separation occurs is shown schematically. For positive q (shaded region), no domain structure is found.

Fig.3.1(a) is a phase diagram showing the coexistence possibilities of the first three phases $(1, 0, 0)$, $(0, 1, 0)$ and $(0, 0, 1)$ in different regions of the on the qp -plane at $c_1 = 0$. This gives us a clear idea as to where on this phase diagram the domain formation can be expected, depending upon any particular form of the trapping potential $U(\mathbf{r})$, which is considered to be harmonic trapping in this context. The phases $(1, 1, 0)$ and $(0, 1, 1)$ can only exist along the diagonal lines $p = q$ and $p = -q$ respectively. The AF phase $(1, 0, 1)$ only exists along the q -axis, whereas $(1, 1, 1)$ can exist only at the origin (of the qp -plane). A pair-wise comparison of energy densities of stationary states with same chemical potential captures the possible phase-coexistence inside a harmonic trap for negative values of the quadratic Zeeman term, q (see Fig.3.1(b)). This also includes an estimation of the radius of phase boundaries under harmonic confinement. The same comparison is sufficient to

deduce that no phase separation or domain formation is possible for $q > 0$. Note that, in principle, the ferromagnetic and the polar states can coexist in the region I and VI, (in Fig.3.1(a)) still there is no phase separation in this region (Fig.3.1(b)). This will be clear when we will discuss the reason for not getting phase separation for $q > 0$.

As an example, let us choose a region (III) where the first three single-component phases can exist. We can assume the trapping potential to be a 2D harmonic confinement, $U(\mathbf{r}) = \frac{1}{2}\kappa r^2$, where κ is related to the trapping frequency ω as, $\kappa = M\omega^2$. A comparison of energy densities of the $(1, 0, 0)$ and $(0, 1, 0)$ states,

$$\Delta e_{12} \equiv e_1 - e_2 = \frac{(p - q)(2U(r) - (p - q))}{2c_0}, \quad (3.57)$$

implies that the state $(1, 0, 0)$ energetically is favored below a radius $r_0^2 = (p - q)/\kappa$ because $(p - q) > 0$. The state $(0, 1, 0)$ should be existing for $r > r_0$ and is the peripheral state when $(1, 0, 0)$ sits at the core of the harmonic trap. This type of domain formation cannot happen when $(p - q)$ is negative as $r_0^2 > 0$, which implies that the phase separation between the F1 and P is only possible in region-I, II, III and IV of Fig.3.1(a), where $(p - q) > 0$.

Under the T-F approximation, these pair-wise comparisons of energy density reveals the ground state domains of stationary states for $c_1 = 0$. Note that, in the regions marked as III and IV in Fig.3.1(a), all three types of phase separation are allowed. No cases can be found for simultaneous domain formation including all three states. As we are doing a pair-wise comparison, in situations where there are more than one possibility of phase separations, one can start the analysis by first considering which of the states is energetically favored at the center of the trap. This is a logical first step as the condensation in an experimental situation arises first at the central region because of the density being maximum there [120]. For example, in region-III one can start with the F1 state that is energetically minimum at $U(r) = 0$, the center of the trap. Out of the two domain-forming possibilities with either the polar or F2 states, the polar state wins because the separation can happen at a smaller radius than that with the F2 state. Now, when the polar or $(0,1,0)$ state is in the outer region, one can check that the $(0,0,1)$ never wins energetically over $(0,1,0)$.

The T-F approximated energy densities of the three unrestricted stationary states (F1,

P, and F2) are compared simultaneously (not a pair-wise comparison) to get the phase diagrams (Fig.3.2) on an $U(r)$ vs p and $U(r)$ vs q planes under the constraint of a constant chemical potential.

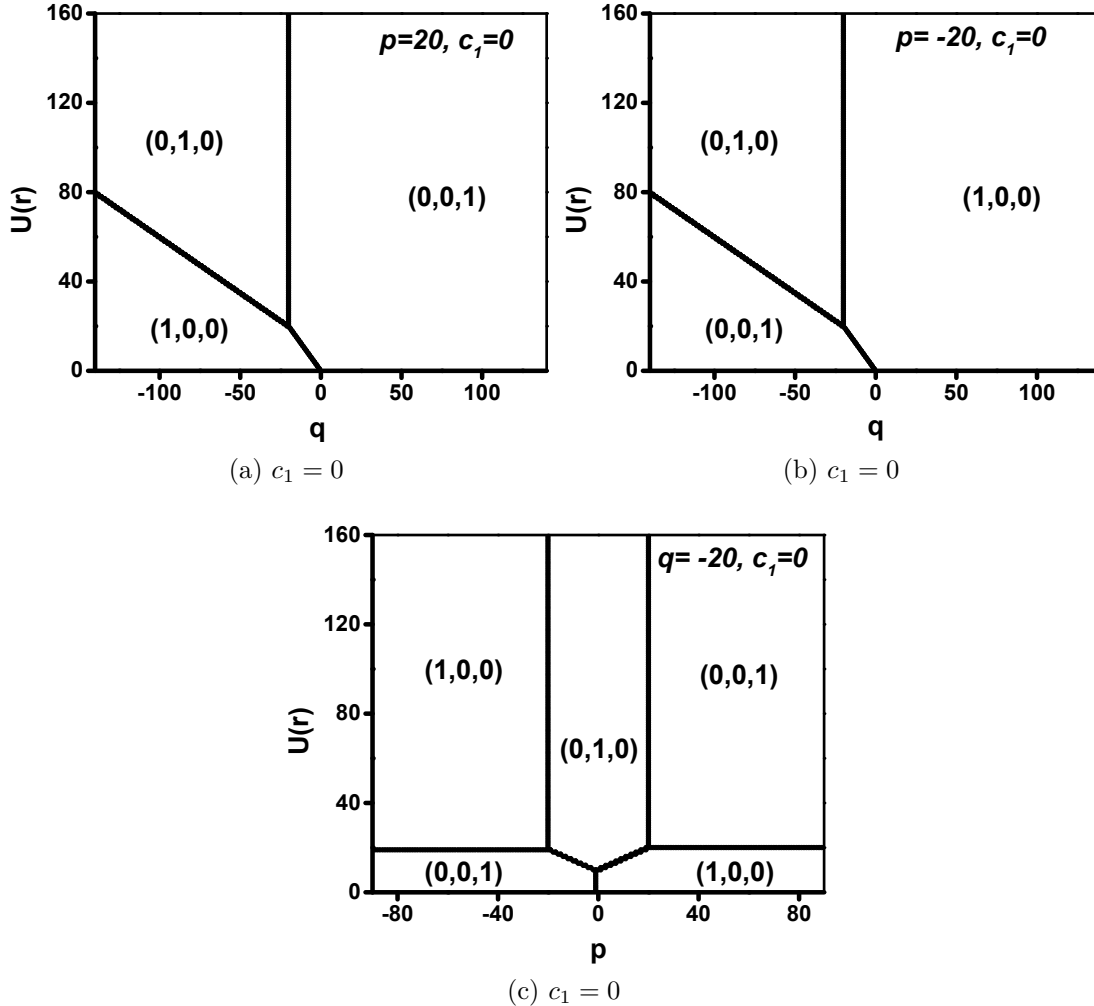


Figure 3.2: Phase-coexistence of a spin-1 BEC without spin interaction ($c_1 = 0$). (a) and (b) showing phase separation for opposite linear Zeeman terms. These sub-figures are symmetric under the change in the direction of the magnetic field, which determines the sign of p . Depending on the sign of p , the ferromagnetic states swap their positions, which is natural as the direction of the magnetic field favors one out of the two possible ferromagnetic states. (c) The quadratic Zeeman term is fixed at a negative value. The phase boundaries remain unaffected by the change of chemical potential (μ). In this and all the following figures, p , q , and $U(r)$ are shown in Hz , obtained by dividing the energy by Planck's constant, h .

If the quadratic Zeeman term q is sufficiently negative with $|q| > |p|$, phase separation between ferromagnetic and polar phases is observed, where near the center of the trap $(1,0,0)$ state is energetically favored when the linear Zeeman term is positive (Fig.3.2(a)). Similarly, when p is negative and the above-mentioned condition is met, domain structure

with the other ferromagnetic state $(0,0,1)$ occupying the central region along with the polar state in the peripheral region is observed (see Fig.2.1(b)). For small negative values of q , such that $|q| < |p|$, domain formations between the ferromagnetic states are observed. For this situation, if p is positive F1 or the $(1,0,0)$ state is energetically lowest at the trap center (Fig.3.2(a)) which corresponds to region-II in Fig.3.1(a). Whereas, F2 or the $(0,0,1)$ state is favored at the central region when p is negative (see Fig.2.1(b)) which corresponds to region-V of Fig.3.1(a).

All possible domain structures involving the stationary states can be observed for negative values of q , which is shown in Fig.3.2(c) while the pair-wise energy density comparison tells that no possible phase separation can happen for $q > 0$. The ground state will be selected depending on the chemical potential μ . As we are only focussing on the phase separation scenario, we are keeping a constant μ for the three unrestricted stationary states. We find $(0,0,1)$ to be energetically lowest for $p > 0$ and $q > 0$ (in the region-I, VIII) which can also be seen in Fig.3.2(a)). This situation will change when the constant μ condition is relaxed in order to find the only existing phase without any phase separation. One can look for the ground state in these regions given that the particle numbers present in the condensate are fixed. This reveals that the F1 state or $(1,0,0)$ state becomes the ground state in region-I, VI and the polar state becomes the ground state in region-VII, VIII, which is shown in the shaded region of Fig.3.1(b). The present analysis captures all the possibilities of phase separation under the T-F approximation.

If we compare the results obtained in this confined case with the phase diagram of the uniform BEC, we can notice that Fig.2.1(b) indicates there can be no phase-coexistence of the two opposite ferromagnetic phases (at nonzero p). In contrast, the confined picture reveals the opposite. Thus, one should probe the phase separation scenario under actual confinement following the method shown in this section, rather than extrapolate the results based on the density of the homogeneous case to that under confinement.

3.2.2 Anti-ferromagnetic type of spin interaction

In the previous section, we discussed how the T-F approximated energy density comparison of all possible stationary states reveals domain-forming possibilities when the spin interaction is absent. Here, we will compare the stationary states for the anti-

ferromagnetic type of spin interaction, i.e., $c_1 > 0$. In section 3.1, we have looked into all possible stationary states under confinement using the T-F approximation and also found out the number density and energy density for each stationary state. As we are going to compare the energy densities, the results of section 3.1 are summarized in Table 3.2 for convenience. Note that, the energetic comparison can be done for a range of p

States	Variation of density	Energy density	Restriction
(1,0,0) <i>F1</i>	$(c_0 + c_1)n(\mathbf{r}) = \mu + p - q - U(\mathbf{r})$	$\frac{[U(\mathbf{r})-p+q][\mu+p-q-U(\mathbf{r})]}{(c_0+c_1)} + \frac{[\mu+p-q-U(\mathbf{r})]^2}{2(c_0+c_1)}$	<i>none</i>
(0,1,0) <i>P</i>	$c_0n(\mathbf{r}) = \mu - U(\mathbf{r})$	$\frac{U(\mathbf{r})[\mu-U(\mathbf{r})]}{c_0} + \frac{[\mu-U(\mathbf{r})]^2}{2c_0}$	<i>none</i>
(0,0,1) <i>F2</i>	$(c_0 + c_1)n(\mathbf{r}) = \mu - p - q - U(\mathbf{r})$	$\frac{[U(\mathbf{r})+p+q][\mu-p-q-U(\mathbf{r})]}{(c_0+c_1)} + \frac{[\mu-p-q-U(\mathbf{r})]^2}{2(c_0+c_1)}$	<i>none</i>
(1,1,0) <i>MF1</i>	$(c_0+c_1)n(\mathbf{r}) = \mu - U(\mathbf{r}) + (p - q)$	$\frac{U(\mathbf{r})[\mu+p-q-U(\mathbf{r})]}{(c_0+c_1)} + \frac{c_0[\mu+p-q-U(\mathbf{r})]^2}{2(c_0+c_1)^2} + \frac{c_1}{2}n_1^2$	$n_0 = \frac{p-q}{c_1}$
(1,0,1) <i>AF</i>	$c_0n(\mathbf{r}) = \mu - q - U(\mathbf{r})$ and $(n_1 - n_{-1}) \equiv F_z = \frac{p}{c_1}$	$\frac{[U(\mathbf{r})+q][\mu-q-U(\mathbf{r})]}{c_0} + \frac{[\mu-q-U(\mathbf{r})]^2}{2c_0} - \frac{p^2}{2c_1}$	<i>none</i>
(0,1,1) <i>MF2</i>	$(c_0+c_1)n(\mathbf{r}) = \mu - U(\mathbf{r}) - (p + q)$	$\frac{U(\mathbf{r})[\mu-p-q-U(\mathbf{r})]}{(c_0+c_1)} + \frac{c_0[\mu-p-q-U(\mathbf{r})]^2}{2(c_0+c_1)^2} + \frac{c_1}{2}n_{-1}^2$	$n_0 = \frac{-p-q}{c_1}$
(1,1,1) <i>(A)PM</i>	$(c_0 + c_1)n(\mathbf{r}) = k_1 - U(\mathbf{r})$ where, $k_1 = \mu + \frac{(p^2-q^2)}{2q}$	$\frac{U(\mathbf{r})[k_1-U(\mathbf{r})]}{c_0+c_1} + \frac{c_1}{2} \left[\frac{k_1-U(\mathbf{r})}{c_0+c_1} - \frac{p^2-q^2}{2qc_1} \right]^2 + \frac{c_0}{2} \left[\frac{k_1-U(\mathbf{r})}{c_0+c_1} \right]^2$	<i>PM</i> ($ p < q $) <i>APM</i> ($ p > q $)

Table 3.2: T-F approximated number density and energy density expressions for different stationary states at for a generic trapping potential, are shown here. As the n_0 component is strictly positive, the mixed-ferromagnetic states, *MF1*, and *MF2* are restricted in a (q, p) parameter space (depending on the sign of c_1). The *APM* and the *PM* state are identical in their number density and energy density expressions. The *APM* state is only valid when $|p| > |q|$ whereas, the *PM* state exists when $|q| > |p|$ is satisfied. [121, 122]

and q values along with the trapping potential $U(\mathbf{r})$ keeping in mind that, for the mixed states, the sub-component densities must be positive. This puts restrictions over p and q for all the mixed states. For example, the T-F approximated number density of the anti-ferromagnetic state (Eq.3.19a-3.19b),

$$n_{\pm 1}(\mathbf{r}) = \frac{\mu - q - U(\mathbf{r})}{2c_0} \pm \frac{p}{2c_1}, \quad (3.58)$$

restricts the AF state inside the allowed values of p and q so that, both the sub-component densities are positive, i.e.,

$$\frac{c_1}{c_0} (\mu - q - U(\mathbf{r})) > p > -\frac{c_1}{c_0} (\mu - q - U(\mathbf{r})). \quad (3.59)$$

This condition is similar to the restriction over p , which is $-c_1 n < p < c_1 n$, for the untrapped (homogeneous number density) case [83] which we have briefly discussed in section 2.4.

We will take the realistic example of ^{23}Na , for which the spin interaction is of anti-ferromagnetic type. The numerical value of c_1 is $2.415 \times 10^{-19} \text{ Hz } m^3$, where the energy is in units of Hz , which is obtained by dividing the S.I value by h , i.e, Planck's constant. The parameter c_0 is $149.89 \times 10^{-19} \text{ Hz } m^3$ for this element [83, 119, 123]. Now, the energy density of all possible states can be compared to look for phase-separated structures at a constant chemical potential (μ) ensuring chemical stability. We fix the μ roughly at 400 nK, which is roughly 7084 Hz . We vary the parameter p and q within a range of -150Hz to 150Hz . External potential $U(r)$ is varied from 0 to 170Hz . As we are relying on the T-F approximation, we have restricted the search for domain structure to a region near the center of the trap, where the density is higher and the T-F approximation, in general, is valid. Note that, one can expect a significant deviation from the T-F approximated number density profile near the T-F radius, where according to the T-F approximation, the density sharply goes to zero. For example, the T-F radius is at around $U(r)$ of the order of 6000 Hz for the ferromagnetic states with the specified range of p and q .

For the purpose of better representation, we fix either p or q and tune the other with $U(r)$. For a fixed value of $q = -40 \text{ Hz}$, domain structures between the ferromagnetic states are obtained. If the linear Zeeman term is negative, a bilayer domain with the F2

state at the core and F1 state in the outer region is observed (Fig.3.3(a)). The situation is just the opposite for positive values of p , where the F1 state energetically favored near the high-density central region and the F2 state staying in the low-density region form a phase-separating structure in Fig.3.3(b).

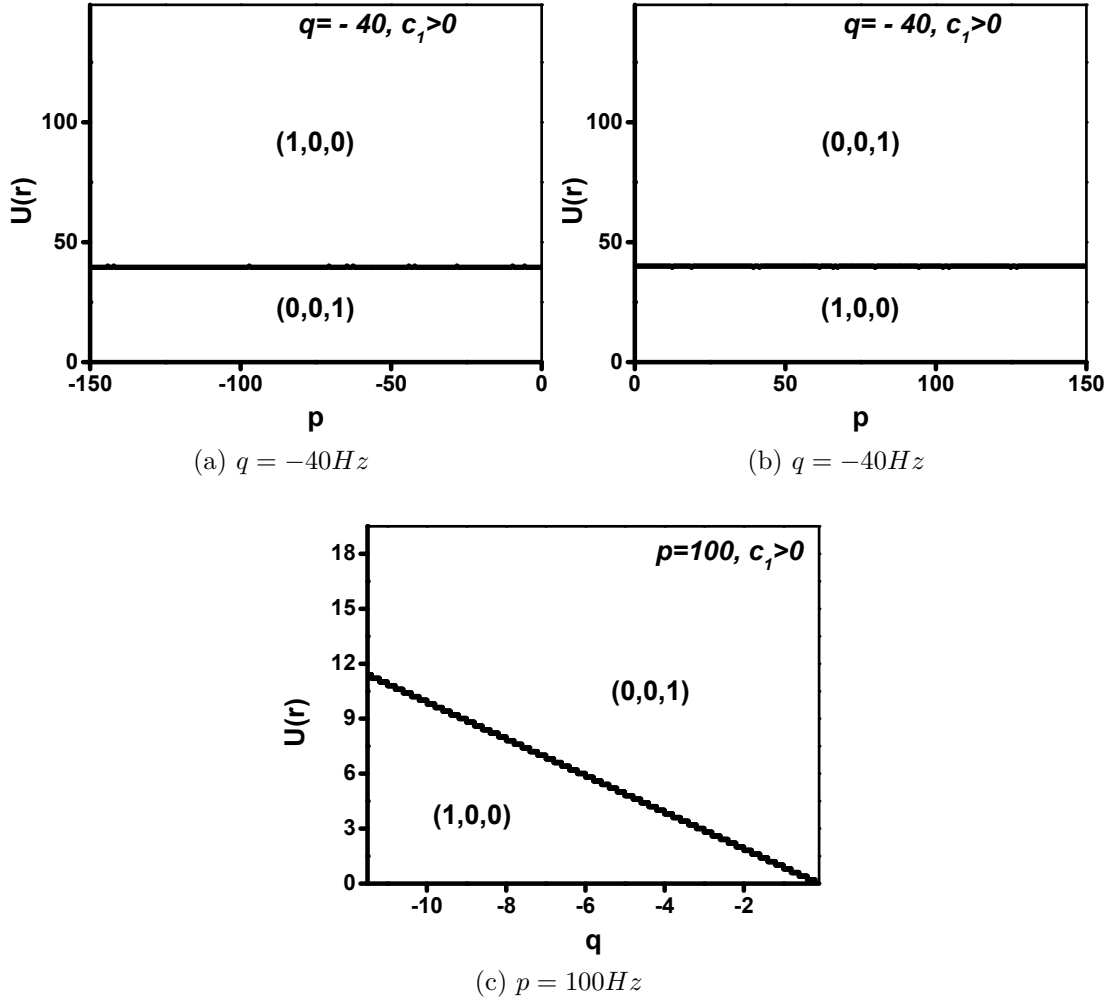


Figure 3.3: Domain formation possibilities for the anti-ferromagnetic type of spin-spin interaction ($c_1 > 0$) involving two coexisting stationary states. Phase separation between the two ferromagnetic states when the quadratic term is fixed at $q = -40 Hz$, (a) with the F2 state occupying the central region for negative values of p , and (b) the F1 state energetically favored in the high-density region with positive p . In both cases, the domain boundary is unaffected by the change in the magnitude of p . (c) For fixed value of p , the same domain boundary gets affected by the change in the magnitude of q as, $U(r) = -q$.

Fig.3.3(a) and Fig.3.3(b) show that for a fixed negative value of the quadratic Zeeman term q , the domain boundary is insensitive to the change of p . Whereas, if the linear term is fixed at $p = 100 Hz$, for negative q values, one can see in Fig.3.3(c), that the F1 state which occupies the central region pushes the domain boundary outward as q is further

decreased.

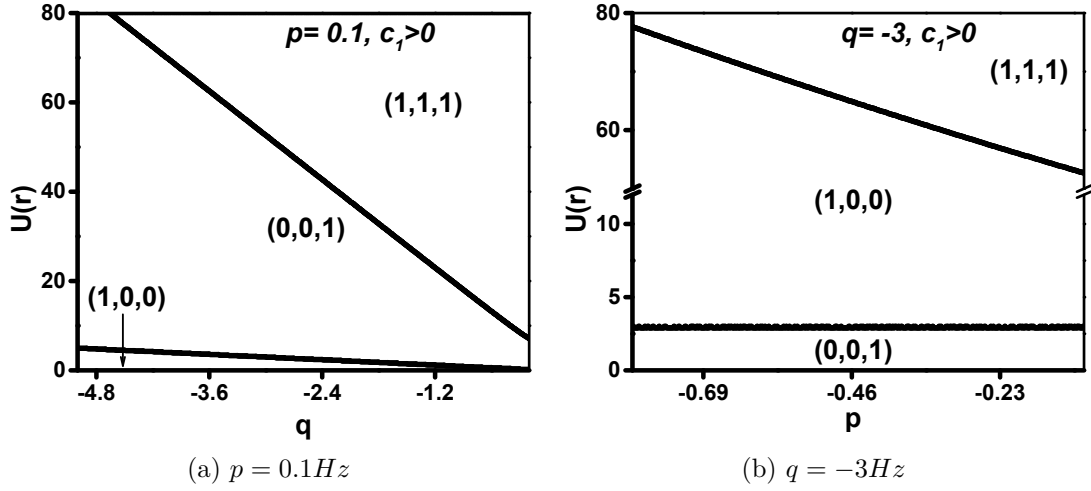


Figure 3.4: Domain formation possibilities for the anti-ferromagnetic type of spin-spin interaction ($c_1 > 0$) involving three coexisting stationary states. (a) For small values of positive p and negative q , the F1 state occupies the center, with the F2 state in the middle followed by the PM state in the outer region of the trap. (b) With the change in sign of p , a similar tri-layer domain structure with the interchange of the position of the ferromagnetic states is observed.

Another interesting possibility is to have a tri-layer domain formation where three stationary states coexist side by side. Such a situation is obtained for very small values of linear and quadratic terms. In Fig.3.4(a), the linear term is fixed at a small positive value, where we get a tri-layer domain between the F1 state at the central region followed by the F2 state in the middle and the PM state (as, $|q| > |p|$) at the low-density region of the trap. For fixed negative values of q and varying negative p a similar structure is obtained with the F2 state now occupying the central region and F1 in the middle, while the PM state occupying the low-density region (see Fig.3.4(b)).

Note that, all domain structures are obtained for negative values of q . Although spin-spin interaction is positive (i.e., $c_1 > 0$), the anti-ferromagnetic state does not win energetically to show phase-coexistence. Moreover, the mixed-ferromagnetic states and the APM state also do not partake in any domain structures. There is no underlying reason for not getting domain structures, where these stationary states are involved, and there is a possibility of getting such domain structures if we go beyond the specified range of $U(r)$ or even p, q values. This fact indicates to some limitations of the T-F approximation.

The phase-coexisting structures discussed till now, are for a generic trapping potential

$U(r)$ under the T-F approximation. Now, to get to the radial variation of (sub-component) densities of the domain forming stationary states, one can use the analytical expressions of number densities summarized in Table 3.2. We assume a 3D harmonic confinement with the trapping frequency, $\omega = 2\pi \times 100 \text{ Hz}$.

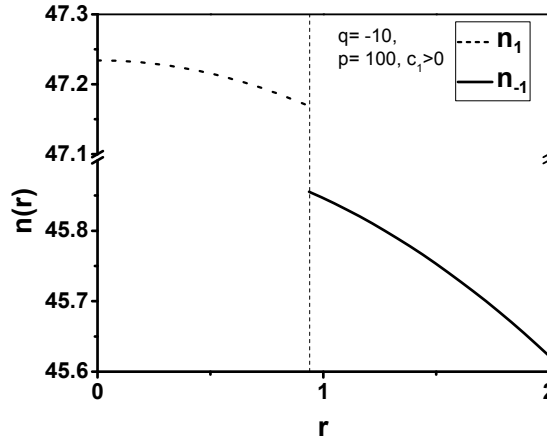


Figure 3.5: The radial density plot corresponding to the domain formation possibility shown in Fig. 3.3(c), inside an isotropic 3D harmonic confinement.

We can fix the linear and quadratic terms at $p = 100 \text{ Hz}$ and $q = -10 \text{ Hz}$ that corresponds to the domain structure shown in Fig.3.3(c). The F1 state occupies the central region of the trap which corresponds to the n_1 component that decreases with radial distance from the trap center as $-r^2$. This is followed by the F2 state (n_{-1} component) that appears roughly at a distance of $0.94 \mu\text{m}$ from the center of the trap (Fig.3.5). Note that, the difference in the T-F approximated density of the ferromagnetic states near the domain boundary is not very large, which increases the chance for mechanical stability.

3.2.3 Ferromagnetic type of spin interaction

In this section, we search for domain-forming possibilities when $c_1 < 0$, i.e., for the ferromagnetic type of spin interaction. We take the parameter values corresponding to spin-1 ^{87}Rb BEC, for which c_1 comes out to be $-0.275 \times 10^{-19} \text{ Hz m}^3$. The spin-independent interaction coefficient c_0 is $78.02 \times 10^{-19} \text{ Hz m}^3$ for this element [83, 124]. To probe for domain structure we vary the controllable parameters p , q , and the trapping potential $U(r)$ within the same range specified in the previous section. The chemical potential μ is also fixed at the same value of 7084 Hz .

When q is fixed at a small negative value, the anti-ferromagnetic state (1,0,1), dominates

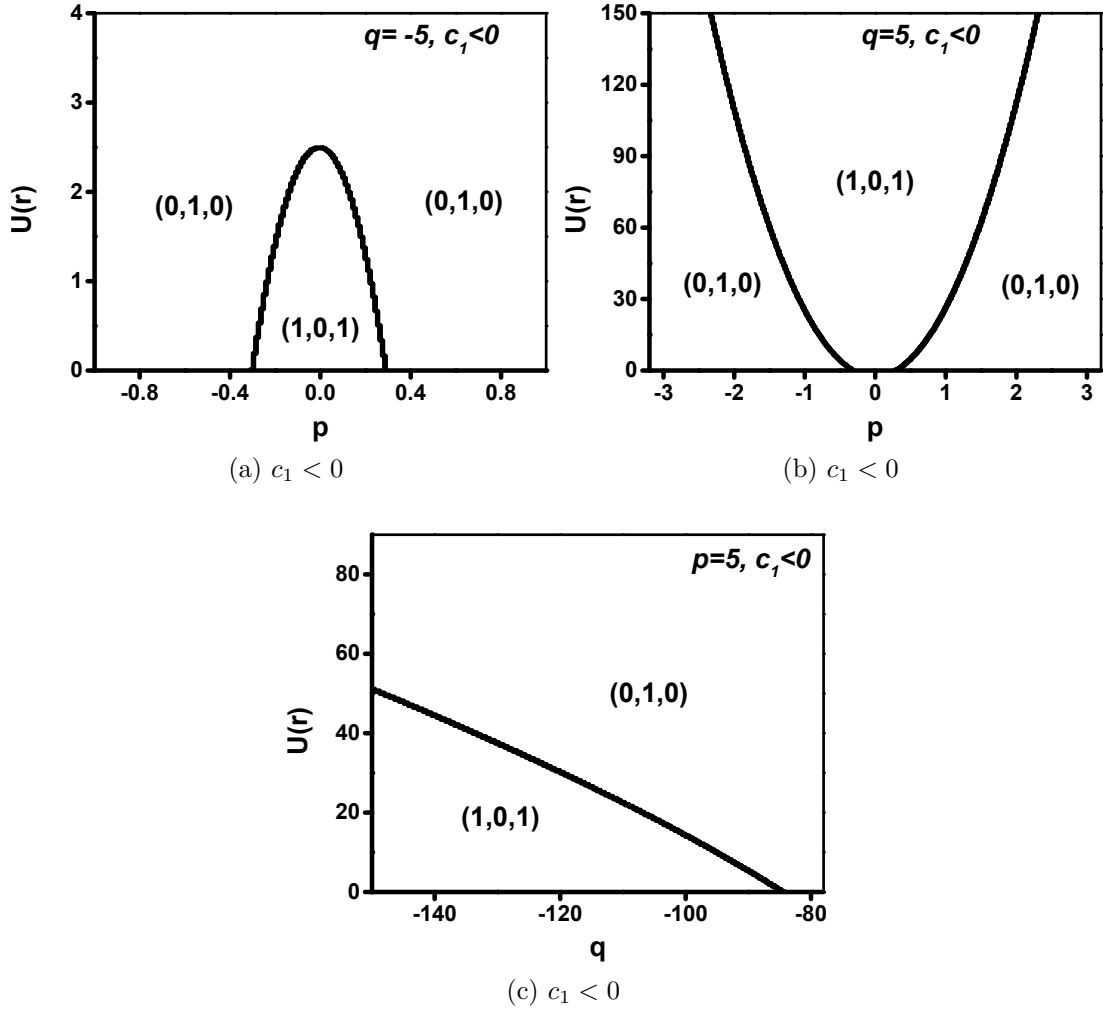


Figure 3.6: Phase-coexistence possibilities for ferromagnetic type spin interaction. Fixing the quadratic term, q at the specified values, and for small p , possible phase separations between the anti-ferromagnetic and polar states are observed with the sign of q being (a) negative favors the AF state, and (b) positive favors the polar state in the high-density region. (c) Similar domain structure is also present for small positive p and large negative values of q .

near the center of the trap, for very small values of p , while the polar state $(0,1,0)$ forms a domain structure staying in the low-density region (see Fig.3.6(a)). With the increment of the magnitude of p , the domain boundary moves towards the trap center and for sufficiently large p , this domain structure is lost. A contrasting situation is obtained if q is fixed at a small but positive value. For small values of p , except near $p = 0$, the polar state energetically winning near the center of the trap coexist with the AF state. An increment in the magnitude of p only broadens the central domain occupied by the polar state (in Fig.3.6(b)). The AF-polar domain structure is also observed for large values of q , when p is fixed at a small positive value (see Fig.3.6(c)).

One of the common features of the domain structures in Fig.3.6(a) and Fig.3.6(b) is that a slight increase of $|p|$ would prefer the polar phase to expand its domain in both cases. Also, after a limiting value of $|p|$ the structure is lost. Interesting to note that, as p appears in the energy expression of the AF state (for details see Table 3.2), an increase in p^2 would increase its energy density (as $c_1 < 0$). Whereas, the energy density of the polar state does not depend on p . As a result, depletion of the domain of the AF state with the increment in the magnitude of p is quite reasonable to occur. The energy density of the polar state does not depend on q but the AF state gets affected approximately as $qn(r)$, where $n(r)$ is the total density. Therefore, for negative q in Fig.3.6(a) the AF state is energetically favored in the high-density region. Whereas, in Fig.3.6(b), for positive q , the AF state gets pushed away to the low-density region.

We found that there is no dominance of the ferromagnetic phases in the domain formation scenario. Also, the mixed-ferromagnetic states as well as PM and APM states do not participate in any phase-coexisting scenario. We have restricted the search to a very small region of the parameter space for the reason specified earlier. Tuning p and q beyond $\pm 150 Hz$, the ferromagnetic state dominates in the domain formation scenario. Also, the other states may appear for $U(r)$ beyond $170 Hz$ which we have not included in Fig.3.6.

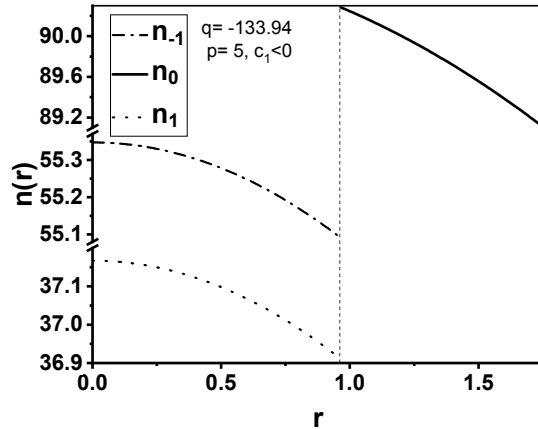


Figure 3.7: In an isotropic 3D harmonic confinement, the number density variation with the radial distance from the center of the trap is shown corresponding to the domain formation possibility in Fig.3.6(c). The $n_1(r)$ and $n_{-1}(r)$ component of the AF state which occupies the central region decreases with the distance r , while after a distance, which specifies the domain boundary, the polar state ($n_0(r)$ shown in solid line) appears.

We have reasoned earlier about the importance of the sub-component density plot.

We take the example of Fig.3.6(c), where we fix the linear and quadratic Zeeman term at 5 Hz and -133.94 Hz respectively. Under the same 3D harmonic confinement with trapping frequency $\omega = 2\pi \times 100 \text{ Hz}$ we plot the radial variation of sub-component number densities in Fig.3.7. The *AF* state staying at the central region of the trap vanishes at an approximate distance of $0.95 \mu\text{m}$. One can check from Table 3.2 that for the *AF* state, the $n_{-1}(r)$ component is greater than the $n_1(r)$ even for $p > 0$ as $c_1 < 0$. The polar phase with only one sub-component $n_0(r)$ occupies the outer region at approximately $r \gtrsim 0.95 \mu\text{m}$. The total number density of the *AF* and the polar state at the interface, in this case also, is not very large, which is important for mechanical stability.

3.3 Discussion

In this chapter, we have considered a trapped spin-1 BEC, and from the GP equation, we find out the allowed stationary state structures. Under the Thomas-Fermi approximation, we got to necessary details of the stationary states in terms of the sub-component and energy density, which in turn, produces the total energy as well. A comparison of the energy densities for different stationary states can be done on an equal footing, which gives an idea about the stationary state that is favored locally inside the confinement. This allows for the study of possible domain-forming structures, under a single essential constraint of the same chemical potential (μ) for the chemical stability of the neighboring domains. This procedure is quite general and is applicable to any trapping geometry. The method presented in this chapter can capture all possible domain-forming scenarios in a unified way, whereas the phase separation studies are previously done mostly on a case-by-case basis.

We started with the simple possible case, that is in the absence of the spin-interaction ($c_1 = 0$), which is the Manakov limit in the soliton studies [71]. Not only this case has theoretical importance, but also it is experimentally possible to tune the spin interaction parameter close to zero by applying optical and magnetic Feshbach resonance [115, 125–127]. In this situation, we demonstrate that a pair-wise comparison of energy density is enough to predict the phase separation scenario, as the multi-component states, in this case, are severely restricted in (q, p) parameter space, reducing significant effort.

We have also presented a detailed study of the phase-coexistence of stationary states for

both the ferromagnetic and the anti-ferromagnetic type of spin interaction. The procedure presented in this section is indeed very general and captures all possible multi-component states equally, irrespective of the confining potential, as long as the T-F approximation is valid. Although, for demonstration purposes, we have made use of 3D isotropic harmonic confinement, the same analysis can be used to include any potential and can be extended to effectively 2-dimensional or 1-dimensional systems. GP dynamics for effective 2- and 1-dimensional systems are obtained by integrating out the dimensions which are confined below the healing length [115] that yields the same structure of GP model with the renormalized couplings, i.e., the length scales of the confined dimensions would feature in the interaction parameters c_0 and c_1 .

Note that, while the T-F approximation is excellent near the center of the trap, one can expect a significant deviation from the T-F approximated results near the low-density region of the trap, i.e., near the T-F radius (where the T-F approximated density sharply goes to zero, which is also not physical at all). As the linear and quadratic Zeeman terms also affect the T-F radius, we have restricted our search for domain structures to a narrow range of p, q values. Also, we have only considered the trapping potential from 0 to 170 Hz , which is in very narrow proximity to the center of the trap. Note that, near the T-F radius of the ferromagnetic states the $U(r)$ is of the order of 6000 Hz . We have found a remarkable result that when interactions are ferromagnetic, the anti-ferromagnetic and polar phases dominate the domain formation scenario and for the anti-ferromagnetic type of spin interaction the situation is just the opposite. It should be noted that the Zeeman terms may be varied to even higher values [128] and the scheme shown here using energy density comparison should suffice to reveal any domain structure even in that regime as long as one can rely on the T-F approximation.

The domain boundaries obtained from the T-F approximation serve as the first step for the study of dynamics under various conditions. Near the phase boundaries, the derivative of the order parameter becomes significant and cannot be neglected, however, under the T-F approximation that is not the case. So, it is essential that the stability analysis around each and every phase boundary of phase domains be done which would provide a deeper understanding of the domain formation scenario. The constant chemical potential constraint which is essential for the chemical stability of coexisting phases may also be a heavy requirement for many cases under various conditions. The failure of maintaining

this constraint may also rule out some otherwise allowed structures. However, that can only be understood once we look into the requirement of fulfilling this constraint explicitly. But, the analysis and the predictions presented in this chapter would serve as a starting point for all these prospects essentially in a broader sense.

Chapter 4

Variational method: Ground state properties in the absence of the magnetic field

In the previous chapter, we derived the number density and energy density expressions corresponding to each stationary state of a trapped spin-1 BEC under the T-F approximation. These T-F approximated energy densities were compared locally, under an essential constraint of the same chemical potential that revealed all possible domain structures.

Note that, the T-F approximation is widely used to study trapped condensates for its analytical ease, but it is only valid as long as the density is large enough to neglect the kinetic energy contribution. There exist many situations, where even if this condition is met, the application of the T-F approximation could give rise to other issues. For large condensates, where the density is high enough, situations may arise when the competing stationary states have comparable total energy under the T-F approximation. In such cases, the kinetic energy may become a distinguishing factor, and should not be neglected.

In this chapter, we present a case study related to the ground state of a harmonically trapped spin-1 BEC under the influence of spin interaction when the external magnetic fields are negligible. We will start with the T-F approximated results, which would reveal that the total energy of the competing stationary states which are ground state candidates are so close that one cannot ignore the kinetic energy contribution. To give an alternative

and better method that takes account of the kinetic energy of the system, which is neglected in the T-F approximation, we introduce a multi-modal variational method. This variational method works exceptionally well to provide a detailed and rigorous insight into the problem at hand, which is beyond the scope of the T-F approximation. This method is general enough to be applied to other situations where the T-F approximated results are inconclusive. Additionally, this multi-modal variational method produces accurate results even for small condensates with particle numbers as low as 500, where the density is not high enough to trust the T-F approximated results.

The spinor BEC attracted a lot of attention due to its complexity and rich ground state structures [49, 83, 95, 114, 129]. Many theoretical and computational studies have been done to understand the role of spin-spin interactions on the ground state structure. This often requires a negligible presence (or absence) of the external field. As a result, there have been a lot of analyses on the ground state when the quadratic and linear Zeeman terms are practically zero [115, 116].

In [54], the ground state structure in a harmonic confinement was studied by T.-L. Ho, where it was shown that the ferromagnetic state becomes the ground state when the spin interaction is of the ferromagnetic type, and for the anti-ferromagnetic interaction the polar state is energetically favored to become the ground state. It was also argued that, due to spin rotational symmetry, there exist degenerate states that are equally likely to be the ground state. It is obvious that the anti-phase-matched (APM) state, the polar state, and the anti-ferromagnetic (AF) state are the stationary states that fall into this degenerate class. In another notable theoretical work [130], the single-mode approximation (SMA) was employed for the three-component states. Note that, in SMA, it is assumed that all the sub-components share the same spatial profile. The ground state structure is investigated with these three-component states to check the validity of SMA. Due to the fixing of magnetization ($M \neq 1$), the phase-matched (PM) state becomes the ground state that follows SMA (for the ferromagnetic type of interaction). In contrast, the APM state, which does not follow SMA, becomes the ground state when spin-interaction is of anti-ferromagnetic type. One can also start with non-equilibrium populations in different spin components and with time evolution get to the ground state with the equilibrium densities [131]. The ground state structure with fixed magnetization [115, 129], or in zero magnetic force [116] have also been explored. One can also get to the

phase diagram of ground states by tracking modulational instability for anti-ferromagnetic condensate [100]. The ground state phase diagram gets substantially modified if the finite temperature effects [132–134] and interparticle correlations [135] are included.

The variational approach that we develop and present in this chapter was partly developed in [136] by Pendse and Bhattacharyay for non-spinor BEC. This multi-modal approach takes into account the individual Zeeman components. Not only this method provides a smooth density profile of the Zeeman components but also ensures a smooth energy-density profile where, unlike the T-F approximation, the kinetic energy is not neglected.

4.1 T-F approximated total energy in the absence of the magnetic field

Before we go into the details of the variational method, we will discuss the T-F approximated results briefly. It should be noted that at zero magnetic fields, the system becomes degenerate even at non-zero temperature [128]. In the absence of the magnetic field, the linear and quadratic Zeeman term is obviously not present, i.e., $p = 0$ and $q = 0$ and it is interesting to look at the effect of the spin-dependent interaction [54, 115, 131]. Note that, the T-F approximated energy density corresponding to the (A)PM state shown in Table 3.2 is ill-defined at $q = 0$. To get rid of this issue, one can rewrite the GP equation with $p, q = 0$ in the first place and solve the phase equations to get the details of the PM state. In Chapter 3, we have already discussed the $k(\mathbf{r}) \equiv \sqrt{n_1(\mathbf{r})/n_{-1}(\mathbf{r})} = 1$ case for the APM phase, which corresponds to the situation $p = 0$ and $q = 0$. We can use the energy density of the APM state (shown in Eq.3.54) as obtained under the T-F approximation in this limit.

For the purpose of completeness, we will have a very brief discussion about the stationary states at $p = 0$ and $q = 0$ as obtained from the T-F approximation. To get to the ground state, we will consider a fixed number of condensate particles, for which the chemical potential would be different for different stationary states. In the subsequent analysis, we will explicitly assume the three-dimensional isotropic harmonic confinement, and compare the total energy of the different stationary states which reveals the ground

state under the T-F approximation. We will also consider a one-dimensional harmonic trapping geometry and quantitatively discuss the T-F approximated results in that case. Note that, the numerical solution of the GP equation is easier to obtain in one-dimensional case.

4.1.1 Stationary states at $p=0$ and $q=0$

Putting $p = 0$ and $q = 0$ in the GP equation leads to the phase equations,

$$\hbar\dot{\theta}_0 = \frac{1}{\sqrt{n_0(\mathbf{r})}} \left(-\frac{\hbar^2 \nabla^2}{2M} + U(\mathbf{r}) + c_0 n - \mu \right) \sqrt{n_0(\mathbf{r})} + c_1 (n_1 + n_{-1} + 2\sqrt{n_{-1}n_1} \cos \theta_r), \quad (4.1)$$

$$\begin{aligned} \hbar\dot{\theta}_{\pm 1} = \frac{1}{\sqrt{n_{\pm 1}(\mathbf{r})}} \left(-\frac{\hbar^2 \nabla^2}{2M} + U(\mathbf{r}) + c_0 n - \mu \right) \sqrt{n_{\pm 1}(\mathbf{r})} \pm c_1 (n_1 - n_{-1}) \\ + c_1 n_0 \left(1 + \sqrt{\frac{n_{\mp 1}(\mathbf{r})}{n_{\pm 1}(\mathbf{r})}} \cos \theta_r \right). \end{aligned} \quad (4.2)$$

Under stationarity conditions, and in the T-F approximation, the solution corresponding to the single-component states i.e., the ferromagnetic states and the polar state can be easily obtained, which is similar to that shown in Table 3.2 with $p = 0$ and $q = 0$. The same goes for the anti-ferromagnetic state. These results are summarized in Table 4.1. Note that, mixed-ferromagnetic states (MF1 and MF2) are not allowed in this limit as the n_0 component becomes zero (see Table 3.2). We will focus on the other multi-component states in this limit, of which only the (A)PM state requires attention in this limit, as the energy density shown in Table 3.2 corresponding to these states is ill-defined when $p = 0$ and $q = 0$.

Phase-matched state (PM)

The stationary state corresponding to the relative phase $\theta_r = 0$ with all three sub-components populated is known as the phase-matched (PM) state. Under T-F approximation, Eq.4.1-4.2 can be simplified for this stationary state,

$$U(\mathbf{r}) + c_0 n - \mu + c_1 (n_1 + n_{-1} + 2\sqrt{n_{-1}n_1}) = 0, \quad (4.3)$$

$$U(\mathbf{r}) + c_0 n - \mu + c_1(n_1 - n_{-1}) + c_1 n_0 \left(1 + \sqrt{\frac{n_{-1}(\mathbf{r})}{n_1(\mathbf{r})}}\right) = 0, \quad (4.4)$$

$$U(\mathbf{r}) + c_0 n - \mu - c_1(n_1 - n_{-1}) + c_1 n_0 \left(1 + \sqrt{\frac{n_1(\mathbf{r})}{n_{-1}(\mathbf{r})}}\right) = 0, \quad (4.5)$$

where $\cos \theta_r = 1$ as $\theta_r = 0$. Now the addition of the last two equations leads to,

$$U(\mathbf{r}) + c_0 n(\mathbf{r}) - \mu + \frac{c_1 n_0}{2\sqrt{n_1 n_{-1}}} (n_1 + n_{-1} + 2\sqrt{n_1 n_{-1}}) = 0. \quad (4.6)$$

If we compare this with the phase equation corresponding to $\dot{\theta}_0 = 0$, i.e., Eq.4.3, we get a relation between the n_0 and the other two sub-components,

$$n_0 = 2\sqrt{n_1 n_{-1}}, \quad (4.7)$$

which is valid as long as all the sub-components are populated, which as we have discussed earlier, is a necessary condition for the (A)PM state. One can also subtract the Eq.4.5 from the Eq.4.4, which does not give any new condition but rather confirms the same relation.

One can use the relation Eq.4.7 in Eq.4.3, that leads to

$$U(\mathbf{r}) + c_0 n - \mu + c_1(n_1 + n_{-1} + n_0) = 0, \quad (4.8)$$

which can be rearranged to get to the total number density,

$$n(\mathbf{r}) = \frac{\mu - U(\mathbf{r})}{c_0 + c_1}, \quad (4.9)$$

where the total number density is obviously the sum of all the sub-component densities, i.e., $n(\mathbf{r}) = n_1(\mathbf{r}) + n_0(\mathbf{r}) + n_{-1}(\mathbf{r})$. Now depending on the magnetization density $\tilde{m} \equiv n_1(\mathbf{r}) - n_{-1}(\mathbf{r})$, one can write the sub-component densities as

$$n_1(\mathbf{r}) = \frac{[n(\mathbf{r}) + \tilde{m}(\mathbf{r})]^2}{4n(\mathbf{r})}, \quad (4.10a)$$

$$n_0(\mathbf{r}) = \frac{n^2(\mathbf{r}) - \tilde{m}^2(\mathbf{r})}{2n(\mathbf{r})}, \quad (4.10b)$$

$$n_{-1}(\mathbf{r}) = \frac{[n(\mathbf{r}) - \tilde{m}(\mathbf{r})]^2}{4n(\mathbf{r})}. \quad (4.10c)$$

These expressions can be used in the T-F approximated energy density expression [83, 137],

$$e(\mathbf{r}) = U(\mathbf{r})n(\mathbf{r}) + \frac{c_0}{2}n^2(\mathbf{r}) + \frac{c_1}{2}(n_1 - n_{-1})^2 + c_1n_0[n_1 + n_{-1} + 2\sqrt{n_1n_{-1}}\cos\theta_r], \quad (4.11)$$

which leads to the energy density for this state in this limit,

$$e_{PM}(\mathbf{r}) = U(\mathbf{r})n(\mathbf{r}) + \left(\frac{c_0}{2} + \frac{c_1}{2}\right)n^2(\mathbf{r}). \quad (4.12)$$

Note that, though the magnetization density $\tilde{m}(\mathbf{r})$ is required to get the sub-component density expressions, it does not appear in the energy density. As a result, this parameter can be used as a free parameter in the analysis.

Anti-phase-matched state (APM)

If all the sub-components are populated with the relative phase, $\theta_r = \pi$, the stationary state is known as the anti-phase-matched (APM) state. In the previous chapter, we have already discussed the condition of $k(\mathbf{r}) = 1$ case which corresponds to the $p = 0$ and $q = 0$. For completeness, we will discuss this again in this context, starting with Eq.4.1-4.2.

Under the T-F approximation, the phase stationary equations lead to,

$$U(\mathbf{r}) + c_0n(\mathbf{r}) - \mu + c_1(n_1 + n_{-1} - 2\sqrt{n_1n_{-1}}) = 0, \quad (4.13)$$

$$U(\mathbf{r}) + c_0n(\mathbf{r}) - \mu + c_1(n_1 - n_{-1}) + c_1n_0 \left(1 - \sqrt{\frac{n_{-1}(\mathbf{r})}{n_1(\mathbf{r})}}\right) = 0, \quad (4.14)$$

$$U(\mathbf{r}) + c_0n(\mathbf{r}) - \mu - c_1(n_1 - n_{-1}) + c_1n_0 \left(1 - \sqrt{\frac{n_1(\mathbf{r})}{n_{-1}(\mathbf{r})}}\right) = 0, \quad (4.15)$$

where $\cos\theta_r = -1$ corresponding to $\theta_r = \pi$ is used. In a similar manner as done for the

PM state, the addition of the last two equations would provide,

$$U(\mathbf{r}) + c_0 n(\mathbf{r}) - \mu - \frac{c_1 n_0}{2\sqrt{n_1 n_{-1}}} (n_1 + n_{-1} - 2\sqrt{n_1 n_{-1}}) = 0, \quad (4.16)$$

which when compared to Eq.4.13, tells that $n_0 = -2\sqrt{n_1 n_{-1}}$ must be satisfied, which is a clear violation of the assumption Eq.3.1 taken to get to the phase equations. According to the assumption Eq.3.1, $\sqrt{n_m}$ for $m = \pm 1, 0$ are strictly positive for this state. If there is a negative sign in the wave function that is absorbed in the phase factor $\exp(-i\theta_m)$. So the only possible way in which both Eq.4.13 and Eq.4.16 can be correct is when

$$n_1 + n_{-1} - 2\sqrt{n_1 n_{-1}} = 0, \quad (4.17)$$

is satisfied, which means, $\sqrt{n_1} = \sqrt{n_{-1}}$. This is exactly the condition $k(\mathbf{r}) = 1$ we saw in the last chapter. This also tells that the APM state with non-zero magnetization is not a possibility allowed in the absence of the magnetic field.

From Eq.4.13, using the relation we obtained, one can write the total number density,

$$c_0 n(\mathbf{r}) = \mu - U(\mathbf{r}). \quad (4.18)$$

Note that, the sub-component number densities do not come out from the phase equations. All the phase equations, under the relation we obtained in Eq.4.17, only lead to the total number density expression. Not even from the minimization of energy density, the sub-component population can be obtained. So, in the absence of the magnetic fields, the APM state is a one-parameter family of stationary states, with zero magnetization density. The energy density for this state is

$$e_{APM}(\mathbf{r}) = U(\mathbf{r}) \frac{(\mu - U(\mathbf{r}))}{c_0} + \frac{(\mu - U(\mathbf{r}))^2}{2c_0}, \quad (4.19)$$

which we had already obtained in Eq.3.54.

Except for the (A)PM states, results corresponding to other stationary states can be straightforwardly obtained by putting $p = 0$ and $q = 0$ in Table 3.2. For convenience, the T-F approximated number density profiles and the energy density for all the stationary states, in the absence of the magnetic field, are summarized in Table 4.1.

States	Variation of density	Energy density
(1,0,0) <i>F1</i>	$(c_0 + c_1)n(\mathbf{r}) = \mu - U(\mathbf{r})$	$U(\mathbf{r}) \frac{(\mu - U(\mathbf{r}))}{(c_0 + c_1)} + \frac{(\mu - U(\mathbf{r}))^2}{2(c_0 + c_1)}$
(0,1,0) <i>P</i>	$c_0 n(\mathbf{r}) = \mu - U(\mathbf{r})$	$U(\mathbf{r}) \frac{(\mu - U(\mathbf{r}))}{c_0} + \frac{(\mu - U(\mathbf{r}))^2}{2c_0}$
(0,0,1) <i>F2</i>	$(c_0 + c_1)n(\mathbf{r}) = \mu - U(\mathbf{r})$	$U(\mathbf{r}) \frac{(\mu - U(\mathbf{r}))}{(c_0 + c_1)} + \frac{(\mu - U(\mathbf{r}))^2}{2(c_0 + c_1)}$
(1,0,1) <i>AF</i>	$c_0 n(\mathbf{r}) = \mu - U(\mathbf{r})$ and $n_1(\mathbf{r}) = n_{-1}(\mathbf{r})$	$U(\mathbf{r}) \frac{(\mu - U(\mathbf{r}))}{c_0} + \frac{(\mu - U(\mathbf{r}))^2}{2c_0}$
(1,1,1) <i>PM</i>	$(c_0 + c_1)n(\mathbf{r}) = \mu - U(\mathbf{r})$	$U(\mathbf{r}) \frac{(\mu - U(\mathbf{r}))}{(c_0 + c_1)} + \frac{(\mu - U(\mathbf{r}))^2}{2(c_0 + c_1)}$
(1,1,1) <i>APM</i>	$c_0 n(\mathbf{r}) = \mu - U(\mathbf{r})$ and $n_1(\mathbf{r}) = n_{-1}(\mathbf{r})$	$U(\mathbf{r}) \frac{(\mu - U(\mathbf{r}))}{c_0} + \frac{(\mu - U(\mathbf{r}))^2}{2c_0}$

Table 4.1: The T-F approximated number density and energy density expressions for different stationary states in the absence of the magnetic fields are summarized. The states, *MF1*, and *MF2* are not allowed for $p = 0$ and $q = 0$. The ferromagnetic states *F1*, *F2*, and the *PM* state are energetically degenerate, while on the other hand, the polar, *AF*, and *APM* states are energetically degenerate too.

4.1.2 The T-F approximated total energy for three-dimensional isotropic harmonic confinement

Let us assume that the condensate is inside a three-dimensional isotropic harmonic confinement with the trapping frequency, ω . So the trapping potential would be $U(r) = \frac{1}{2}M\omega^2 r^2$, where M is the mass of a condensate particle. We fix the total number of condensate particles, say, N . If we integrate the total density for a stationary state, one gets

the total number of condensate particles, i.e.,

$$\int_0^R n(\mathbf{r})d\mathbf{r} = N, \quad (4.20)$$

where R is the T-F radius.

Let us first focus on the ferromagnetic or the PM state, for which both number density and energy density expressions are identical (see Table 4.1). For these degenerate states,

$$N = \int_0^{R_1} 4\pi r^2 \frac{\mu_1 - M\omega^2 r^2/2}{(c_0 + c_1)} dr = \frac{4\pi M\omega^2 R_1^5}{15(c_0 + c_1)}, \quad (4.21)$$

where R_1 is the T-F radius for these states, and this is related to the chemical potential as, $\mu_1 = M\omega^2 R_1^2/2$ [138]. Using this relation in the Eq.4.21, one can write the chemical potential for these degenerate states as

$$\mu_1 = \frac{M\omega^2}{2} \left[\frac{15(c_0 + c_1)N}{4\pi M\omega^2} \right]^{\frac{2}{5}}. \quad (4.22)$$

Following the same steps one can also get to the chemical potential for the other three degenerate states (polar/ AF/ APM),

$$\mu_2 = \frac{M\omega^2}{2} \left[\frac{15c_0 N}{4\pi M\omega^2} \right]^{\frac{2}{5}}. \quad (4.23)$$

So, for a fixed number of particles, the chemical potential, in general, would be different for different stationary states, as long as the T-F approximated total number density expressions are not identical. Using the chemical potential, now one can integrate the energy density to get the total energy for a stationary state, which can be compared to get the ground state.

The total energy for the PM or the ferromagnetic states can be obtained by integrating

the energy density given in Eq.4.12,

$$\begin{aligned}
 E_{PM/F1/F2} &= \int d\mathbf{r} e_{PM}(\mathbf{r}) \\
 &= \int_0^{R_1} 4\pi r^2 dr \left[\frac{1}{2} M \omega^2 r^2 \frac{\left(\mu_1 - \frac{1}{2} M \omega^2 r^2\right)}{(c_0 + c_1)} + \frac{\left(\mu_1 - \frac{1}{2} M \omega^2 r^2\right)^2}{2(c_0 + c_1)} \right]. \quad (4.24)
 \end{aligned}$$

After using the relation between μ_1 and R_1 and the chemical potential as obtained in Eq.4.22 the total energy can be written in a simplified form,

$$E_{PM/F1/F2} = \frac{2\pi M^2 \omega^4}{21} \left[\frac{15N}{4\pi M \omega^2} \right]^{7/5} (c_0 + c_1)^{2/5}. \quad (4.25)$$

Similarly, one can get to the total energy of the other three degenerate states,

$$E_{APM/AF/P} = \frac{2\pi M^2 \omega^4}{21} \left[\frac{15N}{4\pi M \omega^2} \right]^{7/5} (c_0)^{2/5}. \quad (4.26)$$

Ferromagnetic type spin interaction: When the spin-dependent interaction term, $c_1 < 0$, it is evident that, the total energy of the PM and the ferromagnetic states (Eq.4.25) would be lesser than that of the APM, AF or polar states (Eq.4.26). So, in this case, the PM state or the ferromagnetic states are equally likely to be the ground state.

Anti-ferromagnetic type of spin interaction: As $c_1 > 0$, the APM or AF or the polar states are energetically favored over the ferromagnetic or the PM state. Now, quantitatively speaking, one can take the realistic example of the ^{23}Na condensate for which the spin interaction is of anti-ferromagnetic type. One can assume that the trapping frequency corresponding to the three-dimensional isotropic harmonic confinement is, $\omega = 2\pi \times 100 \text{ Hz}$. The interaction parameters for this case are, $c_1 = 2.415 \times 10^{-19} \text{ Hz } m^3$, and $c_0 = 149.89 \times 10^{-19} \text{ Hz } m^3$, where similar to the previous chapter, we have written energy in units of Hz , which is obtained by dividing the S.I value with h , i.e, Planck's constant. The chemical potential of the APM, polar, and AF state comes out to be $\mu_2 = 1033.15 \text{ Hz}$, which roughly is 50 nK . While the chemical potential is $\mu_1 = 1039.04 \text{ Hz}$ for the PM and ferromagnetic states. Using these values we find the total energy of the PM state, $E_{PM/ferro} \simeq 7.42 \times 10^7 \text{ Hz}$, while the same for the APM state is, $E_{APM} \simeq 7.38 \times 10^7 \text{ Hz}$ for a total number of condensate particle assumed to be $N = 10^5$, for which the T-F approximation is expected to produce accurate results.

Qualitatively, we have understood that under the T-F approximation, not only the APM state but also the polar and the anti-ferromagnetic states are equally likely to be the ground state for the anti-ferromagnetic type of spin interaction. But quantitatively, the energy difference between the ferromagnetic/PM states and the APM state is just 0.5% of that of the PM state. This is an extremely small relative energy difference. In the T-F approximation, the kinetic energy is completely neglected, but even for large condensates, if we do not consider the kinetic energy it can have significant consequences. Needless to say, for a system of a smaller number of particles, where the T-F approximation is known not to be a good one, the kinetic energy contribution will be more pronounced. This warrants a closer look at the situation beyond the T-F approximation.

But before going into that, let us discuss the total energy comparison in one-dimensional harmonic confinement, which we will require for the comparison of the T-F approximated results with the results obtained from the numerical and the variational method, which we will introduce later.

4.1.3 The T-F approximated total energy comparison in quasi-one-dimensional harmonic confinement

We assume the system to be in a quasi-one-dimensional harmonic trap elongated along the x -axis with a trapping frequency ω_x . The trapping frequency in the transverse direction ω_y and ω_z are much greater than that along the x -axis, i.e., $\omega_{yz} > \omega_x$, where $\omega_{yz} \equiv \sqrt{\omega_y \omega_z}$. Quantitatively, we assume the oscillator length scale along the x -axis, $l_x = \sqrt{\hbar/m\omega_x}$ is around $2.965 \mu m$, which is greater than the oscillator length of the transverse direction $l_{yz} = \sqrt{\hbar/m\omega_{yz}}$, that is around $0.59 \mu m$.

Now to get to the total energy of the APM, polar or AF state, one can integrate the energy density,

$$\begin{aligned}
 E_{APM/P/AF} &= \int d\mathbf{r} e_{APM}(\mathbf{r}) \\
 &= \int_{-R_2}^{R_2} \pi l_{yz}^2 dx \left[\frac{1}{2} M \omega_x^2 x^2 \frac{(\mu_1 - \frac{1}{2} M \omega_x^2 x^2)}{c_0} + \frac{(\mu_1 - \frac{1}{2} M \omega_x^2 x^2)^2}{2c_0} \right], \quad (4.27)
 \end{aligned}$$

which leads to

$$E_{APM/P/AF}^{1D} = \frac{\pi l_{yz}^2}{5} M^2 \omega_x^4 \left[\frac{3N}{2\pi l_{yz}^2 M \omega_x^2} \right]^{5/3} (c_0)^{2/3}. \quad (4.28)$$

Using the energy density for the ferromagnetic or the PM state, the total energy of these states in the 1-D trapping can be written as

$$E_{PM/F1/F2}^{1D} = \frac{\pi l_{yz}^2}{5} M^2 \omega_x^4 \left[\frac{3N}{2\pi l_{yz}^2 M \omega_x^2} \right]^{5/3} (c_0 + c_1)^{2/3}. \quad (4.29)$$

Ferromagnetic type spin interaction: Comparing the total energy of the stationary states, it is easy to see that, for $c_1 < 0$, the PM or the ferromagnetic states are energetically favored over the APM state.

Anti-ferromagnetic type of spin interaction: Qualitatively the APM, polar, or the AF state are energetically favored over the other states to become the ground state for condensates with the anti-ferromagnetic type of spin-dependent interaction. But taking the realistic example of ^{23}Na , as done in the case of the 3-D trapping geometry earlier, we find that the total energy comes out to be, $E_{APM/P/AF}^{1D} \simeq 8.648 \times 10^8 Hz$, while for the PM and ferromagnetic states, it is $E_{PM/F1/F2}^{1D} \simeq 8.74 \times 10^8 Hz$, for $N = 10^5$ number of condensate particles. It shows that even if the APM state or the other two degenerate states win in this situation, the relative energy difference with the PM state is only 1%. This is very small and independent of the total number N . So, it is only natural to suspect that consideration of the full profile of the condensate along with the kinetic energy might affect this conclusion of the T-F approximation. Also, for small condensates, where the T-F approximation is not at all accurate, we need to go beyond the T-F approximation to see whether the conclusion about the condensate ground state remains unaffected.

4.2 Variational Method

In this section, we develop a multi-modal variational method that will let us go beyond the capability of the T-F approximation. We will focus on the scenario already discussed in the previous section, where we saw that under 3-D or quasi-1-D harmonic confinement, for the condensate with an anti-ferromagnetic type spin interaction, the polar, AF and the APM states are favored to be the ground state with a very small relative energy difference with the other three degenerate states (F1/ F2/ PM) in the absence of magnetic field.

The variational method will let us get a full profile of the condensate in contrast to the T-F profile, which might tell a different story.

We will start with the 3-D case, and discuss the method in a very detailed manner. Later we will come to the quasi-1-D case which will be helpful in comparing all the results with the numerical simulation.

4.2.1 3-D isotropic harmonic confinement: Variational approach

First, we start with the phase equations, under stationarity condition in the absence of the magnetic field,

$$\left(-\frac{\hbar^2 \nabla^2}{2M} + U(\mathbf{r}) + c_0 n - \mu + c_1 (n_1 + n_{-1} + 2\sqrt{n_{-1}n_1} \cos \theta_r) \right) \sqrt{n_0(\mathbf{r})} = 0, \quad (4.30)$$

$$\left(-\frac{\hbar^2 \nabla^2}{2M} + U(\mathbf{r}) + c_0 n - \mu \pm c_1 (n_1 - n_{-1}) \right) \sqrt{n_0(\mathbf{r})} + c_1 n_0 \left(\sqrt{n_{\pm 1}(\mathbf{r})} + \sqrt{n_{\mp 1}(\mathbf{r})} \cos \theta_r \right) = 0. \quad (4.31)$$

To write these equations in a dimensionless form, we rescale the interaction parameter and the number densities as,

$$c_0 = (4/3)\pi l_0^3 \lambda_0 \hbar \omega, \quad c_1 = (4/3)\pi l_0^3 \lambda_1 \hbar \omega, \quad (4.32)$$

$$u_m = (4/3)\pi l_0^3 \lambda_0 n_m, \quad r = l_0 \eta; \quad (4.33)$$

where, $l_0 = \sqrt{\hbar/(m\omega)}$ is the oscillator length scale [139] and naturally $\hbar\omega$ becomes the energy scale. After these transformations, λ_0 , and λ_1 correspond to the spin-independent and spin-dependent interaction coefficients respectively. Whereas, η is the radial distance from the trap center and u_m is the sub-component density in dimensionless form.

Now, the phase equations for the 3-D isotropic harmonic confinement can be written in a dimensionless form as

$$\left\{ -\frac{1}{2} \frac{1}{\eta^2} \frac{d}{d\eta} \left(\eta^2 \frac{d}{d\eta} \right) + \frac{1}{2} \eta^2 + u - \mu' + \lambda_1' (u_1 + u_{-1} + 2\sqrt{u_{-1}u_1} \cos \theta_r) \right\} \sqrt{u_0} = 0, \quad (4.34)$$

$$\left\{ -\frac{1}{2} \frac{1}{\eta^2} \frac{d}{d\eta} \left(\eta^2 \frac{d}{d\eta} \right) + \frac{1}{2} \eta^2 + u - \mu' \pm \lambda'_1 (u_1 - u_{-1}) \right\} \sqrt{u_{\pm 1}} + \lambda'_1 u_0 (\sqrt{u_{\pm 1}} + \sqrt{u_{\mp 1}} \cos \theta_r) = 0, \quad (4.35)$$

where, λ'_1 is the ratio of the spin-dependent and spin-independent interaction coefficients, i.e., $\lambda'_1 = \lambda_1/\lambda_0$, and μ' is also rescaled as, $\mu' = \mu/(\hbar\omega)$. In these equations, u is the total number density, which is the sum of the sub-component densities, i.e., $u = u_1 + u_0 + u_{-1}$.

In the high-density region, close to the trap center, the kinetic energy contribution is very small compared to the interaction energy (non-linear terms), and we can neglect the kinetic energy contribution. So, close to the trap center, one neglects the Laplacian terms in Eq.4.34-4.35, and corresponding sub-component densities can be found out for a stationary state as a function of the parameter μ' and the radial distance η . Now at the low-density region of the trap, far from the trap center, the kinetic energy will have a significant contribution and we assume a Gaussian tail of number density in this region, in analogy with the first few lowest energy states under harmonic potential.

We impose the condition that the wave function (by this we mean the square root of the sub-component number density u_m) in the high-density and in the low-density region match smoothly at $\eta = \eta_0$ i.e.,

$$\begin{aligned} u^{in}(\eta) &= f(\mu', \eta) & \text{for } \eta < \eta_0, \\ u^{out}(\eta) &= (a + c\eta + d\eta^2) \exp\left(-\frac{\eta^2}{b}\right) & \text{for } \eta \geq \eta_0. \end{aligned} \quad (4.36)$$

We additionally impose that not only the wave function, but also its first, second, and third derivatives on both sides should be equal at $\eta = \eta_0$.

Now, the exact functional form $f(\mu', \eta)$, which describes the number density in the high-density region of the trap is different for different stationary states. The solution of the Eq.4.34-4.35 after neglecting the Laplacian term provides the $f(\mu', \eta)$ which we would see later when we discuss the variational method for the PM state or the polar state. Following the smooth-matching-condition, a , b , c , and d can be written in terms of μ' and the matching point, η_0 . If we integrate the sub-component densities and sum it up this should provide the total number of condensate particles, N . This can be used to write the parameter μ' as a function of N and the matching point η_0 . As a result, for a given number of condensate particles, the total energy can be calculated easily, which becomes

a function of η_0 . Now, from the minimization of the total energy, the free parameter η_0 is fixed. Then, by backtracking, all the sub-component densities can be expressed analytically.

Note that, it is essential to impose smoothness up to the third derivative, which ensures that the kinetic energy on both sides of η_0 matches smoothly as well. This, as a result, allows for a smooth energy density profile. The procedure we discussed so far, takes into account all the sub-component densities, and in general, the coefficients a , b , c , and d are not always identical for different sub-components. Hence, this variational approach is truly multi-modal and one can expect this to be applicable even if the sub-components do not follow a single spatial distribution.

We will apply this method to get to the total energy of the polar state and the PM state. This method does not break the degeneracy between the PM and the ferromagnetic state. Similarly, the inherent degeneracy between the polar, AF, and APM states is also not lifted by this method. So, we choose only the polar and the PM state out of the two sets of degenerate states and apply the variational method for these stationary states in the following.

Polar state

For this state, only the sub-component corresponding to $m = 0$ is populated and the other two are empty. So, in this state, $u = u_0$ and $u_{\pm 1} = 0$. Now in the high-density region, one can neglect the Laplacian term of Eq.4.34, which leads to

$$u_{pol}^{in}(\eta) = \mu' - \eta^2/2. \quad (4.37)$$

Note that, for the polar state, this is the expression corresponding to the function $f(\mu', \eta)$ in Eq.4.36. Using this expression in the matching condition of the number density at the matching point η_0 , i.e., $\sqrt{u_{pol}^{in}(\eta_0)} = \sqrt{u_{pol}^{out}(\eta_0)}$, one can write the unknown coefficient a in Eq.4.36 as a function of the other unknowns, b , c , d and η_0 ,

$$a = \left(\mu' - \eta_0^2/2\right) \exp\left(\frac{\eta_0^2}{b}\right) - c\eta_0 - d\eta_0^2. \quad (4.38)$$

Similarly from the matching condition for the slope of $\sqrt{u_{pol}(\eta)}$ in outer and inner region at η_0 gives,

$$d = \exp\left(\frac{\eta_0^2}{b}\right) \left(\frac{\mu' - \eta_0^2/2}{b} - \frac{1}{2}\right) - \frac{c}{2\eta_0}. \quad (4.39)$$

The second derivative matching condition gives c in terms of b and η_0 ,

$$c = \frac{2\exp\left(\frac{\eta_0^2}{b}\right) \eta_0^3 (2b - 2\mu' + \eta_0^2)}{b^2}. \quad (4.40)$$

The matching conditions have reduced the number of unknown coefficients. The remaining parameter b is obtained by matching the third derivative,

$$b = \frac{1}{12} \left(6\mu' - 9\eta_0^2 + \sqrt{36\mu'^2 - 12\mu'\eta_0^2 + 33\eta_0^4}\right), \quad (4.41)$$

where, the parameter b is written only in terms of the parameter μ' and η_0 . Now using the expression of b , the parameter c (in Eq.4.40) can also be expressed in terms of the parameters μ' and η_0 only. The same holds true for the parameters a and d as well. Therefore, after the matching conditions are imposed, the number density in the outer region becomes a function of the parameters μ' and η_0 only. To determine μ' , one can use,

$$\int_0^{\eta_0} u_{pol}^{in} \eta^2 d\eta + \int_{\eta_0}^{\infty} u_{pol}^{out} \eta^2 d\eta = \lambda_0 N/3, \quad (4.42)$$

which is the same as $\int_0^{\infty} n_{pol}(r) 4\pi r^2 dr = N$, written in the dimensionless form. Following the integration and further simplification one gets to,

$$\begin{aligned} & \frac{1}{192k^{5/2}} \left[12\sqrt{k}\eta_0 \left(168k\mu'^3 + 4\mu'^2(-113k + 336\mu')\eta_0^2 + 18(23k - 176\mu')\mu'\eta_0^4 + 216\eta_0^8 \right. \right. \\ & + (53k + 816\mu')\eta_0^6 \left. \right) + 6 \exp\left(\frac{12\eta_0^2}{k}\right) \sqrt{3\pi} \left(336k\mu'^4 + 128\mu'^3(-10k + 21\mu')\eta_0^2 \right. \\ & + 8(269k - 1168\mu')\mu'^2\eta_0^4 + 16\mu'(-115k + 872\mu')\eta_0^6 + (473k - 7904\mu')\eta_0^8 + 1464\eta_0^{10} \left. \right) \\ & + \exp\left(\frac{12\eta_0^2}{k}\right) k\sqrt{3\pi} \left(-168k\mu'^3 + 4(125k - 336\mu')\mu'^2\eta_0^2 + 2\mu'(-311k + 1776\mu')\eta_0^4 \right. \\ & \left. \left. + 3(61k - 784\mu')\eta_0^6 + 456\eta_0^8 \right) \operatorname{Erf}\left(\frac{2\sqrt{3}\eta_0}{\sqrt{k}}\right) \right] + \frac{\mu'\eta_0^3}{3} - \frac{\eta_0^5}{10} = \lambda_0 N/3, \end{aligned} \quad (4.43)$$

where, $k = 6\mu' - 9\eta_0^2 + \sqrt{36\mu'^2 - 12\mu'\eta_0^2 + 33\eta_0^4}$ and $\text{Erf}\left(\frac{2\sqrt{3}\eta_0}{\sqrt{k}}\right)$ is the error function. Note that, the spin-independent interaction coefficient λ_0 , and the total number of condensate particles, N are fixed depending upon the type of condensate we are interested in. Thus, using Eq.4.43, the μ' can be numerically estimated for different values of η_0 .

For a particular condensate with a given N , the total energy of the polar state can be calculated for different values of η_0 by using the corresponding estimation of $\mu'(\eta_0)$ from Eq.4.43. The energy density can be written as,

$$e_{pol}(u(\eta)) = \frac{3\hbar\omega}{2\lambda_0} \left[-\sqrt{u(\eta)} \frac{1}{\eta^2} \frac{d}{d\eta} (\eta^2 \frac{d}{d\eta} \sqrt{u(\eta)}) + \eta^2 u(\eta) + u^2(\eta) \right], \quad (4.44)$$

which assumes this form in the dimensionless version. Now, by integrating the energy density, i.e.,

$$E_{pol}(\eta_0) = \int_0^{\eta_0} d\eta \eta^2 e_{pol}(u^{in}(\eta)) + \int_{\eta_0}^{\infty} d\eta \eta^2 e_{pol}(u^{out}(\eta)), \quad (4.45)$$

the total energy is obtained that can be calculated for varying values of the matching point.

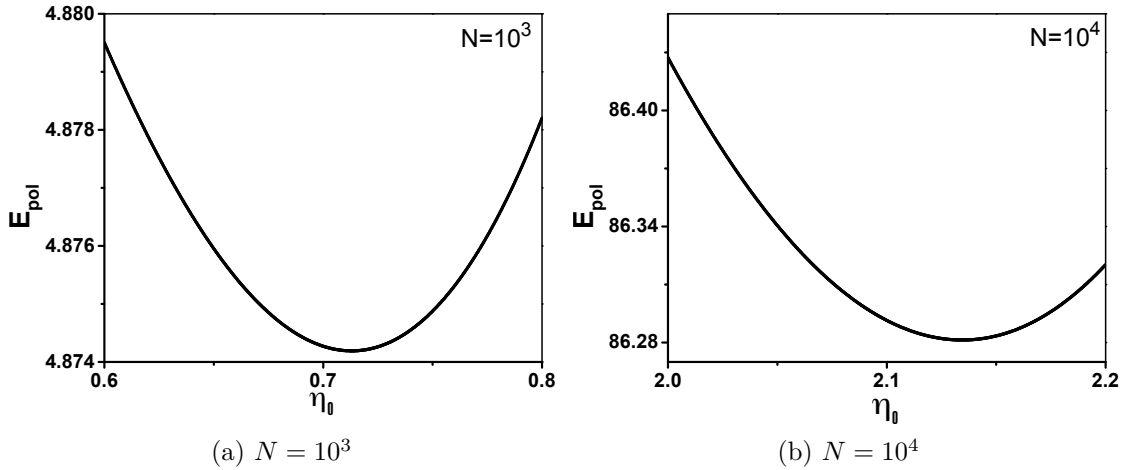


Figure 4.1: Total energy of the polar state with varying η_0 (the matching point) shows the existence of minima, which fixes η_0 corresponding to the energy minimum. (a) The total number of condensate particles is 1,000 and the energy minimum determines the matching point at $\eta_0 \simeq 0.713$ while the T-F radius is approximately 1.81. (b) For 10,000 condensate particles, the total energy is minimum at $\eta_0 \simeq 2.135$ which has shifted more towards the T-F radius, which in this case is $\simeq 2.868$. To get the actual energy values, one has to multiply $3\hbar\omega/(2\lambda_0)$ with the energy values shown in this figure. For the purpose of visualization, this scaling factor is used in all subsequent figures (of the 3-D case).

By minimizing the total energy with respect to this matching point, i.e., $\frac{dE_{pol}(\eta_0)}{d\eta_0} = 0$,

one fixes of η_0 as well as the minimum possible total energy for the polar state.

Phase-matched state

The PM state is a multi-component state, so the variational method would be done on the sub-components, following a similar approach shown for the polar state. Firstly, to get the sub-component densities for the PM state in the high-density region, the kinetic energy contribution in Eq.4.34-4.35 can be neglected in comparison to the interactions. Note that, in the previous section, we discussed the PM state under the T-F approximation, where we saw that the magnetization density becomes a degeneracy parameter for the PM state, as it does not come in the energy expression. Similarly, in the variational method, the magnetization density does not affect the total energy of the PM state. So for simplicity, we will stick to $\tilde{m} = 0$. Following the same procedure, the sub-component densities are obtained from Eq.4.34-4.35 in terms of the total number density in the high-density region,

$$u_{\pm 1}^{in} = u^{in}/4, \quad u_0^{in} = u^{in}/2, \quad (4.46)$$

where u_m^{in} for $m = 1, 0, -1$ represents the sub-component densities close to the trap center. The total density u^{in} , in this region is,

$$u^{in} = \frac{\mu' - \eta^2/2}{(1 + \lambda_1')} \quad \text{for } \eta \geq \eta_0. \quad (4.47)$$

According to the assumption we have taken, the sub-component densities in the outer region where the kinetic energy contribution is significant are,

$$u_m^{out}(\eta) = (a_m + c_m\eta + d_m\eta^2) \exp(-\eta^2/b_m) \quad \text{for } \eta \geq \eta_0. \quad (4.48)$$

Employing the smooth matching condition of the wave function and its first three derivatives of the high-density and low-density expressions, the coefficients a_m , b_m , c_m and d_m can be obtained for the PM state, following the same procedure as done for the polar state. The coefficients for the sub-components follow,

$$b_0 = b_{\pm 1} = b, \quad (4.49a)$$

$$c_{\pm 1} = \frac{c_0}{2} = \frac{c}{4(1 + \lambda'_1)}, \quad (4.49b)$$

$$d_{\pm 1} = \frac{d_0}{2} = \frac{d}{4(1 + \lambda'_1)}, \quad (4.49c)$$

$$a_{\pm 1} = \frac{a_0}{2} = \frac{a}{4(1 + \lambda'_1)}, \quad (4.49d)$$

where the parameters a , b , c , d are found out to be of similar expression as with Eq.4.38-4.41, where μ' is different from that of the polar state. The parameter μ' for the PM state can be obtained from the equation giving the total number of particles,

$$\int_0^{\eta_0} u_{PM}^{in} \eta^2 d\eta + \int_{\eta_0}^{\infty} u_{PM}^{out} \eta^2 d\eta = \lambda_0 N/3, \quad (4.50)$$

where, $u_{PM}^{out} = u_1^{out}(\eta) + u_0^{out}(\eta) + u_{-1}^{out}(\eta)$ is the total number density at $\eta \geq \eta_0$. Following the integration one arrives at,

$$\begin{aligned} & \frac{1}{192k^{5/2}} \left[12\sqrt{k}\eta_0 \left(168k\mu'^3 + 4\mu'^2(-113k + 336\mu')\eta_0^2 + 18(23k - 176\mu')\mu'\eta_0^4 + 216\eta_0^8 \right. \right. \\ & + (53k + 816\mu')\eta_0^6 \left. \right) + 6 \exp\left(\frac{12\eta_0^2}{k}\right) \sqrt{3\pi} \left(336k\mu'^4 + 128\mu'^3(-10k + 21\mu')\eta_0^2 \right. \\ & + 8(269k - 1168\mu')\mu'^2\eta_0^4 + 16\mu'(-115k + 872\mu')\eta_0^6 + (473k - 7904\mu')\eta_0^8 + 1464\eta_0^{10} \left. \right) \\ & + \exp\left(\frac{12\eta_0^2}{k}\right) k\sqrt{3\pi} \left(-168k\mu'^3 + 4(125k - 336\mu')\mu'^2\eta_0^2 + 2\mu'(-311k + 1776\mu')\eta_0^4 \right. \\ & \left. \left. + 3(61k - 784\mu')\eta_0^6 + 456\eta_0^8 \right) \text{Erf}\left(\frac{2\sqrt{3}\eta_0}{\sqrt{k}}\right) \right] + \frac{\mu'\eta_0^3}{3} - \frac{\eta_0^5}{10} = (1 + \lambda'_1)\lambda_0 N/3, \end{aligned} \quad (4.51)$$

where, $k = 6\mu' - 9\eta_0^2 + \sqrt{36\mu'^2 - 12\mu'\eta_0^2 + 33\eta_0^4}$. This equation is similar to Eq.4.43 except for the coefficient $(1 + \lambda'_1)$ on the right side of this equation. The parameter μ' for the PM state can be estimated for different values of N and η_0 using this equation.

The energy density for the PM state for the 3-D harmonic confinement is

$$e_{PM} = \frac{3\hbar\omega_x}{2\lambda_0} \left[-\sqrt{u(\eta)} \frac{1}{\eta^2} \frac{d}{d\eta} (\eta^2 \frac{d}{d\eta} \sqrt{u(\eta)}) + \eta^2 u(\eta) + (1 + \lambda'_1) u^2(\eta) \right]. \quad (4.52)$$

Thus, one can calculate the total energy for the PM state by simply integrating the

energy density,

$$E_{PM}(\eta_0) = \int_0^{\eta_0} d\eta \eta^2 e_{PM}(u(\eta)) + \int_{\eta_0}^{\infty} d\eta \eta^2 e_{PM}(u(\eta, \eta_0)). \quad (4.53)$$

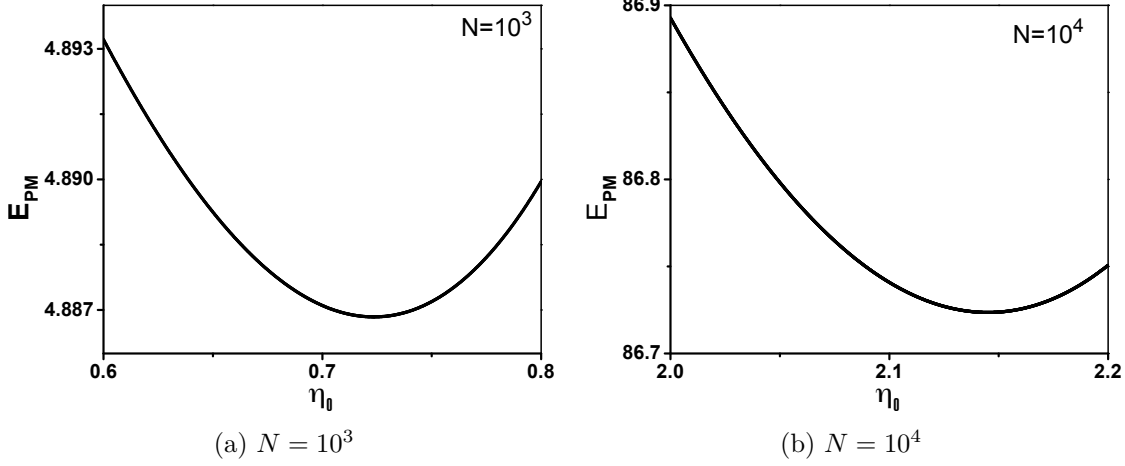


Figure 4.2: Total energy of the PM-state for different values of η_0 . The minimization of total energy fixes the free parameter η_0 , for example, (a) for 1,000 condensate particles, corresponding to the minimum value of total energy (4.887), η_0 is fixed at 0.724 (approx.) while the T-F radius is approximately at 1.815. (b) Similarly, for 10,000 condensate particles, we find at $\eta_0 \simeq 2.145$, the total energy is minimized at an approximate value of 86.724, while the T-F radius, in this case, is 2.877 (approx.).

Now, the minimization of energy with respect to the matching point η_0 gives the energy of the PM state that fixes the value of η_0 as well. This, in turn, gives μ' . Subsequently, one can write analytical expressions corresponding to the sub-component number densities.

4.2.2 3-D isotropic harmonic confinement: Results

For a condensate with an anti-ferromagnetic type of spin interaction in a 3-D isotropic harmonic confinement, we saw that the T-F approximation estimates the relative energy difference between the PM (or the ferromagnetic states) and the polar (or APM or AF) state ($(E_{PM}^{TF} - E_{pol}^{TF})/E_{PM}^{TF}$) is only about $\simeq 0.5\%$ with polar state winning energetically in the absence of the magnetic field (at $p = 0$ and $q = 0$). This relative energy difference does not change with the condensate size, i.e., the number of condensate particles N . So our main purpose to employ the variational method (VM) is to see the effect of the inclusion of kinetic energy on this small energy difference as well as to check whether it depends on N . The relative energy difference as estimated from the T-F approximation

is very small, and there is a possibility that the inclusion of the correction might favor the PM state to win energetically.

Particle Number	Polar/APM/AF	PM state
$N = 1000$	$E^{TF} = 3.0267, E^{var} = 4.8742$	$E^{TF} = 3.046, E^{var} = 4.8868$
$N = 5000$	$E^{TF} = 28.8084, E^{var} = 34.994$	$E^{TF} = 28.993, E^{var} = 35.1525$
$N = 10000$	$E^{TF} = 76.0257, E^{var} = 86.2813$	$E^{TF} = 76.513, E^{var} = 86.7235$
$N = 15000$	$E^{TF} = 134.1184, E^{var} = 147.8625$	$E^{TF} = 134.9779, E^{var} = 148.6607$

Table 4.2: Total energy as obtained from the VM and the T-F approximation for both the polar and the PM state are shown for the different numbers of condensate particles. The energy scale of $3\hbar\omega/(2\lambda_0)$ is used, multiplying this scale with the energy values shown here, will produce the actual total energy. Here, E^{var} denotes the total energy obtained from VM and E^{TF} is the T-F approximated total energy. All the values given are mostly rounded off to the last decimal place.

For a wide range of condensate particles in an experimentally achievable regime (e.g. $N = 1000, 3000, 5000, 7000, 10000, 15000$), we employ the VM. For the 3-D isotropic harmonic confinement, where we stick to the same trapping frequency, $\omega = 2\pi \times 100 \text{ Hz}$, as used in the T-F analysis. The interaction parameters are, $\lambda_0 = 3.88164 \times 10^{-3}$ and $\lambda_1 = 0.0161$, which corresponds to the ^{23}Na condensate in the dimensionless form. Some of the numerical values of the total energy corresponding to the PM and the polar state, that we obtained from the T-F approximation (in this dimensionless form) and the VM are summarized in Table 4.2. Both for the PM and the polar state, the correction introduced by the variational method is relevant as the total energy estimated from the VM is significantly different from the T-F estimation. Specifically for smaller condensates with particle numbers (we went as low as, $N = 500$), there is a drastic difference between the VM and the T-F approximated total energies.

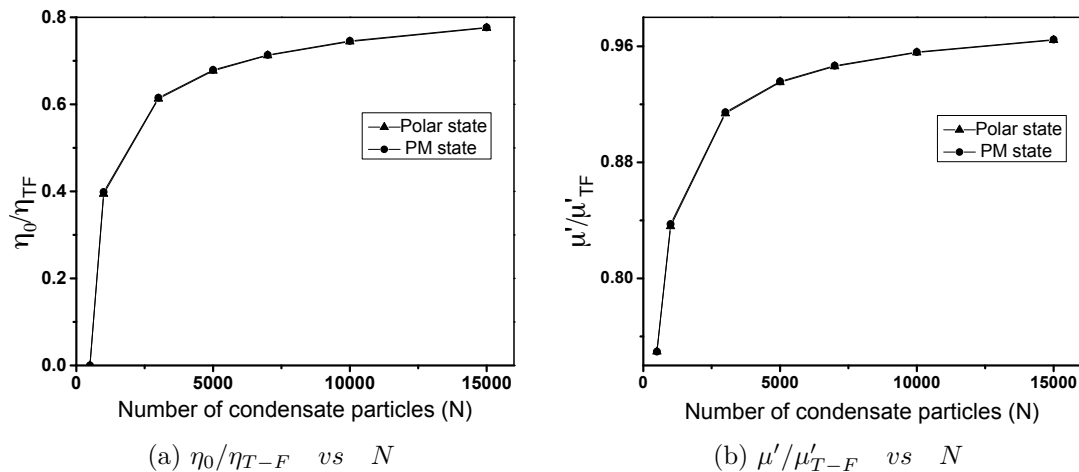


Figure 4.3: (a) The ratio of the matching point, η_0 , and the T-F radius η_{TF} for different condensate particles, gives important information about the accuracy of the T-F approximated results. As the number of condensate particles is increased, the matching point shifts towards the T-F radius for both polar and PM states. It shows the relevance of the VM when the condensate particles are less than 10,000, given our choice of the parameter values (ω , λ_0 and λ'_1). (b) The ratio of μ' obtained via the VM and the T-F approximation increases with the number of condensate particles. The number density at the center of the trap, which is the peak density, is proportional to μ' with the same proportionality constant for both the VM and the T-F approximation. This ratio approaches unity as the condensate becomes larger, while for condensates with a smaller number of particles, the μ' obtained from the VM deviates significantly from that of the T-F approximation.

The matching point η_0 , where the Gaussian tail matches smoothly with the number density of the high-density region, moves toward the T-F radius as the number of condensate particles is increased. This means, for large condensates, the T-F approximation gives accurate results (Fig.4.3(a)). A very similar trend is also followed by the μ' estimated in the VM (Fig.4.3(b)). For small condensates, the VM estimated μ' is lesser than that of T-F estimation. This is due to a significant contribution of the Gaussian tail, as the matching point η_0 is closer to the trap center. The ratio of the parameter μ' obtained from the VM and the T-F approximation also signifies the ratio of the peak density, which is number density (estimated by these two methods) at the center of the trap (Fig.4.3(b)).

We found that the VM estimates the matching point to be in extremely close proximity to the trap center or might be equal to zero ($\eta_0 \simeq 0$) for condensates with $N \leq 521$. Note that, this is due to the specific choice of the trapping geometry, and depending on that the above-mentioned number can be large as well, if the trapping frequency is reduced. For this situation, the VM estimates an analytical condensate profile. In Section 4.2.5, we will compare this predicted profile with the computationally obtained condensate profile

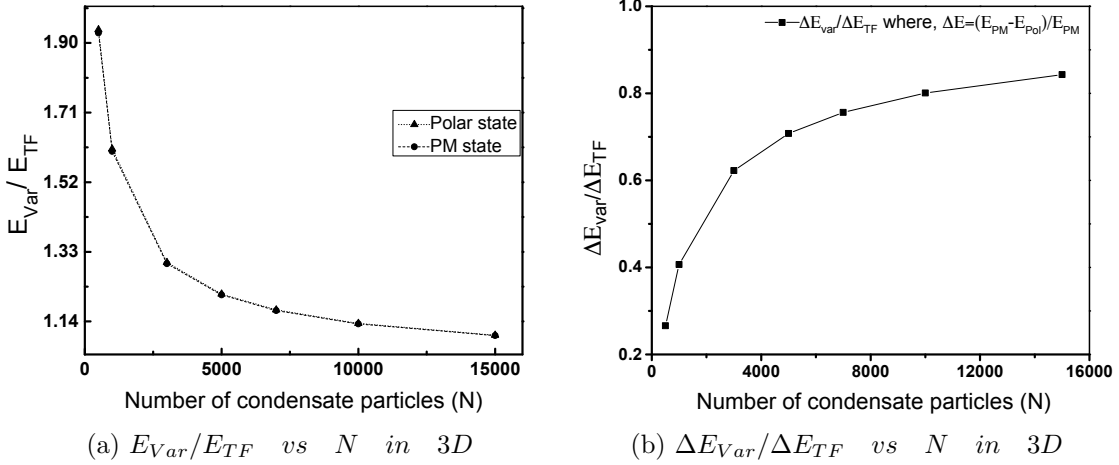


Figure 4.4: (a) The ratio of total energy estimated by the VM and the T-F approximation for polar/ APM/ AF and PM/ ferromagnetic states. The effect of the VM on the total energy is similar for both stationary states. For small condensates, the energy ratio is almost twice. This depicts the significance of using the VM instead of the T-F approximation. (b) The ratio of relative energy difference of PM state and polar state (defined as $\Delta E = (E_{PM} - E_{Pol})/E_{PM}$) as obtained from the VM and the T-F approximation, for different condensate particles clearly depicts that consideration of the full number density profile, and the inclusion of the kinetic energy do not change the fact that under 3-D harmonic trapping, polar/ AF/ APM state still energetically favorable than the ferromagnetic/ PM-state. The inclusion of the correction reduces the energy difference between the polar and the PM state by a significant margin, which is more pronounced for condensates with a smaller number of particles.

for $N = 500$.

Now coming to the total energy, the VM is really significant, especially for condensates with smaller particle numbers, where we find that the total energy estimated for both PM and polar/APM/AF state is almost twice ($N = 500$) of that estimated using the T-F approximation (Fig.4.4(a)). Importantly, the relative energy difference between the polar and the PM state (which was $\simeq 0.5\%$ in the T-F approximation) becomes almost $\simeq 0.16\%$ for smaller condensates with $N = 500$ and $\simeq 0.26\%$ for $N = 1000$. For larger condensates, the energy difference is reduced as well, in comparison to the T-F estimation. Still, the polar state, the APM state, or the AF state is equally likely to be the ground state (Fig.4.4(b)).

4.2.3 Quasi-1-D harmonic confinement: Variational approach

The variational method also applies in quasi-one-dimensional geometry. In this section, for completeness, we will briefly discuss the procedure, which is similar to that of three-

dimensional confinement. To write the phase equations in a dimensionless form, for a quasi-one-dimensional condensate, the interaction parameter and the number densities are scaled as,

$$c_0 = 2\pi l_{yz}^2 l_x \lambda_0^{1D} \hbar \omega_x, \quad c_1 = 2\pi l_{yz}^2 l_x \lambda_1^{1D} \hbar \omega_x, \quad (4.54)$$

$$u_m = 2\pi l_{yz}^2 l_x \lambda_0^{1D} n_m, \quad r = l_x \zeta; \quad (4.55)$$

where ω_x is the trapping frequency in the direction of elongation and $\omega_{yz} = \sqrt{\omega_y \omega_z}$ is the geometric mean of the trapping frequencies in the transverse direction. The corresponding oscillator length scales are defined as, $l_x^2 = \hbar/(m\omega_x)$ and $l_{yz}^2 = \hbar/(m\omega_{yz})$, and N is the total number of particles in the condensate. As a result, the parameters λ_0^{1D} , λ_1^{1D} , ζ and u_m become all dimensionless. Note that, we are considering the condensate to be elongated in x direction as the harmonic trapping is far lesser than the geometric mean of the trapping frequencies along the other two directions i.e. $\omega_x \ll \omega_{yz}$.

Thus, the phase-stationary GP equation reads,

$$\left\{ -\frac{1}{2} \frac{d^2}{d\zeta^2} + \frac{1}{2} \zeta^2 + u - \mu' + \lambda_1'' (u_1 + u_{-1} + 2\sqrt{u_{-1}u_1} \cos \theta_r) \right\} \sqrt{u_0} = 0, \quad (4.56)$$

$$\left\{ -\frac{1}{2} \frac{d^2}{d\zeta^2} + \frac{1}{2} \zeta^2 + u - \mu' \pm \lambda_1'' (u_1 - u_{-1}) \right\} \sqrt{u_{\pm 1}} + \lambda_1'' u_0 (\sqrt{u_{\pm 1}} + \sqrt{u_{\mp 1}} \cos \theta_r) = 0, \quad (4.57)$$

in the dimensionless form where, $\lambda_1'' = \lambda_1^{1D}/\lambda_0^{1D}$. The parameter μ is rescaled as, $\mu' = \mu/(\hbar\omega_x)$. Note that, the equations are exactly similar to those for 3-D except for the Laplacian term. Due to rescaling, the interaction parameters would be different in 1-D according to the specific choice we have taken in Eq.4.54.

Following a similar approach we had taken in case of 3-D condensate, we assume the number densities as,

$$\begin{aligned} u^{in}(\zeta) &= f(\mu', \zeta) \quad \text{for } |\zeta| < |\zeta_0|, \\ u^{out}(\zeta) &= (a + c |\zeta| + d \zeta^2) \exp\left(-\frac{\zeta^2}{b}\right) \quad \text{for } |\zeta| \geq |\zeta_0|. \end{aligned} \quad (4.58)$$

The square root of the number density and its derivatives on both sides should be equal at $\zeta = \zeta_0$. The functional form $f(\mu', \zeta)$ is different for different stationary states and can be found from the solution of the Eq.4.56-4.57 after neglecting the kinetic energy term. This is due to the fact that the kinetic energy contribution is assumed to be lesser in

comparison to the interaction terms at the trap center. The parameter ζ is the position coordinate in the dimensionless form while the center of the trap is at $\zeta = 0$. As it is a 1-D trapping geometry, ζ can be positive and negative. Considering the symmetry of the problem, only the positive values for ζ and ζ_0 are taken in the subsequent analysis to simplify notations.

Polar state:

Similar to the 3-D condensate, the number density for the high-density region is found out,

$$u_{pol}^{in}(\zeta) = \mu' - \zeta^2/2 \quad \text{for } |\zeta| < |\zeta_0|. \quad (4.59)$$

Using the smooth matching condition, $\zeta = \zeta_0$ we find all the coefficients a, b, c, d ,

$$d = \exp\left(\frac{12\zeta_0^2}{k}\right) \frac{(k - 12\mu')\mu' - (k - 20\mu')\zeta_0^2 - 13\zeta_0^4}{2\zeta_0^2(-2\mu' + \zeta_0^2)}, \quad (4.60a)$$

$$b = \frac{k}{12} \quad (4.60b)$$

$$c = 48\zeta_0^3 \exp\left(\frac{12\zeta_0^2}{k}\right) \frac{k - 12(\mu' - \zeta_0^2/2)}{k^2}, \quad (4.60c)$$

$$a = \exp\left(\frac{12\zeta_0^2}{k}\right) \frac{42\zeta_0^4 - 4(k - 14\mu' + 22\zeta_0^2)\mu' + 3k\zeta_0^2}{4(2\mu' - \zeta_0^2)}, \quad (4.60d)$$

where, $k = 6\mu' - 9\zeta_0^2 + \sqrt{36\mu'^2 - 12\mu'\zeta_0^2 + 33\zeta_0^4}$. Now if we integrate the sub-component densities it should produce the total number of particles, which in this non-dimensional version can be written as

$$\int_0^{\zeta_0} u_{pol}^{in} d\zeta + \int_{\zeta_0}^{\infty} u_{pol}^{out} d\zeta = \lambda_0^{1D} N. \quad (4.61)$$

This equation helps to provide the estimation of μ' for a particular value of the matching point ζ_0 and N . Following the integration and simplifying further,

$$\begin{aligned} & \frac{1}{16\sqrt{3}k^2} \left[4\sqrt{3}\zeta_0 \left(12k\mu'^2 + 4\mu'(-5k + 24\mu')\zeta_0^2 - 216\zeta_0^6 + (-53k + 384\mu')\zeta_0^4 \right) \right. \\ & \quad - \exp\left(\frac{12\eta_0^2}{k1}\right) \sqrt{k\pi} \left(-60k\mu'^2 + 20(7k - 24\mu')\mu'\zeta_0^2 + (29k - 576\mu')\zeta_0^4 \right. \\ & \quad \left. \left. + 408\zeta_0^6 \right) \text{Erfc}\left(\frac{2\sqrt{3}\zeta_0}{\sqrt{k}}\right) \right] + \mu'\zeta_0 - \zeta_0^3/6 = \lambda_0^{1D} N, \end{aligned} \quad (4.62)$$

where, $\text{Erfc}((2\sqrt{3}\zeta_0)/\sqrt{k})$ is the complementary error function and k is defined earlier. Here λ_0^{1D} is different from the 3-D condensate due to the scaling factor in Eq.4.54. From the above relation, μ' can be estimated for different values of ζ_0 and N . Though the procedure is similar, the equation for determining μ' is different from the 3-D condensate.

The polar-state energy density,

$$e_{pol}(u(\zeta)) = \frac{\hbar\omega_x}{2\lambda_0^{1D}} \left(-\sqrt{u(\zeta)} \frac{d^2}{d\zeta^2} \sqrt{u(\zeta)} + \zeta^2 u(\zeta) + u^2(\zeta) \right), \quad (4.63)$$

can be integrated to get to the total energy,

$$E_{pol}(\zeta_0) = \int_0^{\zeta_0} d\zeta e_{pol}(u^{in}(\zeta)) + \int_{\zeta_0}^{\infty} d\zeta e_{pol}(u^{out}(\zeta)). \quad (4.64)$$

The minimum of the total energy with respect to ζ_0 fixes the total energy corresponding to the stationary state as well as the corresponding μ' .

We have discussed the variational procedure for a quasi-one-dimensional harmonically trapped BEC, taking the example of the polar state. The same procedure is straightforwardly applied for the PM state as well.

4.2.4 Quasi-1-D harmonic confinement: Results

We assume that the geometric mean of the trapping frequencies in the transverse direction is, $\omega_{yz} = 2\pi \times 1261 \text{ Hz}$, which is much greater than the trapping frequency along the direction of elongation, $\omega_x = 2\pi \times 50 \text{ Hz}$. Corresponding interaction parameters are, $\lambda_0^{1D} = 46.157075 \times 10^{-3}$ and $\lambda_1' = 0.0161$. The energy estimation from the VM, in this

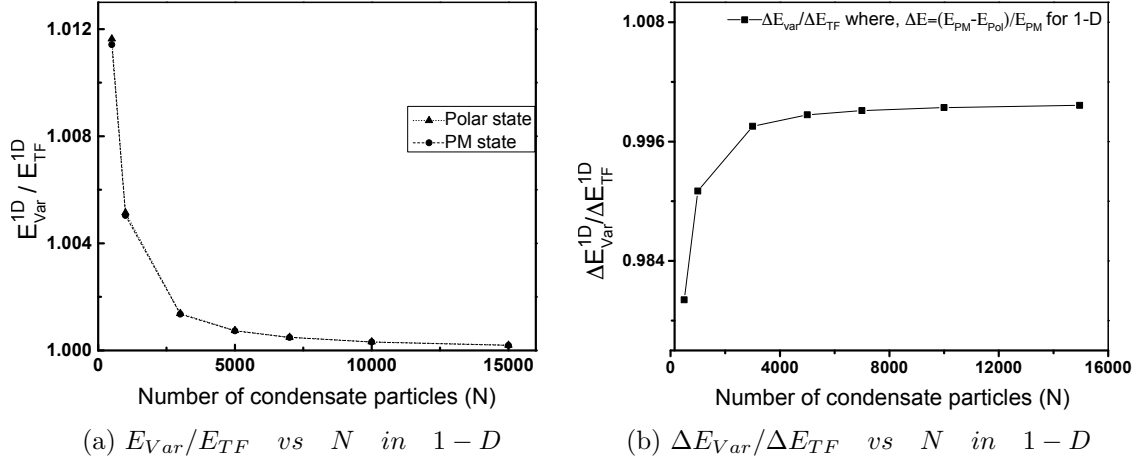


Figure 4.5: (a) Ratio of total energy estimated by VM and T-F approximation varies with the total number of condensate particles. The energy estimated by the VM is greater than the energy estimated by the T-F approximation. (b) The ratio of energy difference $((E_{PM}^{1D} - E_{pol}^{1D})/E_{PM}^{1D})$ between the PM and polar/APM/AF states in VM and T-F is plotted with the number of condensate particles. The inclusion of the kinetic energy and consideration of the full profile of the condensate does not change the relative energy difference that much for the 1-D harmonic confinement, given the trapping frequencies we have chosen.

case, also varies with the number of condensate particles in a similar fashion as in the 3-D isotropic trapping, where the VM has a more pronounced effect for smaller condensates. But in comparison with the 3-D case (Fig.4.4(a)), for this choice of trapping frequencies, the energy estimated by the VM does not deviate that significantly (Fig.4.5(a)) from the T-F approximated energy for both the stationary states. As a result, the energy difference between the stationary states (which is $\simeq 1\%$ in T-F limit for 1-D condensate) almost remains the same even for the smaller condensates after considering the full profile of the condensate and including the kinetic energy term. Note that, for different choices of trapping frequencies, a more noticeable energy difference could be seen.

4.2.5 Comparison of the variational method with numerically obtained condensate profile

Till now, we have seen that for the anti-ferromagnetic type of spin-interaction, the variational method indicates that the APM-like degenerate states (polar/ AF/ APM) are favored to be the ground state in the absence of the magnetic field. But in the variational method, we made a reasonable assumption to model the tail part of the condensate (the number density at the low-density region) with the first few lowest-energy states under

harmonic oscillator potential. It is only natural to ask about the validity of this assumption. So, we start with the GP equation for the polar state and numerically simulate the condensate profile for this state and compare it with the analytical profile to check the accuracy of the variational method.

For condensates in 3-D isotropic harmonic trapping, we substitute the number density with another function, $u(\eta) \rightarrow |\phi(\eta)|^2/\eta^2$. This would allow us to tackle the Laplacian term efficiently [140]. Here, we use the imaginary-time split-step Fourier method to simulate the ground state condensate profile.

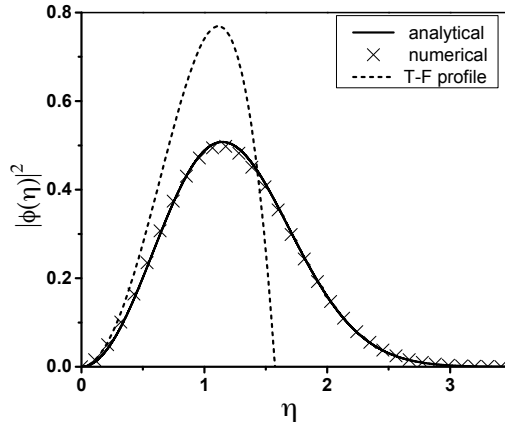
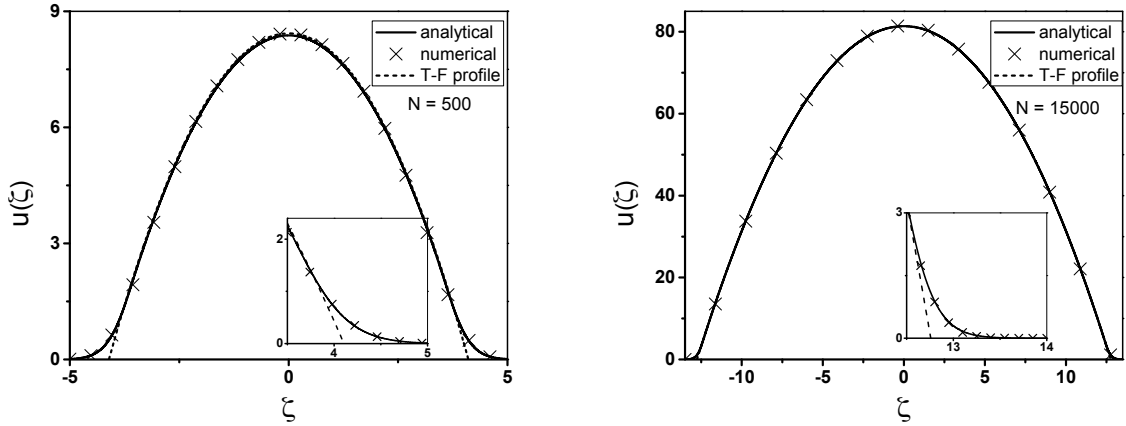


Figure 4.6: The condensate profile, for 3-D isotropic harmonic confinement, represented in terms of $|\phi(\eta)|^2$ with the radial distance η from the trap center for $N=500$, where $|\phi(\eta)|^2$ is related to the number density of the polar state as, $|\phi(\eta)|^2 = \eta^2 \times u(\eta)$. The VM estimated analytical profile matches quite well with the numerically simulated condensate profile while the T-F approximated profile shown in the dashed line deviates significantly from the simulated profile.

Note that, we have previously discussed that for small condensates with 500 particles, the variational method predicted $\eta_0 \simeq 0$. The analytical number density profile obtained from the VM, in this case, is $u = (\mu' + \eta^2/2)\exp(-\eta^2/\mu')$ corresponding to, $\mu' = 0.93$. In Fig.4.6 the 3-D condensate profile is represented in terms of $|\phi(\eta)|^2$ where, the VM estimated analytical profile is $|\phi^{Anal.}(\eta)|^2 = \eta^2(\mu' + \eta^2/2)\exp(-\eta^2/\mu')$. This analytical profile predicted by the variational method aptly represents the numerically simulated profile with reasonable accuracy. In contrast, the T-F profile, $|\phi^{T-F}(\eta)|^2 = \eta^2(\mu'^{T-F} - \eta^2/2)$ with the T-F approximated chemical potential, $\mu'^{T-F} = 1.241$, fails as expected. This emphasizes the need to go beyond the T-F approximation and use the variational method for much more accurate analytical estimation, especially for the 3-D condensate, where numerical simulation is, in general, computationally expensive.



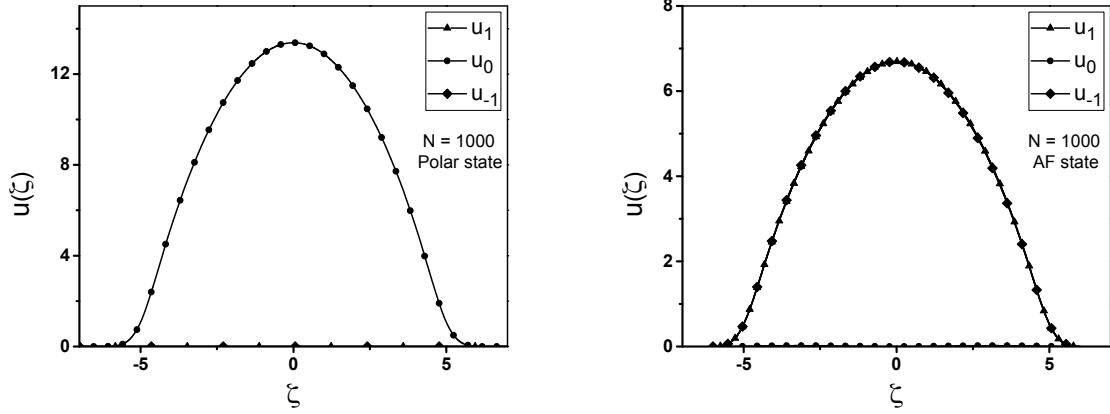
(a) number density $u(\zeta)$ with distance ζ for $N=500$

(b) number density $u(\zeta)$ with distance ζ for $N=15000$

Figure 4.7: Numerically obtained number density profile is compared with the analytical profiles. (a) For small condensate with particle number as low as $N=500$, the VM estimated analytical profile with $\mu' \simeq 8.378$ and the matching point at $(\zeta_0 \simeq) \pm 3.48$ agrees quite well with the numerically obtained profile. In the high-density region, the T-F profile (dashed line) matches the numerical profile but it deviates significantly for $|\zeta| > |\zeta_0|$ (see the inset plot). (b) For the large condensate ($N=15000$) we find $\mu' \simeq 81.372$ and $\zeta_0 \simeq 12.368$. The T-F approximation is good for large condensates. The VM verifies that the matching point is not very far from the T-F radius. Near $\zeta_0 \simeq 12.368$ significant difference between numerically obtained density and T-F density can be seen in the inset, while the VM profile matches quite accurately with the numerical density.

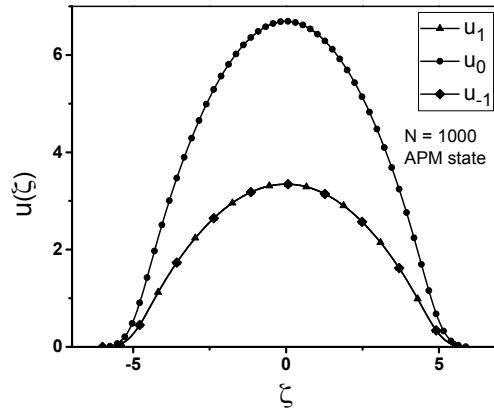
For the quasi-1-D harmonic trapping, the T-F approximated and the VM number density of the polar state are compared with the numerically obtained density profile for both small (Fig.4.7(a)) and large (Fig.4.7(b)) condensates. We find that the numerically obtained profile is in excellent agreement with the analytical profile in both cases. In this case also, the VM aptly describes the low-density region of the condensate profile (see the insets of Fig.4.7)

Note that the matching point (η_0) depends on $\lambda_0 N$. The parameter λ_0 can be modulated via Feshbach resonance (via changing c_0) or by changing the trapping frequency (hence the oscillator length), both of which are experimentally achievable. Thus, in the case of 3-D confinement, if the parameter λ_0 is halved, the matching point (η_0) is found to be close to zero or almost zero ($\eta_0 \simeq 0$) even for larger condensate with $N=1000$. This shows that even for larger condensates, the VM would find its significance in providing a fairly accurate condensate profile. The VM also produces a fair idea about the safe applicability of the T-F approximation.



(a) initial condition: u_1 and u_{-1} are negligibly small, only u_0 is occupied.

(b) initial condition: u_0 is negligibly small, other two sub-components are equally occupied.



(c) initial condition: all the sub-components occupied with zero magnetization.

Figure 4.8: Numerically obtained sub-component number densities of the condensate with an anti-ferromagnetic type of spin interaction in an effective 1-D trap, where the initial wave function is Gaussian where for (a) only u_0 , (b) u_1 and u_{-1} and (c) all the sub-components are populated. After sufficient imaginary time evolution, it confirms that all three degenerate states (i.e., (a) polar, (b) AF and (c) APM) are equally likely to become the ground states in this parameter regime.

We have seen that not only the polar state but also the APM and the AF states are equally likely to be the ground state. We numerically simulate the spin-1 Gross-Pitaevskii equation in the absence of the magnetic field with zero magnetization via imaginary time propagation to get to the ground state for $N=1000$ following the approach given in [141]. We use the Gaussian wave function as the initial condition. If we start with an initial condition, where u_0 is populated only, while the other two sub-components are negligibly populated, the solution after sufficient steps converges to the polar state (Fig.4.8(a)). Similarly, if we initialize $\sqrt{u_1}$ and $\sqrt{u_{-1}}$ with the Gaussian wave function along with $\sqrt{u_0}$ being negligibly populated, the solution converges to the AF state (Fig.4.8(b)) after

a sufficient time propagation. Whereas, if all the sub-components are initialized with the Gaussian wave function, we find APM state as the ground state (Fig.4.8(c)). Note that, this is characteristic of degenerate solutions, whereas, in [141, 142] only AF state is reported to be the ground state at zero magnetic field and zero magnetization for anti-ferromagnetic condensate.

4.2.6 Energy Density of the ground state

In the previous chapter, we saw that a comparison of the T-F approximated energy densities led to a lot of domain formation possibilities. In this chapter, we have discussed the need to go beyond the T-F approximation and the viability of the VM in providing a more accurate picture. In cases where the T-F approximation is not at all accurate, or when we need a more accurate energy density expression to compare the energy densities locally, it is only natural to ask if the VM can provide a good enough estimation of the energy density expression. To compare, the energy density of the polar state obtained from the VM, the T-F approximation, and the numerical simulation are plotted against the radial distance from the trap center for the 1-D harmonic trapping in Fig.4.9. We have shown only the positive half, it is symmetric in the negative half.

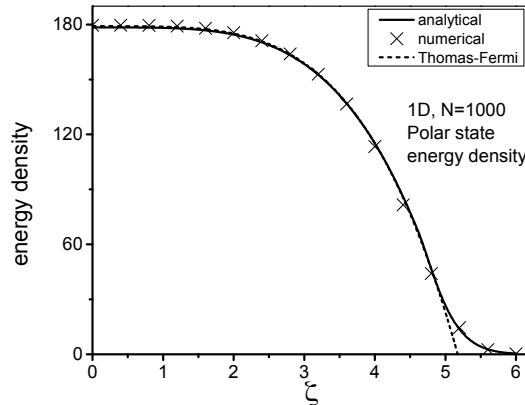


Figure 4.9: The energy density for polar state, for $N=1000$ is plotted against the distance (ζ), where $\zeta = 0$ is the 1-D trap center. Here the energy density profile obtained from the T-F approximation (dashed line) and the VM (solid line) is compared with the numerically obtained profile. Near the center of the trap, both the T-F and VM profile is quite good in comparison to the numerical profile. Near the T-F radius, the T-F approximated energy density deviates from the numerical one, while the VM estimation is very accurate in this low-density regime.

We observe that the VM and the T-F energy density profiles match quite well with the

numerical profile near the trap center, however, the marked difference can be seen near the T-F radius where the VM profile agrees with the numerical one with great accuracy. Thus, the smooth analytical energy density profile would find its importance in predicting the phase separation or domain formation phenomena wherever a detailed energy density comparison is required.

4.3 Discussion

In this chapter, we have introduced a multi-modal variational method that estimates the number density profile of a harmonically trapped spin-1 condensate with much more accuracy compared to the most widely used analytical method which is the T-F approximation. To showcase the importance of the method, we choose a simple possible setting, which is the absence of the magnetic field. We started with the T-F approximated results, which predict that, for anti-ferromagnetic spin interaction, the three degenerate states, namely the polar, anti-phase-matched, and anti-ferromagnetic states are equally likely to be the ground state. Quantitatively, the closely competing stationary states namely the PM state or the ferromagnetic states have a very small energy difference with the T-F approximated ground state. This quantity is independent of the number of particles present in the condensate. This small relative energy difference is of the order of the kinetic energy contribution. So, even for large condensates, the T-F approximated results, which are obtained disregarding the kinetic energy contribution, are inconclusive. Such a situation requires a closer inspection. We introduce the variational method that incorporates the kinetic energy contribution and produces more refined ground state estimations.

The variational method not only produces a smooth number- and energy density profile of the condensate in large particle number limit where the T-F approximation is generally applicable but also it works excellent in comparison to the numerical simulation even for as low as a few hundred particles, where the T-F approximated profile is far from accurate. The VM estimates the condensate profile for the 3-D trapping geometry with great accuracy, whereas numerical simulation for the 3-D case is, in general, computationally expensive. In the context of the ground state, the VM still indicates that the polar or the other two degenerate states are favored. In contrast to the T-F approximated results, the relative energy difference according to the VM depends on the number of particles in the

condensate. For condensates with low particle numbers, this energy difference becomes almost one-fourth of that estimated by the T-F approximation.

Note that, for ^{87}Rb , the spin-spin interaction is of ferromagnetic type and the $|c_1|/c_0$ ratio for this case is much lower than that of ^{23}Na . The relative energy difference between the T-F approximated ground state (PM or the ferromagnetic states) and the other three degenerate states would be even lower than the relative energy difference of the ^{23}Na system (which is 0.5% under T-F approximation). The variational method developed in this chapter can be easily applied to get an accurate picture of the ^{87}Rb system as well.

Chapter 5

Multi-component stationary states in the presence of the magnetic field

In the last chapter, we have introduced a variational method and focused on a case study, which is finding out the ground state of the harmonically trapped spin-1 condensate in the absence of the magnetic field. The T-F approximation was inconclusive due to the competing energies of the ground state candidates and there was a requirement to go beyond the T-F approximation. The variational method in the absence of the magnetic field not only provided important corrections to the T-F approximated results but also demonstrated its essential applicability for condensates with fewer particles where the T-F approximation cannot be applied.

In this chapter, we will look at the multi-component stationary states, which become the ground states both for the anti-ferromagnetic and ferromagnetic types of spin interaction, in the presence of the magnetic field. We will see, even when the number of particles present in the condensate is large, the T-F approximation could produce wrong physical interpretation of domain structure in the ground state. We will demonstrate that the generalized multi-modal variational method in the presence of the magnetic field is essential in giving a proper analytical description of multi-component states.

Accurately known density profiles of the multi-component ground state are crucial in dealing with a lot of interesting phenomena like complex soliton structures [71–74], domain formation [121] that can occur in spinor BEC. There have been a lot of studies on

multi-component ground states [54, 115, 129, 130]. But, most of those analytical studies are based on Thomas-Fermi (T-F) approximation and single-mode approximation (SMA) for the sake of simplicity. In the previous chapter, we have shown a variational method that is multi-modal in nature. Note that, in the absence of the magnetic field, the sub-components of the multi-component states follow a single spatial mode. In this chapter, we will see that in the presence of the magnetic field, the multi-component states, that are the essence of spinor-BEC do not, in general, follow a single spatial mode. In this case, neither SMA nor the T-F approximation can provide an accurate description. The T-F approximation even leads to a wrong physical interpretation of domain structure in the ground state. No matter how large the condensate is (in the so-called "T-F limit"), for the multi-component states, if at least one of the sub-components tends to vanish at a smaller distance away from the trap center than the other components, then the T-F approximation will indicate a domain structure in the ground state. Whereas, numerical simulation does not indicate any domain structure in the ground state. Thus, in general, the T-F approximation cannot be trusted for the ground state prediction of a trapped spin-1 BEC in the presence of the magnetic field, no matter how large the condensate may be. On top of that, the SMA also becomes inaccurate in estimating the sub-component density distributions. The variational method, on the other hand, is reliable for the ground state prediction as well as for getting the condensate profiles in such situations.

The multi-modal variational method provides accurate density profiles which can be used for the estimation of the total energy of the multi-component states. The total energy of different stationary states can be compared to get to the phase transition boundaries over (q, p) parameter space. We will estimate the phase transition boundary between the PM (multi-component state) and the polar state (that happens for $c_1 < 0$) for a 3-D isotropic harmonic confinement and draw a detailed comparison of the trapped situation with that of the homogeneous case (in the absence of trapping as shown in Fig.2.1(c)).

5.1 GP equation in the non-dimensional form: Recap

For a particular stationary state the sub-component phase equations

$$\hbar\dot{\theta}_0 = \frac{1}{\sqrt{n_0(\mathbf{r})}} \left(-\frac{\hbar^2 \nabla^2}{2M} + U(\mathbf{r}) + c_0 n - \mu \right) \sqrt{n_0(\mathbf{r})} + c_1 (n_1 + n_{-1} + 2\sqrt{n_{-1}n_1} \cos \theta_r), \quad (5.1)$$

$$\begin{aligned} \hbar\dot{\theta}_{\pm 1} = \frac{1}{\sqrt{n_{\pm 1}(\mathbf{r})}} \left(-\frac{\hbar^2 \nabla^2}{2M} + U(\mathbf{r}) + c_0 n - \mu \right) \sqrt{n_{\pm 1}(\mathbf{r})} \pm c_1 (n_1 - n_{-1}) + q \mp p \\ + c_1 n_0 \left(1 + \sqrt{\frac{n_{\mp 1}(\mathbf{r})}{n_{\pm 1}(\mathbf{r})}} \cos \theta_r \right), \end{aligned} \quad (5.2)$$

can be solved that yields the sub-component number densities and hence the total energy corresponding to the stationary state.

Here, we will consider a quasi-one-dimensional geometry. The condensate is assumed to be trapped in harmonic confinement with elongation along the x-axis. The trapping frequency along the direction of elongation is much less than the geometric mean of the trapping frequency along the other two directions i.e., $\omega_x \ll \omega_{yz}$, where $\omega_{yz} = \sqrt{\omega_y \omega_z}$. We will rewrite the number density and the interaction parameters in a slightly different scaling from that we used in Eq.4.54-4.55,

$$c_0 = 2\pi l_{yz}^2 l_x \lambda_0 \hbar \omega_x, \quad c_1 = 2\pi l_{yz}^2 l_x \lambda_1 \hbar \omega_x, \quad (5.3)$$

$$u_m = 2\pi l_{yz}^2 l_x n_m, \quad r = l_x \zeta. \quad (5.4)$$

Imposing the stationarity condition, for the quasi-one-dimensional harmonic trapping, the phase equations can now be written by using Eq.5.3-5.4,

$$\left\{ -\frac{1}{2} \frac{d^2}{d\zeta^2} + \frac{1}{2} \zeta^2 + \lambda_0 u - \mu' + \lambda_1 (u_1 + u_{-1} + 2\sqrt{u_{-1}u_1} \cos \theta_r) \right\} \sqrt{u_0} = 0, \quad (5.5)$$

$$\left\{ -\frac{1}{2} \frac{d^2}{d\zeta^2} + \frac{1}{2} \zeta^2 + \lambda_0 u - \mu' \pm \lambda_1 (u_1 - u_{-1}) \mp p' + q' \right\} \sqrt{u_{\pm 1}} + \lambda_1 u_0 (\sqrt{u_{\pm 1}} + \sqrt{u_{\mp 1}} \cos \theta_r) = 0, \quad (5.6)$$

where p' , q' , and μ' correspond to the dimensionless forms of the linear and quadratic Zeeman terms and the chemical potential respectively. The scaling is done by dividing the parameters with the factor $\hbar \omega_x$. The total density u is obviously the sum of the sub-component densities, i.e., $u = u_1 + u_0 + u_{-1}$.

To solve these equations one can use that T-F approximation, and we have discussed all the details of it in Chapter 3. We have summarized the T-F approximated number densities and the energy densities in this scaling, for different stationary states of our present interest, in Table 5.1.

States	Variation of density	Energy density	Restriction
(1,0,0) <i>F1</i>	$(\lambda_0 + \lambda_1)u(\zeta) = \mu' + p' - q' - \zeta^2/2$	$\frac{[\zeta^2/2 - p' + q'][\mu' + p' - q' - \zeta^2/2]}{(\lambda_0 + \lambda_1)} + \frac{[\mu' + p' - q' - \zeta^2/2]^2}{2(\lambda_0 + \lambda_1)}$	<i>none</i>
(0,1,0) <i>P</i>	$\lambda_0 u(\zeta) = \mu' - \zeta^2/2$	$\frac{\zeta^2/2[\mu' - \zeta^2/2]}{\lambda_0} + \frac{[\mu' - \zeta^2/2]^2}{2\lambda_0}$	<i>none</i>
(0,0,1) <i>F2</i>	$(\lambda_0 + \lambda_1)u(\zeta) = \mu' - p' - q' - \zeta^2/2$	$\frac{[\zeta^2/2 + p' + q'][\mu' - p' - q' - \zeta^2/2]}{(\lambda_0 + \lambda_1)} + \frac{[\mu' - p' - q' - \zeta^2/2]^2}{2(\lambda_0 + \lambda_1)}$	<i>none</i>
(1,0,1) <i>AF</i>	$\lambda_0 u(\zeta) = \mu' - q' - \zeta^2/2$ and $(u_1 - u_{-1}) \equiv F_z = \frac{p'}{\lambda_1}$	$\frac{[\zeta^2/2 + q'][\mu' - q' - \zeta^2/2]}{\lambda_0} + \frac{[\mu' - q' - \zeta^2/2]^2}{2\lambda_0} - \frac{p'^2}{2\lambda_1}$	<i>none</i>
(1,1,1) <i>(A)PM</i>	$(\lambda_0 + \lambda_1)u(\zeta) = k_1 - \zeta^2/2$ where, $k_1 = \mu' + \frac{(p'^2 - q'^2)}{2q'}$	$\frac{\zeta^2/2[k_1 - \zeta^2/2]}{\lambda_0 + \lambda_1} + \frac{\lambda_1}{2} \left[\frac{k_1 - \zeta^2/2}{\lambda_0 + \lambda_1} - \frac{p'^2 - q'^2}{2q'\lambda_1} \right]^2 + \frac{\lambda_0}{2} \left[\frac{k_1 - \zeta^2/2}{\lambda_0 + \lambda_1} \right]^2$	<i>PM</i> ($ p' < q' $) <i>APM</i> ($ p' > q' $)

Table 5.1: The density and the energy density expressions corresponding to different stationary states at $\lambda_1 \neq 0$ obtained via T-F approximation are shown here [121, 122]. All the parameters in this table are in dimensionless form. One can use Eq.5.3-5.4 to convert expressions into dimensional forms. The energy expressions and the density expressions for PM and APM states are identical. However, PM and APM states are restricted in space where the APM state exists if the absolute value of the linear Zeeman term is higher than that of the quadratic Zeeman term and PM state exists otherwise.

5.2 Multi-component stationary states:

In what follows, we will do a qualitative as well as quantitative analysis. For that, we have considered a quasi-one-dimensional cigar-shaped harmonic confinement. The trapping frequency along the elongated direction is $\omega_x = 2\pi \times 50 \text{ Hz}$ and the geometric mean of the trapping frequencies along the transverse direction is $\omega_{yz} = 2\pi \times 1261 \text{ Hz}$. In the last chapter, we saw that for 1-D trapping geometry with the same trapping frequency, the T-F approximation gives reasonably good results in estimating the number density

for the single-component stationary states with $N \geq 500$, in the absence of the magnetic field (see Fig.4.7(a)). So, it is logical to believe that the T-F approximation might lead to fairly accurate results for multi-component stationary states in the presence of a small magnetic field if $N \geq 500$.

For quantitative analysis, we fix the number of condensate particles at $N = 5000$, for which one can expect that the T-F approximation would produce even better results. The multi-component states that become the ground state are our focus in this chapter. We will discuss the details of the PM state that appears as a ground state for a range of linear and quadratic Zeeman terms (p' and q' values), in condensates with the ferromagnetic spin-spin interaction e.g., ^{87}Rb . We will also focus on the anti-ferromagnetic state which is the ground state for ^{23}Na that possess the anti-ferromagnetic type of spin interaction [83]. For quantitative analysis, we have chosen specific values of p' and q' and also taken the quasi-one-dimensional confinement for convenience in numerical simulation. However, the analytic formalism developed and validated is general and can be extended to higher dimensional cases where numerical analysis could be problematic. Similarly, the results do not depend on the specific choices of p' and q' as well. In the following, we will start with the T-F analysis for these two cases, to exemplify the problem with the T-F approximation when applied to spin-1 condensate. This will also help us to draw a detailed comparison with the beyond T-F approximated results later.

5.2.1 PM state: T-F study

For ^{87}Rb condensate that possesses the ferromagnetic type of spin interaction, the oscillator length along the direction of elongation is $l_x = 1.53 \mu\text{m}$, while along the transverse direction $l_{yz} = 0.30 \mu\text{m}$, corresponding to the above-specified trap geometry. The spin-independent and the spin-dependent interaction parameters assume the numerical values, $\lambda_0 = 17.66 \times 10^{-2}$ and $\lambda_1 = -6.22 \times 10^{-4}$.

In this section, we will compare the T-F approximated results with the numerical profile to discuss the issue with the T-F approximation when applied to the multi-component states. As a case study, we fix the linear and quadratic Zeeman terms at $p' = 0.01$ and $q' = 0.3$. The stationary state that is energetically favorable to be the ground state at these parameter values is the PM state. The conclusions will remain valid for a range of

p' and q' values for which the PM state is favorable as the ground state.

In Chapter 3, we have shown the derivation of the PM sub-component densities for arbitrary p and q values under the T-F approximation. Given the scaling we have used in Eq.5.3-5.4, the T-F approximated sub-component number densities of the PM state are,

$$u_1^{TF} = \frac{(p' + q')^2}{4q'^2} \left[\frac{\mu' + \frac{(p'^2 - q'^2)}{2q'} - \frac{1}{2}\zeta^2}{\lambda_0 + \lambda_1} + \frac{q'^2 - p'^2}{2\lambda_1 q'} \right], \quad (5.7)$$

$$u_{-1}^{TF} = \frac{(p' - q')^2}{4q'^2} \left[\frac{\mu' + \frac{(p'^2 - q'^2)}{2q'} - \frac{1}{2}\zeta^2}{\lambda_0 + \lambda_1} + \frac{q'^2 - p'^2}{2\lambda_1 q'} \right], \quad (5.8)$$

$$u_0^{TF} = \frac{(q'^2 - p'^2)}{2q'^2} \left[\frac{\mu' + \frac{(p'^2 - q'^2)}{2q'} - \frac{1}{2}\zeta^2}{\lambda_0 + \lambda_1} - \frac{q'^2 + p'^2}{2\lambda_1 q'} \right]. \quad (5.9)$$

We compare these expressions that we obtained in the T-F approximation with the numerically simulated profiles (we use the imaginary time propagation in the split-step Fourier method [141]), where the profiles as estimated by the T-F approximation are used as the initial wave function.

The T-F approximated sub-component densities u_1 and u_{-1} agree well with the numerical ones except near the T-F radius of these components (see Fig.5.1(a)). Whereas, the T-F profile of the u_0 component also agrees with the numerical one in the high-density region of the trap but starts to deviate when the other components u_1 and u_{-1} vanish, which for this parameter values is at around $\zeta_{\pm 1}^{TF} = \pm 10.3$. Note that, $\zeta_{\pm 1}^{TF}$ is the T-F radius of the $u_{\pm 1}$ components. Naturally, one might expect that, beyond the point, $\zeta_{\pm 1}^{TF}$, the summation of the T-F approximated sub-component number densities (i.e., $u_{tot} = u_1 + u_0 + u_{-1}$) will not agree with the numerical profile as there is a significant mismatch in the u_0 component.

Note that, in Chapter 3, we have discussed in detail that the necessary condition for the validity of the PM state in the T-F approximation is that all the sub-components are populated. So, the PM state is only valid for $|\zeta| < |\zeta_{\pm 1}^{TF}|$ i.e., as long as all the sub-components are populated and beyond the T-F radius of $u_{\pm 1}$, the PM state ceases

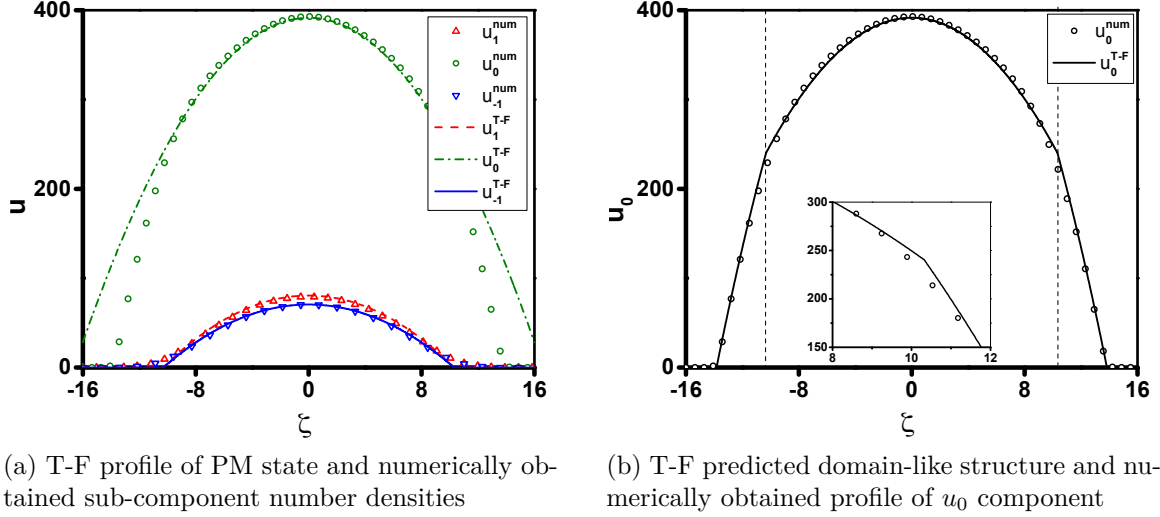


Figure 5.1: (a): The T-F approximated sub-component number densities (u_1 , u_0 and u_{-1} components shown in red dash, green dash-dot, and blue solid lines respectively) for the PM state are compared with the numerical densities (markers) for the parameter value $p' = 0.01$ and $q' = 0.3$. The T-F approximated u_0 expression corresponding to the PM state (shown in the green dash-dot line) starts to deviate from that of the numerical simulation beyond $|\zeta| > 10.3$, which is the T-F radius of the $u_{\pm 1}$ component. (b): The T-F prediction of the domain-like situation is plotted where, the u_0 component (solid line) follows the T-F expression of the PM state when all the sub-components are populated ($|\zeta| < 10.3$ for this case) near the center of the trap, followed by a polar state-like behavior. Note that a discontinuity appears in the u_0 (inset) for this domain-like construct, while the numerical result is smooth (bubble markers).

to exist. In this region, only the u_0 component is present, which indicates that it is the polar state (see Table 5.1) that occupies the low-density region of the trap. So, the T-F approximation indicates there is a domain structure with the PM state near the center of the harmonic trap, and the polar state staying in the low-density region.

The sub-component number densities for such a domain-like construct can be given as,

$$u_1^{TF} = \frac{(p' + q')^2}{4q'^2} \left[\frac{\mu' + \frac{(p'^2 - q'^2)}{2q'} - \frac{1}{2}\zeta^2}{\lambda_0 + \lambda_1} + \frac{q'^2 - p'^2}{2\lambda_1 q'} \right], \quad (5.10)$$

$$u_{-1}^{TF} = \frac{(p' - q')^2}{4q'^2} \left[\frac{\mu' + \frac{(p'^2 - q'^2)}{2q'} - \frac{1}{2}\zeta^2}{\lambda_0 + \lambda_1} + \frac{q'^2 - p'^2}{2\lambda_1 q'} \right], \quad (5.11)$$

$$u_0^{TF} = \begin{cases} \frac{(q'^2 - p'^2)}{2q'^2} \left[\frac{\mu' + \frac{(p'^2 - q'^2)}{2q'} - \frac{1}{2}\zeta^2}{\lambda_0 + \lambda_1} - \frac{q'^2 + p'^2}{2\lambda_1 q'} \right], & \text{if } |\zeta| \leq \zeta_{\pm 1}^{TF} \\ \frac{\mu'_{polar} - \frac{1}{2}\zeta^2}{\lambda_0}, & \text{otherwise,} \end{cases} \quad (5.12)$$

where, $\zeta_{\pm 1}^{TF}$ is the Thomas-Fermi radius of the $u_{\pm 1}$ component for this 1-D geometry. Obviously, if this domain-like construct has to be stable we have to impose the condition that the chemical potential μ' for the PM and the polar state (μ'_{polar}) has to be the same. It might seem that (in Fig.5.1(b)), this domain-like explanation works as we compare the sub-component density with the numerical u_0 . But upon closer inspection, one can check that there is a discontinuity at $|\zeta| = \zeta_{\pm 1}^{TF}$. The slope of analytical u_0 also changes drastically around this point resulting in a lot of kinetic energy cost.

The discontinuity in the u_0 component and hence the limitations of the domain-like construct as indicated by the T-F approximation can be further strengthened if we compare numerical simulation and the T-F prediction for a different spin interaction. We increase the spin interaction five times of that of the natural value, $c_1 \rightarrow 5c_1^{Rb}$ while keeping all other parameter values the same. From an experimental point of view, this is amenable via Feshbach resonance [143].

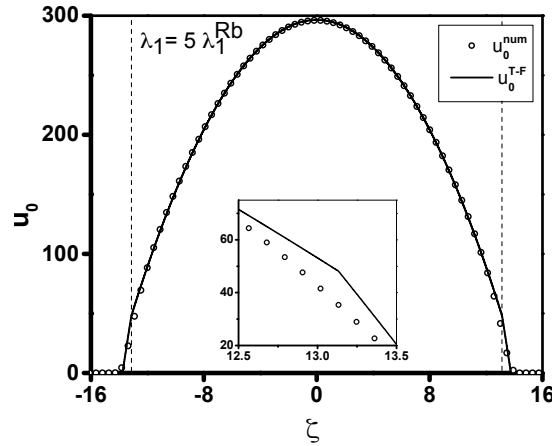


Figure 5.2: The T-F approximated sub-component number density u_0 of the domain-like structure between the PM state and polar state, for the same the parameter values $p' = 0.01$ and $q' = 0.3$ and λ_0 with a spin interaction coefficient c_1 (or λ_1 in this context), which is 5 times of that of the normal value of ^{87}Rb . Increasing the spin interaction shows a similar discontinuity present in u_0 at $|\zeta_{\pm 1}^{TF}| = 13.13$ (dashed lines are placed) for the PM-polar domains (see inset).

As the λ_1 becomes five times the previous value, the domain-like structure predicted

by the T-F approximation shows similar discontinuity (see inset of Fig.5.2) for the sub-component u_0 at $|\zeta_{\pm 1}^{TF}| = 13.13$. The total density for this domain-like structure will also have that same discontinuity.

To explain this, one has to remember that in the T-F approximation, the $u_{\pm 1}$ components sharply go to zero at $|\zeta| = \zeta_{\pm 1}^{TF}$. But in reality, that cannot be the case. We need to include the kinetic energy term in the analysis. As a result, near this point, the Laplacian terms in Eq.5.6 cannot be neglected. However, one can ignore the Laplacian term in Eq.5.5, as the u_0 component is still in the high-density region near this point. Note that, the GP equations are coupled, as a result, one has to solve the Eq.5.5-5.6 by keeping the Laplacian terms corresponding to $u_{\pm 1}$ components. This shows that the T-F approximation is bound to produce an inaccurate description of multi-component stationary states even in the so-called "T-F regime", no matter how large the condensate may be. This warrants an accurate analytical description of the multi-component states appearing for the spin-1 BEC.

5.2.2 PM state: The variational method

In Chapter 4, we proposed a multi-modal variational method that incorporates the kinetic energy contribution and produces the sub-component number density profiles of a stationary state with great accuracy. The variational method (VM) was developed for a spin-1 BEC in the absence of a magnetic field which works with great accuracy even for condensates with a few hundred particles, where the T-F approximation was shown to be no longer valid. The PM state was also analyzed using the multi-modal VM, but for $p = 0$ and $q = 0$, the sub-components of the PM state follow the same spatial mode, which reduces the complexity significantly. In the presence of the magnetic field, we will see that the sub-components no longer follow a single-spatial mode. We extend the same procedure here in the presence of a magnetic field. When the sub-components do not follow the same spatial variation, the situation is much more complex but the extended multi-modal VM tackles it case with ease.

For the variational method to work, we need to estimate the sub-component densities in the high-density region from the phase equations i.e., Eq.5.5-5.6 by neglecting the kinetic energy contribution. This is due to the fact that the density is high in this region,

and so does the interaction terms, and with respect to it, the kinetic energy term can be neglected. This is followed by an assumption of the Gaussian tail in the low-density region. So according to this assumption, the sub-component densities can be written as,

$$u_{\pm 1,0}^{in} = g_{\pm 1,0}(\mu', \zeta), \quad \text{for } |\zeta| \leq \zeta_{\pm 1,0}^{mat} \quad (5.13)$$

$$u_{\pm 1,0}^{out} = (a_{\pm 1,0} + c_{\pm 1,0}|\zeta| + d_{\pm 1,0}\zeta^2)exp\left(-\frac{\zeta^2}{b_{\pm 1,0}}\right) \quad \text{for } |\zeta| \geq \zeta_{\pm 1,0}^{mat}; \quad (5.14)$$

where $g_{\pm 1,0}(\mu', \zeta)$ is the functional form of the sub-component density of $u_{\pm 1,0}$ near the center of the trap. In the low-density region, we assume the number density (or the wave function) taking into account the first few lowest harmonic oscillator states. Now we impose the condition that for each sub-component the low-density $\sqrt{u_{\pm 1,0}^{out}}$ and the high-density $\sqrt{u_{\pm 1,0}^{in}}$ expressions match at a point ζ^{mat} . Not only do they match but their first three derivatives also match. These four constraints provide the four unknowns a , b , c , and d for each sub-components in terms of the matching points and the parameter μ' . Note that, imposing the matching condition up to three derivatives also gives a smooth profile of the corresponding kinetic energy.

Following the procedure, once we determine all the coefficients in Eq.5.14, the sub-component density profile then will only depend on the parameter μ' and the matching points. By integrating the sub-component densities and adding them, one gets to the total number of condensate particles N , i.e.,

$$\sum_{m=-1}^1 \left[\int_0^{\zeta_m^{mat}} u_m^{in}(\mu', \zeta) d\zeta + \int_{\zeta_m^{mat}}^{\infty} u_m^{out}(\mu', \zeta, \zeta_m^{mat}) d\zeta \right] = N, \quad (5.15)$$

This equation can be used to determine μ' as a function of the matching points. Note that, one might expect that the right side should be $N/2$ as the integration is running in only one direction from the center of the trap, but it is N on the right side due to Eq.5.3-5.4 that we used to write the GP equation in non-dimensional form.

Thus the sub-component number densities and, hence, the total energy of a stationary state become the function of the matching points only. From the minimization of the total energy in the parameter space of the matching points, one can determine the matching points as well as the total energy.

For the specific case we are interested in, the PM state, all the sub-components are populated followed by the phase matching condition, i.e., the relative phase being $\theta_r = 0$. One can solve the phase stationary equations (Eq.5.5-5.6) by ignoring the kinetic part to get the sub-component densities in the high-density region. The sub-component densities can be written as,

$$u_m^{in} = k_m \left[\frac{\mu'_m - \zeta^2/2}{\lambda_0 + \lambda_1} \right], \quad (5.16)$$

where,

$$k_1 = \frac{(p' + q')^2}{4q'^2}, \quad k_0 = \frac{q'^2 - p'^2}{2q'^2}, \quad k_{-1} = \frac{(p' - q')^2}{4q'^2} \quad (5.17)$$

and,

$$\mu'_{\pm 1} = \mu'_{eff} + (\lambda_0 + \lambda_1) \frac{q'^2 - p'^2}{2\lambda_1 q'}, \quad (5.18a)$$

$$\mu'_0 = \mu'_{eff} - (\lambda_0 + \lambda_1) \frac{q'^2 + p'^2}{2\lambda_1 q'}, \quad (5.18b)$$

$$\mu'_{eff} = \mu' + \frac{p'^2 - q'^2}{2q'}. \quad (5.18c)$$

Applying the four matching conditions mentioned earlier, the unknown coefficients in the low-density expression for each sub-component can be obtained as,

$$a_m = \frac{1}{-8\mu'_m + 4\zeta_m^2} \left(\mu'_m \left(-56\mu'_m + 70\zeta_m^2 + 4\kappa_m \right) - 3\zeta_m^2 \left(14\zeta_m^2 + \kappa_m - 6\mu'_m \right) \right) \exp\left(\frac{12\zeta_m^2}{\kappa_m}\right), \quad (5.19a)$$

$$b_m = \frac{\kappa_m}{12}, \quad (5.19b)$$

$$c_m = \frac{48\zeta_m^3 \left(-12\mu'_m + 6\zeta_m^2 + \kappa_m \right)}{\kappa_m^2} \exp\left(\frac{12\zeta_m^2}{\kappa_m}\right), \quad (5.19c)$$

$$d_m = \frac{1}{2\zeta_m^2 \left(-2\mu'_m + \zeta_m^2 \right)} \left(-6(\mu'_m)^2 - \zeta_m^2 \left(\kappa_m + 13\zeta_m^2 - 6\mu'_m \right) + \mu'_m \left(14\zeta_m^2 + \kappa_m - 6\mu'_m \right) \right) \exp\left(\frac{12\zeta_m^2}{\kappa_m}\right), \quad (5.19d)$$

where, ζ_m is an abbreviation for the matching point ζ_m^{mat} , and

$$\kappa_m = 6\mu'_m - 9\zeta_m^2 + \sqrt{36\mu_m^2 - 12\mu_m\zeta_m^2 + 33\zeta_m^4}, \quad (5.20)$$

given the sub-component densities in the low-density region are represented as,

$$u_m^{out} = \frac{k_m}{\lambda_0 + \lambda_1} \left(a_m + c_m|\zeta| + d_m\zeta^2 \right) \exp\left(-\frac{\zeta^2}{b_m} \right). \quad (5.21)$$

Now, applying Eq.5.15 one can find the parameter μ' (see μ'_{eff} expression in Eq.5.18c) for different values of ζ_m . Thus, the total energy for the PM state becomes only a function of the matching points. Note that, as $\mu'_1 = \mu'_{-1}$ (see Eq.5.18a) the matching points are the same for these two components, i.e., $\zeta_1^{mat} = \zeta_{-1}^{mat}$.

Note that, the total density of the T-F approximation of the PM state is,

$$u_{tot}^{PM} = \frac{\mu' + \frac{(p^2 - q^2)}{2q} - \frac{1}{2}\zeta^2}{\lambda_0 + \lambda_1}, \quad (5.22)$$

which is analogous to Eq.3.39. This in principle should hold as long as all the sub-components are populated, which is a necessary condition for the validity of the PM state. As the number density cannot be negative, at $|\zeta| > |\zeta_{\pm 1}^{TF}|$ where the $u_{\pm 1}^{TF}$ goes to zero, the above expression is not valid. Also, the PM state does not exist beyond this point.

In Fig.5.3, we notice that the total number density obtained from the numerical simulation can be aptly described by the analytical expression Eq.5.22. The element of surprise is that even beyond $|\zeta_{\pm 1}^{TF}|$, where according to the T-F approximation the PM state ceases to exist, the numerical profile of total number density agrees with Eq.5.22.

We will use this observation coming from the numerical evidence of total density following Eq.5.22 to shift our focus to the total number density u_{tot} instead of the u_0 component while implementing the variational method. So, instead of using the high-density expression u_0^{in} we will use the total density expression,

$$u_{tot}^{in} = k_{tot} \left[\frac{\mu'_{eff} - \zeta^2/2}{\lambda_0 + \lambda_1} \right], \quad (5.23)$$

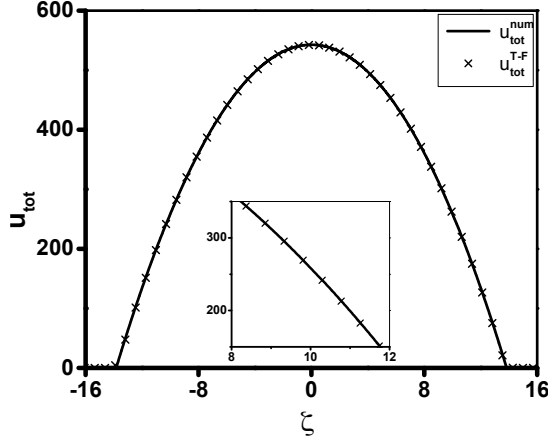
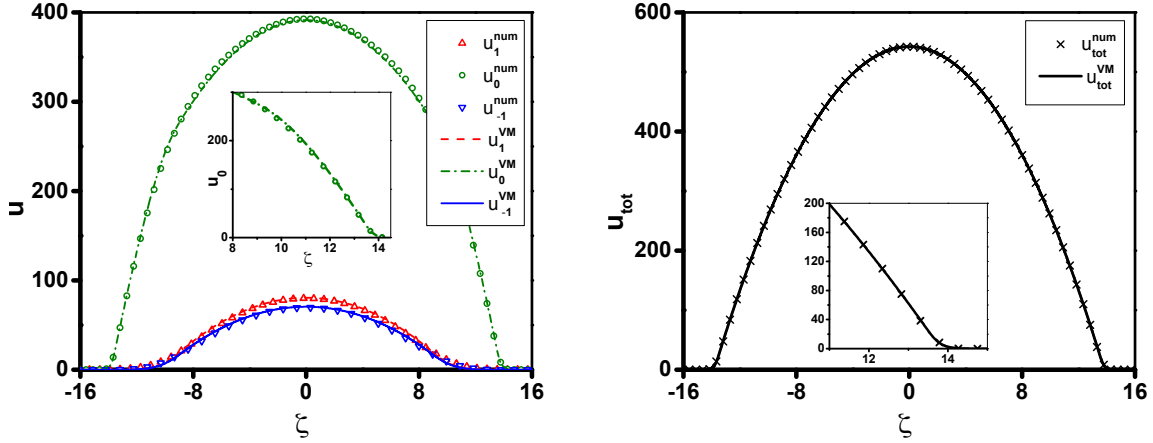


Figure 5.3: The total density obtained from numerical simulation matches quite well with the expression Eq.5.22, which is the T-F expression corresponding to the total density of the PM state. This expression of total number density is only valid as long as all the sub-components are populated. Beyond $|\zeta_{\pm 1}^{TF}|$, according to T-F approximation, Eq.5.22 cannot describe the total density of the PM state, because if it does, then it has to incorporate the negative density contribution from $u_{\pm 1}$ components. (inset) The same expression matches with the numerical total density even beyond the T-F radius $|\zeta_{\pm 1}^{TF}|$ which is roughly at $|\zeta| \simeq 10.3$.

written in the same fashion as Eq.5.16, where $k_{tot} = 1$. Now, one can use Eq.5.19a-5.19d which would also provide total density expression in the low-density region, written in the same fashion as Eq.5.21. The u_0 expression can be later found out by subtracting the sum of variational profiles of $u_{\pm 1}$ from the total number density profile, i.e., $u_0^{VM} = u_{tot}^{VM} - u_1^{VM} - u_{-1}^{VM}$. So, instead of the u_0 component, we will focus on total number density which will also provide a matching point ζ_{tot}^{mat} . Note that, for the PM state, the spatial mode for the u_1 and u_{-1} are equivalent, so the matching point for those two sub-components will be the same i.e., $\zeta_1^{mat} = \zeta_{-1}^{mat}$. Thus, the minimization of the total energy in the two-dimensional parameter space of ζ_1^{mat} and ζ_{tot}^{mat} will determine the energy itself, as well as approximate values of these parameters. Once the matching points are found, the analytical density expressions are also obtained.

Note that, for implementing the variational method, we need the estimate of the number density in the high-density region. In this context, the variational method cannot be implemented using the high-density T-F-like expression corresponding to the u_0 component, i.e., Eq.5.9. This is because the expressions given in Eq.5.7-5.8 runs to negative values beyond the T-F radius of the $u_{\pm 1}$ components. In this region, the u_0 expression (Eq.5.9), which is still in the high-density region, is an over-count that offsets the negative

contribution Eq.5.7-5.8 to conserve the number of particles. The numerically estimated total density matching the Eq.5.22 (which is the sum of Eq.5.7-5.9) further verifies this fact. So, it is essential to shift the focus to the total number density instead of the u_0 component (in fact, it would not work if one takes the T-F-like u_0 expression to implement the variational method).



(a) The VM approximated sub-component number densities and the numerical profile

(b) The VM approximated and numerically obtained total number density

Figure 5.4: (a): The sub-component number density of the PM state obtained from the variational method (u_1 , u_0 and u_{-1} components shown in red dash, green dash-dot, and blue solid lines respectively) and numerical simulation (markers) are plotted against the distance ζ from the center of the trap. The VM estimated analytical profile describes the numerical data quite well near the center of the trap as well as near the tail part of the condensate. The VM rules out any domain-like possibility and analytically estimates the u_0 component (shown in the dash-dot line) that is quite accurate even near the $\zeta_{\pm 1}^{TF}$ in comparison to the numerical (circles) profile (see inset). (b): The analytical profile of the total number density estimated by the VM matches the numerical result even in the low-density region, where it gives an analytic estimate of the condensate density which asymptotically goes to zero with the increase of the distance ζ .

For this specific choices of p' and q' , we find, $\zeta_{\pm 1}^{\text{mat}} = 8.5$ and $\zeta_{\text{tot}}^{\text{mat}} = 13.43$ from the minimization of the total energy. These matching points also determine the parameter $\mu' = 95.6$ from the number conservation equation, Eq.5.15. Thus, the sub-component number densities can be written in an analytical form as,

$$u_1^{\text{var}} = \begin{cases} 1.5173(53.1007 - 0.5\zeta^2), & \text{if } |\zeta| \leq 8.5 \\ 1.5173(114177.278 - 31226.158|\zeta| + 2184.067\zeta^2)\exp(-0.0824\zeta^2), & \text{otherwise,} \end{cases} \quad (5.24)$$

$$u_{-1}^{var} = \begin{cases} 1.3278(53.1007 - 0.5\zeta^2), & \text{if } |\zeta| \leq 8.5 \\ 1.3278(114177.278 - 31226.158|\zeta| + 2184.067\zeta^2)exp(-0.0824\zeta^2), & \text{otherwise,} \end{cases} \quad (5.25)$$

$$u_{tot}^{var} = \begin{cases} 5.6839(95.4599 - 0.5\zeta^2), & \text{if } |\zeta| \leq 13.425 \\ 5.6839(4.8883 \times 10^{25} - 7.4283 \times 10^{24}|\zeta| + 2.8227 \times 10^{23}\zeta^2)exp(-0.2779\zeta^2), & \text{otherwise,} \end{cases} \quad (5.26)$$

where the numbers are rounded up to four decimal places. The analytical expressions of the sub-component densities obtained from the VM is in excellent agreement with the numerical profiles (see Fig.5.4(a)). Note that, in Eq.5.26 the coefficients of the total number density might look very large. Still, for $|\zeta| \geq 13.43$ where the expression is valid, the contribution coming from the exponential part is so small that the combined contribution asymptotically goes to zero at large distances. Subtracting the variationally estimated u_1 and u_{-1} components from this total density expression leads to the VM estimated profile of the u_0 component that matches accurately with the numerical profile (see the inset of Fig.5.4(b))

From a physical perspective, the high-density expressions of u_0 and $u_{\pm 1}$ (Eq.5.7-5.9) were found by getting rid of the kinetic terms in the Eq.5.5-5.6. So, the high-density expressions given in Eq.5.7-5.9 are true as long as all the sub-components are in the high-density region. The low-density behavior of the $u_{\pm 1}$ component near the T-F radius also, in turn, affects the u_0 component in this region. As the variational method can estimate $u_{\pm 1}$ in the low-density region, it successfully provides the full analytical profile.

We have made a case study of the PM state which is a multi-component stationary state that becomes the ground state for a range of linear and quadratic Zeeman strengths. For the purpose of comparison with numerical simulation, we have chosen 1-D harmonic trapping and particular values of p' , q' , and the number of condensate particles N .

Note that, the VM is an approximation scheme that works really well in estimating the sub-component number densities (also the mean fields) and produces a very good estimation of the vector order parameter of the spin-1 system, even when the interaction coefficients c_1 and c_0 are tuned to have comparable strengths. Like other approximate

methods, it has some limitations as well. For example, at a large distance from the center of the trap (very large ζ), where the total density u_{tot}^{VM} and $u_{\pm 1}^{VM}$ are very close to zero and can be considered negligible, we find that the total density is slightly lesser than the combined contribution of the ± 1 sub-components hence, making u_0^{VM} slightly negative which is not physical. For this reason, we have taken the contribution up to a large ζ after which we assume that u_0 goes to zero. Thus, the kinetic energy contribution is included and considered up to a large distance without discontinuity.

Comparison with single-mode approximation (SMA)

To emphasize the requirement of the variational method, we will use the single-mode approximation, which is a widely adopted method for the study of spin-oscillation dynamics in spinor condensates. As the name suggests, all the sub-components are assumed to follow the same spatial variation under SMA [83],

$$\psi_m(\mathbf{r}, t) = \sqrt{N}\xi_m(t)\psi_{SMA}(\mathbf{r})\exp\left(-\frac{i\mu t}{\hbar}\right), \quad (5.27)$$

where, $\psi_{SMA}(\mathbf{r})$ is the spatial mode and $\xi_m(t)$ is, in general, a complex quantity that obeys, $\sum_{m=-1}^{m=1} |\xi_m(t)|^2 = 1$. For 1D harmonic confinement, we will use the same scaling as done in Eq.5.3-5.4 where,

$$\psi_{SMA}(\zeta) = \sqrt{2\pi l_y^2 l_x} \psi_{SMA}(\mathbf{r}). \quad (5.28)$$

The solution of

$$\left[-\frac{1}{2} \frac{d^2}{d\zeta^2} + \frac{1}{2} \zeta^2 + \lambda_0 N |\psi_{SMA}(\zeta)|^2 \right] \psi_{SMA}(\zeta) = \mu' \psi_{SMA}(\zeta), \quad (5.29)$$

subjected to the constraint

$$\int_0^\infty d\zeta |\psi_{SMA}(\zeta)|^2 = 1, \quad (5.30)$$

determines the mode function $\psi_{SMA}(\zeta)$. The dynamics of the normalized spinor $\xi_m(t)$ is dictated by,

$$i \frac{d\xi_{\pm 1}}{d\tau} = (\mp p' + q') \xi_{\pm 1} + \tilde{\lambda}_1 \left[(\rho_{\pm 1} + \rho_0 - \rho_{\mp 1}) \xi_{\pm 1} + \xi_0^2 \xi_{\mp 1}^* \right], \quad (5.31)$$

$$i\frac{d\xi_0}{d\tau} = \tilde{\lambda}_1 \left[(\rho_1 + \rho_1)\xi_0 + 2\xi_1\xi_{-1}\xi_0^* \right], \quad (5.32)$$

where $\rho_m \equiv |\xi_m(t)|^2$ and τ is related to time t as, $\tau = \omega_x t$. The effective volume of the system, $V^{eff} \equiv 4\pi l_x l_y l_z \left(\int_{-\infty}^{\infty} d\zeta |\psi_{SMA}(\zeta)|^4 \right)^{-1}$ determines the parameter $\tilde{\lambda}_1$ [83] as

$$\tilde{\lambda}_1 \equiv \frac{c_1 N}{\hbar \omega_x V^{eff}} = \frac{\lambda_1 N}{2} \int_{-\infty}^{\infty} d\zeta |\psi_{SMA}(\zeta)|^4, \quad (5.33)$$

which appears in Eq.5.31-5.32. The normalized spinor is a complex quantity that can be represented in terms of the fractional population ρ_m with a phase part,

$$\xi_m = \sqrt{\rho_m} \exp\left(-i\theta_m\right) \exp\left(ip'm\tau\right). \quad (5.34)$$

This simplifies Eq.5.31-5.32 further,

$$\frac{d\rho_0}{d\tau} = -2\tilde{\lambda}_1 \rho_0 \sqrt{(1-\rho_0)^2 - f_z^2} \sin\theta_r, \quad (5.35)$$

$$\frac{d\theta_r}{d\tau} = -2\tilde{\lambda}_1 \frac{(1-2\rho_0)(1-\rho_0) - f_z^2}{\sqrt{(1-\rho_0)^2 - f_z^2}} \cos\theta_r + 2q' - 2\tilde{\lambda}_1(1-2\rho_0), \quad (5.36)$$

where, $f_z = |\xi_1|^2 - |\xi_{-1}|^2$, and θ_r is the relative phase. From ρ_0 , one can get to the population fraction in the other two components, i.e., $\rho_{\pm 1} = (1 - \rho_0 \pm f_z)/2$ [83].

We select an experimentally relevant case of $p = 0$ and $q = 0.3$, which also corresponds to the PM state in the ground state, to compare the SMA with the numerical results. Note that, the reason to take $p = 0$ is to draw a parallel with the standard procedure used for the application of SMA, where the contribution coming from the linear Zeeman term is bypassed by moving to a rotating frame which effectively sets $p = 0$ [144].

To estimate the mode function, which is the same for all the spin components under SMA, one has to numerically solve Eq.5.29. Following that, the stationarity condition can be employed in Eq.5.35-5.36 to find the population fraction for different sub-components. When $f_z = 0$, for PM state ($\theta_r = 0$), we find $\tilde{\lambda}_1 \simeq -0.2703$, $\rho_0 \simeq 0.777$ and $\rho_{\pm 1} \simeq 0.111$. From these population fractions, one can determine the sub-component densities as, $u_m^{SMA} = N\rho_m |\psi_{SMA}(\zeta)|^2$.

We observed that the total density profile obtained from SMA ($N|\psi_{SMA}(\zeta)|^2$) is in

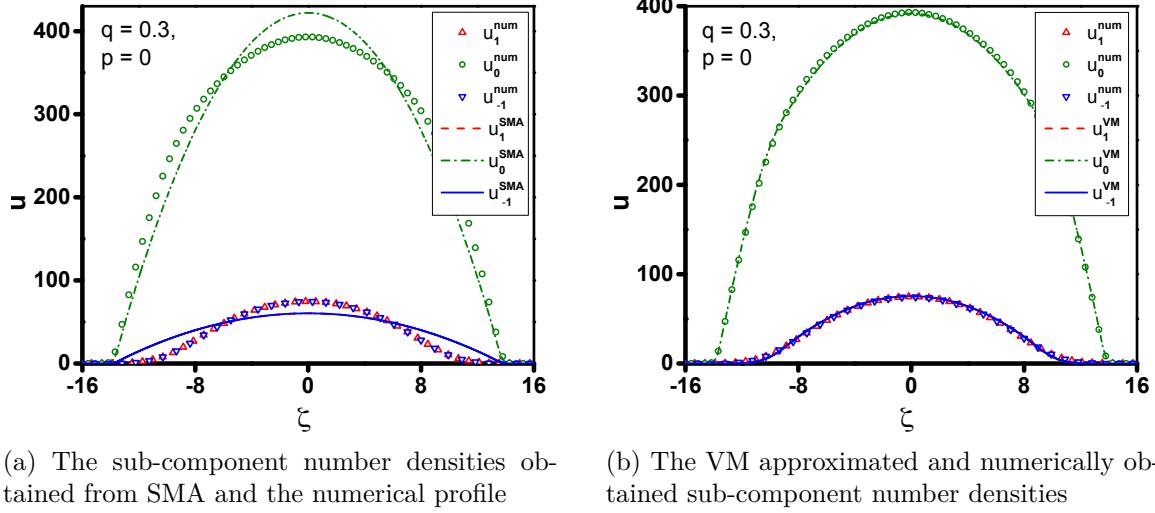


Figure 5.5: (a): The sub-component density profiles obtained from the SMA (u_1 , u_0 and u_{-1} components shown in red dash, green dash-dot, and blue solid lines respectively) are compared with the numerical profile (u_1 , u_0 and u_{-1} components shown in red, green and blue markers). Though the SMA total number density profile agrees with the numerical total number density distribution (not shown here), the SMA overestimates u_0 and underestimates both $u_{\pm 1}$ near the center of the trap. (b): The VM estimated sub-component profiles for the case of $p = 0$ and $q = 0.3$ is in excellent agreement with the multi-modal distribution obtained from the numerical estimation near the center of the trap as well as in the low-density region.

good agreement with the numerically obtained total number density. This is important for an accurate determination of $\tilde{\lambda}_1$ (Eq.5.33). Still, the sub-component density profiles as obtained from SMA do not agree at all with the numerically obtained profiles (see Fig.5.5(a)). In comparison to the numerical profile, the SMA overestimates the u_0 component and underestimates the $u_{\pm 1}$ near the center of the trap. While the numerical profile suggests that the $u_{\pm 1}$ components approach zero much earlier than the u_0 component, it is obvious that according to SMA, they will vanish at an equal distance from the trap center. Note that, it is well-known that SMA is not exact even in the ground state for the PM state, which is also known as the broken-axisymmetry phase [83]. The inaccuracy of SMA further emphasizes the fact that the sub-components do not follow a single spatial mode for the PM state. Thus, a multi-modal analysis is required. Note that, the accurate determination of the sub-component densities is important to estimate the total energy as well. In Fig.5.5(b) we demonstrate that the sub-component density distributions as obtained from the multi-modal VM are in excellent agreement with the numerical simulation for this experimentally relevant case.

5.2.3 Anti-ferromagnetic state

In this section, we will present a brief study on the anti-ferromagnetic state, which is the other possible multi-component stationary state that becomes the ground state for ^{23}Na , which possesses an anti-ferromagnetic type of spin interaction. For the ^{23}Na -condensate, we set the same trapping frequencies corresponding to 1-D confinement as mentioned earlier for the ferromagnetic type condensate. The oscillator length in the elongated direction is $l_x = 2.97 \mu\text{m}$ and the same in the transverse direction is $l_{yz} = 0.59 \mu\text{m}$. Note that, although we consider the same trapping geometry, the oscillator length scale for ^{23}Na and ^{87}Rb condensates are different due to the different masses of the species. The spin-independent and spin-dependent interaction parameters are $\lambda_0 = 46.16 \times 10^{-3}$ and $\lambda_1 = 7.43 \times 10^{-4}$, corresponding to the values given in [83]. For a range of linear and quadratic Zeeman terms, the anti-ferromagnetic (AF) state is found to be favorable as the ground state. For the purpose of numerical study, we will specifically focus on the particular case where $p' = 0.2$ and $q' = -0.5$. Though the conclusions are independent of these particular choices.

As long as the u_1 and u_{-1} sub-components are non-zero, the T-F approximation gives an estimation of the total as well as sub-component number densities (see Table 5.1),

$$u_1^{TF} = \frac{\mu' - q' - \zeta^2/2}{2\lambda_0} + \frac{p'}{2\lambda_1}, \quad (5.37)$$

$$u_{-1}^{TF} = \frac{\mu' - q' - \zeta^2/2}{2\lambda_0} - \frac{p'}{2\lambda_1}. \quad (5.38)$$

As we have chosen a positive value of p' , and for this case, $\lambda_1 > 0$, the u_{-1} component goes to zero much faster than the other one. So, beyond the T-F radius of the u_{-1} component, the AF state ceases to exist but the sole presence of the u_1 component signifies the ferromagnetic state. Thus, according to T-F approximation, the situation is domain-like with the AF state at the center of the trap followed by the ferromagnetic state, F1, (see Table 5.1) that appears in a region with $|\zeta| > \zeta_{-1}^{TF}$. Just like the PM state that we have discussed in detail earlier, the numerical simulation does not indicate any domain-like situation. Rather the AF state is found to be present for all values of ζ . We follow the same procedure for the variational method as discussed in the context of the PM state. When both the sub-components are in the high-density regions, one can write the

densities by neglecting the derivative terms in the phase equations that lead to,

$$u_{\pm 1}^{in} = k_{\pm 1} \left[\frac{\mu'_{\pm 1} - \zeta^2/2}{\lambda_0} \right], \quad (5.39)$$

where, $k_{\pm 1} = 1/2$ and, $\mu'_{\pm 1} = \mu' - q' \pm \frac{\lambda_0}{\lambda_1} p'$. By definition, the sub-component density u_0 is zero for the AF state.

Note that, the high-density expressions are valid as long as both the sub-component density is high enough so that the derivative terms can be safely ignored. But for $p' = 0.2$ and $q' = -0.5$, the u_{-1} component has a lesser T-F radius than the other component. As a result, near the T-F radius of the u_{-1} component, the high-density expression of the u_1 component would be invalid, for the reasons stated earlier. In the high-density region, the total density follows,

$$u_{tot}^{in} = k_{tot} \left[\frac{\mu'_{tot} - \zeta^2/2}{\lambda_0} \right], \quad (5.40)$$

where $k_{tot} = 1$. Following the same procedure as described for the PM state, one can apply the VM for the total density and the sub-component density u_{-1} . Now, if one writes the low-density expressions of the u_{-1} and u_{tot} as

$$u_m^{out} = \frac{k_m}{\lambda_0} \left(a_m + c_m |\zeta| + d_m \zeta^2 \right) \exp \left(- \frac{\zeta^2}{b_m} \right), \quad (5.41)$$

the coefficients will have the same expressions as given in Eq.5.19a-5.19d. Following the same method as explained earlier, one can minimize the total energy corresponding to this stationary state in the parameter space of the matching points ζ_{tot} and ζ_{-1} which provides the analytical form of the full profile of the condensate in terms of the total density and the u_{-1} component. By subtracting the u_{-1} component from the total density profile one can get to the u_1 component. For the previously mentioned p' and q' values, the total energy is minimized for $\zeta_{tot}^{mat} = 8.36$ and $\zeta_{-1}^{mat} = 6.08$. These also produce the analytical formulae of the total density and the u_{-1} components. The density expression for u_1 component can be obtained by subtracting the other sub-component density from the total density.

The VM shows that the T-F approximated domain-like situation is incorrect and justifies the fact that the kinetic energy terms cannot be neglected near the T-F radius for the

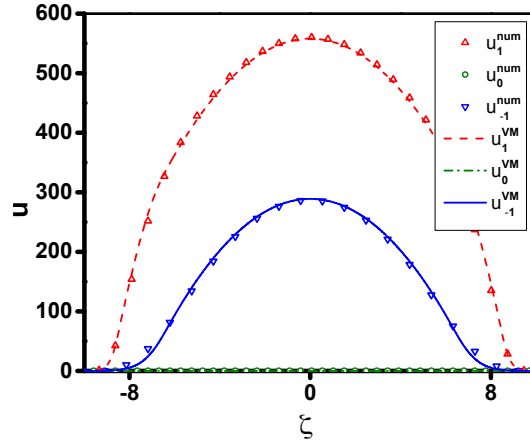


Figure 5.6: Sub-component density expressions obtained via the VM (u_1 , u_0 and u_{-1} components shown in the red dash, green dash-dot, and blue solid lines respectively) and the numerical density profiles (u_1 , u_0 and u_{-1} components shown in red, green and blue markers) for the anti-ferromagnetic state are plotted with distance ζ from the trap center when the Zeeman terms are fixed at $p' = 0.2$ and $q' = -0.5$. The VM profile and the numerical profiles agree for both the sub-components and rule out any possibility of having a domain-like situation.

sub-component which is of smaller density, in this case, the u_{-1} component. The VM also produces a low-density expression of the u_{-1} component which has a small but non-zero presence beyond u_{-1}^{TF} . Thus, it is only the AF state that is present for all regions of space. Moreover, the analytic number density expressions obtained from the VM corresponding to each sub-component are in fair agreement with the numerically obtained profiles (see Fig.5.6).

5.3 Phase transition between PM and polar states under confinement

In the previous section, we considered the case of spin-1 condensate under 1-D harmonic confinement. We have shown that the T-F approximation and the SMA produce inaccurate results for the multi-component ground states. The variational method, on the other hand, analytically obtains the correct profile of the ground states.

In this section, we employ the variational method for estimating the phase transitions between different ground states of a trapped spin-1 BEC, especially when the multi-component states are involved. We will focus on the phase transition between the PM and polar state. This phase transition is of importance in the context of the Kibble-Zurek

mechanism and related spin-vortex generation [83, 145–147]. We consider a spin-1 BEC with the ferromagnetic type of spin-spin interaction inside a 3-dimensional (3-D) isotropic harmonic confinement. To apprehend the contrast and similarity of this phase transition in a trapped condensate with that of the homogeneous (in the absence of trapping) situation, we will briefly recapitulate the homogeneous results shown in Chapter 2 (Fig.2.1).

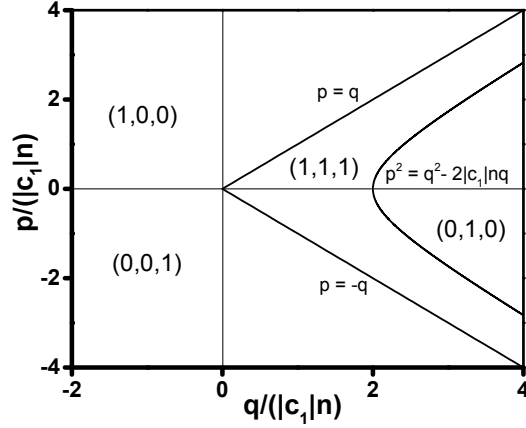


Figure 5.7: The phase diagram of the spin-1 condensate with a ferromagnetic type of spin-spin interaction ($c_1 < 0$) in the absence of any confinement. The ferromagnetic, PM, and polar states are favorable to become the ground states depending on the linear and quadratic Zeeman terms, p and q . The number density n , being a constant over space in the absence of any confinement, can be used to scale the p and q axes. In this scaling, the phase diagram becomes universal in the sense that this diagram does not vary if the number density changes.

The phase transition between the PM and the polar state happens for the ferromagnetic type of spin-spin interaction ($c_1 < 0$). In the absence of confinement, the number density becomes a constant i.e., there is no spatial dependence. For $c_1 < 0$, the phase diagram of the homogeneous condensate, Fig.5.7 (same as Fig. 2.1(c)), shows different stationary states that are favorable as the ground state in certain regions of the (q, p) parameter space. For the negative quadratic Zeeman term ($q < 0$), the ferromagnetic states are the ground states, where one of them is favorable depending on the sign of the linear Zeeman term. For $q > 0$, if the quadratic Zeeman term is greater than the absolute value of the linear term (i.e., $q \geq |p|$) then the PM state becomes the ground state as long as $p^2 \geq q^2 - 2|c_1|nq$ is satisfied. The polar state occupies the remaining part (i.e., $p^2 \leq q^2 - 2|c_1|nq$) of the (q, p) parameter space. For the homogeneous condensate, the PM-polar phase transition occurs at $p^2 = q^2 - 2|c_1|nq$, where the energies of the two states become equal and for a higher value of q for the same p , the PM state is non-existent.

For an isotropic 3-D confinement of trapping frequency ω , we scale the number density and the interaction parameters as,

$$c_0 = \frac{4\pi}{3} l_{osc}^3 \lambda_0 \hbar \omega, \quad c_1 = \frac{4\pi}{3} l_{osc}^3 \lambda_1 \hbar \omega, \quad (5.42)$$

$$u_m = \frac{4\pi}{3} l_{osc}^3 n_m, \quad r = l_{osc} \eta \quad (5.43)$$

where, $l_{osc}^2 = \hbar/(m\omega)$ is the oscillator length and η is the radial distance from the trap center. For this choice of scaling, the phase equations,

$$\left\{ -\frac{1}{2} \frac{1}{\eta^2} \frac{d}{d\eta} \left(\eta^2 \frac{d}{d\eta} \right) + \frac{1}{2} \eta^2 + \lambda_0 u - \mu' + \lambda_1 (u_1 + u_{-1} + 2\sqrt{u_{-1}u_1} \cos \theta_r) \right\} \sqrt{u_0} = 0, \quad (5.44)$$

$$\left\{ -\frac{1}{2} \frac{1}{\eta^2} \frac{d}{d\eta} \left(\eta^2 \frac{d}{d\eta} \right) + \frac{1}{2} \eta^2 + \lambda_0 u - \mu' \pm \lambda_1 (u_1 - u_{-1}) \mp p' + q' \right\} \sqrt{u_{\pm 1}} + \lambda_1 u_0 (\sqrt{u_{\pm 1}} + \sqrt{u_{\mp 1}} \cos \theta_r) = 0, \quad (5.45)$$

assumes a similar structure as Eq.5.5-5.6, where, due to isotropy, we have only considered the radial part of the Laplacian in the spherical polar coordinate. To implement the VM, we follow the same procedure discussed for the 1-D harmonic confinement in the previous section. For the PM state, the unknown coefficients in the number density expression of the low-density region (Eq.5.21 with radial distance η in place of ζ) follow the same expressions Eq.5.19a-Eq.5.19d under 3-D harmonic confinement.

Integrating the sub-component densities would provide the total number of condensate particles, which in the non-dimensional form can be written as (following the scaling Eq.5.42-5.43)

$$\sum_{m=-1}^1 \left[\int_0^{\eta_m^{mat}} u_m^{in}(\mu', \eta) \eta^2 d\eta + \int_{\eta_m^{mat}}^{\infty} u_m^{out}(\mu', \eta, \eta_m^{mat}) \eta^2 d\eta \right] = \frac{N}{3}. \quad (5.46)$$

From this equation, one can estimate the parameter μ' for the matching points η_m^{mat} for a condensate with N particles. Following the same procedure of minimizing the total energy, the matching points are obtained.

For the polar state, the implementation of the variational method is straightforward. Only the u_0 component is populated for the polar state, hence Eq.5.45 becomes trivial. The number density expression in the high-density region for this state can be obtained

by neglecting the Laplacian term in Eq.5.44,

$$u_0^{in} \Big|_{polar} = \frac{\mu' - \frac{1}{2}\eta^2}{\lambda_0}. \quad (5.47)$$

In the low-density region we assume,

$$u_0^{out} \Big|_{polar} = \frac{1}{\lambda_0} \left(a_0 + c_0\eta + d_0\eta^2 \right) \exp\left(-\frac{\eta^2}{b_0} \right), \quad (5.48)$$

where the coefficients a_0 , b_0 , c_0 , and d_0 follows the same expressions as Eq.5.19a-Eq.5.19d. Following the same method discussed earlier, the total energy is minimized in the one-dimensional parameter space of η_0^{mat} . Note that, the total energy of the polar state does not depend on the linear and quadratic Zeeman terms.

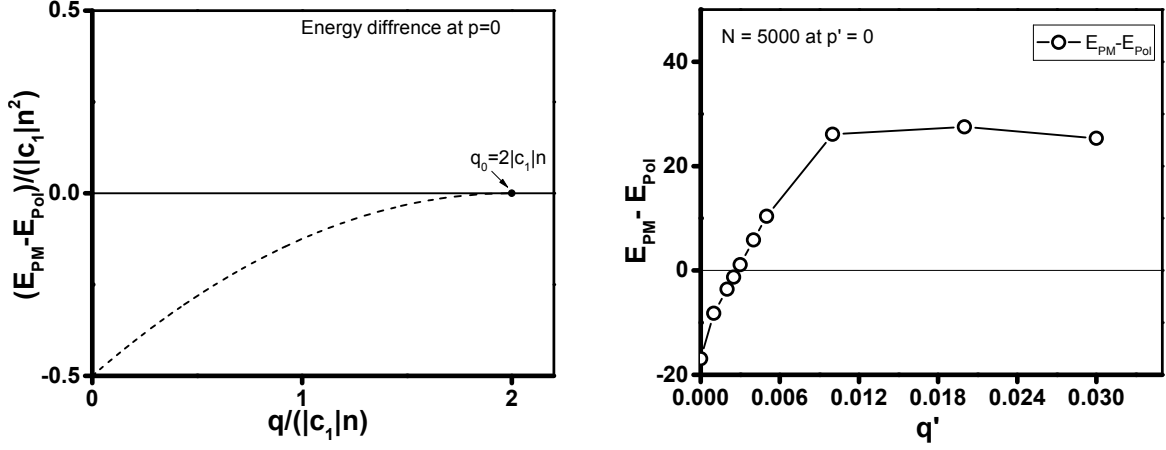
We consider a 3-D isotropic harmonic confinement of trapping frequency $\omega = 2\pi \times 100 \text{ Hz}$. The oscillator length scale corresponding to this choice of trapping frequency is $l_{osc} = 1.07 \mu\text{m}$ for For ^{87}Rb . The interaction parameters defined in Eq.5.42-5.43 are $\lambda_0 = 1.484 \times 10^{-2}$ and $\lambda_1 = -5.249 \times 10^{-5}$.

The VM estimates the total energy of the polar state and the PM state for different p' and q' , a comparison of which would reveal the phase boundary for the trapped condensate. For homogeneous condensate, the energy difference between these two states at $p = 0$ (Fig.5.8(a)) indicates that the energy of the PM state is lower than the polar state for small positive values of q . As the strength of the quadratic Zeeman term is increased, the energy difference reduces, and at the transition point $q_t = 2|c_1|n$, it vanishes. At this point, the number density of the $m = \pm 1$ projection,

$$n_{\pm 1}^{PM} \Big|_{hom.} = \frac{(q \pm p)^2}{4q^2} \left(\frac{-p^2 + q^2 + 2c_1 n q}{2c_1 n q} \right) n \quad (5.49)$$

also vanishes [83], hence the PM state ceases to exist.

For the trapped condensate at $p = 0$, one can estimate the q_0 , where the peak density (number density at the center of the harmonic trap) of the $u_{\pm 1}$ vanishes and the PM state ceases to exist for $q > q_0$. The VM estimated energy difference between the PM and the polar state for $N = 5000$, shown in Fig.5.8(b) indicates that the phase transition happens



(a) The energy difference of PM and polar state in absence of trapping.

(b) The VM approximated energy difference of the PM and polar state under 3-D isotropic harmonic confinement.

Figure 5.8: Subfig-(a): For condensates with the ferromagnetic type of spin-spin interaction ($c_1 < 0$), the energy difference of the PM and the polar state scaled with the constant number density is plotted against the variation of q at $p = 0$ for condensates in the absence of any trapping. At $q \approx 0$, the energy corresponding to the PM state is lower than that of the polar state, making the PM state favorable to become the ground state. As q increases, the energy difference reduces, and at the transition point ($q = 2|c_1|n$ at $p = 0$), the PM state energy becomes equal to that of the polar state. At this point, the sub-component density $n_{\pm 1}$ vanishes. Hence beyond this point, the PM state does not exist. Subfig-(b): The VM estimated energy difference between the PM and polar state under the 3-D harmonic trapping for 5000 condensate particles with varying q' at $p' = 0$. The total energy of the PM state is lower than that of the polar state for small values of the quadratic Zeeman term. The energy difference in the trapped situation indicates that the phase transition happens at $q' \simeq 0.0027$, which is much lower than $q' \simeq 0.0377$, beyond which the PM state ceases to exist.

at $q'_t = 0.0027$, which is an order of magnitude lower than $q'_0 \simeq 0.0377$ beyond which the PM state ceases to exist under trapped conditions.

As is evident from Fig.5.7, for the homogeneous condensate, the constant number density is used in the scaling of p and q . As a result, the whole phase diagram is universal with respect to number density variation for any homogeneous spin-1 condensate with the ferromagnetic type of spin-spin interaction. In contrast, in the presence of confining potential, the number density varies over space and even the peak density (number density at the center of the trap) is different for different stationary states. In this case not the number density but the number of condensate particles are of importance.

For a choice of p' , the VM is employed to estimate the q' value for which the energy difference of the PM and the polar state vanishes. Following the same procedure for

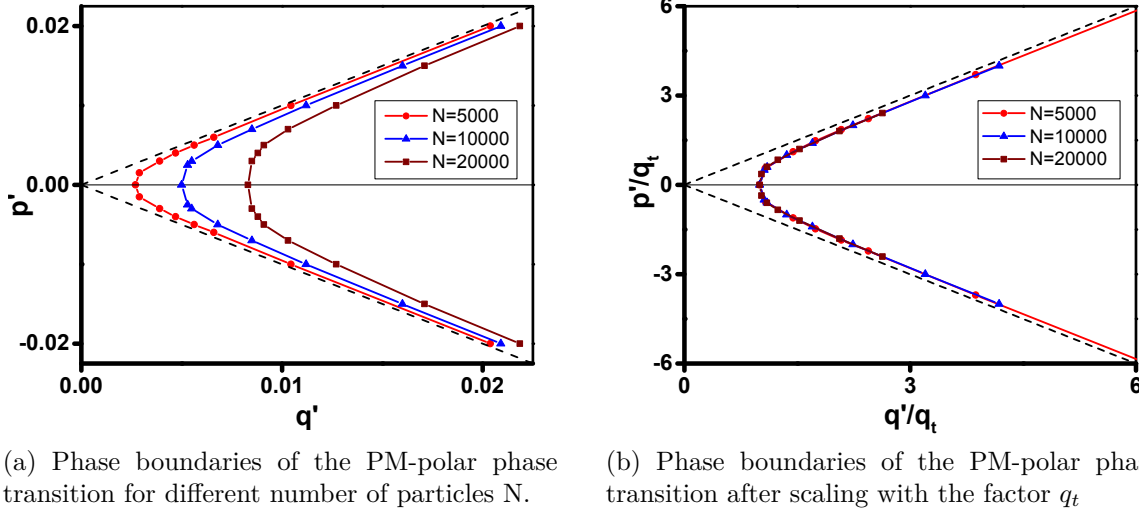


Figure 5.9: Subfig-(a): PM-polar phase transition boundary in (q, p) parameter space under harmonic confinement for 5000, 10000, and 20000 condensate particles (in the red circle, blue triangle, and wine box markers). All the phase boundaries asymptotically follow $|p'| = q'$ line for large values of p' and q' , similar to the homogeneous condensate, while if we increase the number of particles, the range of q' at $p' = 0$, for which the PM state becomes the ground state increases. Subfig-(b): The phase boundaries are plotted by scaling the quadratic and linear Zeeman terms with q_t , where q_t is the quadratic Zeeman strength for which the PM-polar transition happens at $p' = 0$ for a particular N . In these scaled coordinates, all the phase boundaries approximately follow the equation, $(q'/q_t)^2 - (p'/q_t)^2 = 1$, the equation of a hyperbola, similar to the homogeneous condensates.

different choices of p' , one can get the phase boundaries (Fig.5.9(a)) in the q', p' parameter space for a range of condensate particles.

These phase transition boundaries for different condensate particles asymptotically approach the $|p'| = q'$ line for large values of q' . At the same value of the linear Zeeman term p' , with an increase in the number of particles, the phase transition happens at a higher value of q' . For example, at $p' = 0$, the phase transition happens at $q_t = 0.0027$ for 5000 particles, which gets shifted to $q_t = 0.005$ for $N=10000$ and to a higher value of $q_t = 0.0083$ for 20000 particles.

A natural query, therefore, would be whether there exists a scaling factor for trapped condensate which brings these phase boundaries for different numbers of condensate particles (Fig.5.9(a)) to the same plot. The asymptote of unit slope indicates, if we scale the p' and q' with $q_t(N)$, which is the q value at $p = 0$, where the transition happens for a particular N , then all these phase boundaries merge (Fig.5.9(b)) and approximately follow $(q'/q_t)^2 - (p'/q_t)^2 = 1$, the equation of a hyperbola, similar to the homogeneous

condensate.

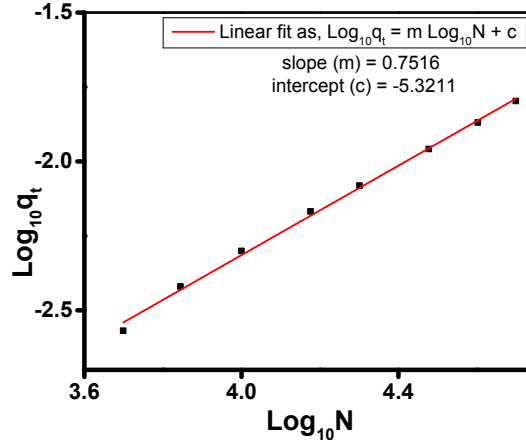


Figure 5.10: Figure shows the scaling q_t to vary with the number of particles as a power function $q_t \propto N^m$. Using a linear fit, the slope of $\log q_t$ vs $\log N$, which corresponds to the power m is obtained, i.e., $m \approx 0.75$. This shows that the scaling factor q_t varies approximately as $q_t \propto N^{3/4}$, for 3-D isotropic harmonic trapping.

To determine the dependence of the scaling factor q_t on the number of condensate particles, we additionally estimated q_t for $N=7000, 15000, 30000, 40000,$ and 50000 particles. Assuming a power-law dependence, from the $\log q_t$ vs $\log N$ plot, we find that the scaling factor depends on the number of particles roughly as $q_t \sim N^{3/4}$ (Fig.5.10).

Note that, in the absence of trapping, the PM-polar phase transition happens at a quadratic Zeeman term, $q_t = 2|c_1|n$ at $p = 0$. In that case, the number density is a constant. If we map the T-F approximated trapped condensate to the homogeneous counterpart by replacing the constant density with the T-F approximated average density, one can get to an estimation of the q_t^{TF} .

The total number present in the condensate can be obtained by integrating the number density, which in the T-F approximation,

$$\int_0^R 4\pi\zeta^2 \left[\mu'_{TF} - \frac{1}{2}\zeta^2 \right] d\zeta \sim N, \quad (5.50)$$

gives a relation between the T-F radius R and the number of particles N . As $\mu'_{TF} = R^2/2$, the T-F radius varies with N as, $R \sim N^{1/5}$, which leads to the volume $V \sim R^3 \sim N^{3/5}$. So, the average density in the T-F approximation depends on N as, $n_{avg} = N/V \sim N^{2/5}$.

If we replace the constant density with the T-F approximated average density, one

can estimate $q_t^{TF} \sim N^{2/5}$. In contrast, the multi-modal VM indicates that this scaling factor is $q_t \sim N^{3/4}$ for the isotropic 3-D harmonic confinement. This result exposes the limitation of the T-F approximation in comparison with more accurate results even in large condensates.

5.4 Discussion

In this chapter, we looked into the multi-component states that become the ground state of a harmonically confined spin-1 BEC in the presence of the magnetic field. Even in the so-called "T-F regime", where the overall density of the condensate is high enough to supposedly neglect the kinetic energy contribution, the T-F approximation indicates to a wrong physical conclusion about domain formation in the ground state. Moreover, the T-F approximated profile for the domain structure has a discontinuity (for example, the u_0 component for PM state has a discontinuity, shown in Fig.5.2). Whereas, the numerical evidence suggests that the multi-component states are solely present in the ground state.

Although, for multi-component states like the PM state, the widely used SMA indicates that there is no domain structure in the ground state, we demonstrate that the SMA overestimates one of the sub-components while underestimating the others. The condensate profile obtained from the SMA also suggests that all the components tend to vanish at a similar distance from the trap center, which is also in stark contrast with the numerical profile. This inaccuracy in estimating the sub-component density profiles would come costly, as an accurate estimation of the same is required to compute the total energy of the PM state, which is the ground state in this case. This requires a general multi-modal treatment taking into consideration the kinetic energy term, which the VM provides. The VM captures the multi-component states because it can accurately estimate trapped density profiles even in the low-density region, where the kinetic energy contribution is the most significant and cannot be neglected. While the T-F approximated condensate profile has a discontinuity, the VM analytically estimates smooth number density profiles that agree with accurate numerical simulation.

The VM can be implemented in higher dimensions where numerical simulation is costlier. For 3-D isotropic harmonic trapping, the VM estimates the phase transition between the PM and the polar state for the ferromagnetic type of spin-spin interaction,

which indicates that the phase transition in a trapped situation is significantly different than the homogeneous condensate. The VM estimation of the phase transition boundaries for different particle numbers shows a universal behavior under a specific scaling of the p' and q' coordinates. This scaling factor arose out of the VM calculation. A similar analysis can be employed for phase transitions involving other states that would produce a complete phase diagram of a spin-1 condensate under harmonic confinement.

Chapter 6

Conclusion and future prospects

6.1 Major findings

In the following, the major findings of this thesis are summarized.

- We have developed a general method to analytically explore the domain formation possibilities for a trapped spin-1 condensate under the Thomas-Fermi approximation. Applying the Thomas-Fermi approximation, the energy densities of all the stationary states can be calculated for a generic trapping potential. Under a single essential constraint of the same chemical potential for the domain-forming structures, the Thomas-Fermi approximated energy densities are compared locally for various magnetic fields (linear and quadratic Zeeman terms). The whole procedure is valid for any generic potential as discussed in detail in Chapter 3. This procedure can be easily extended to higher spin ($f > 1$) systems. This is a general method and allows one to explore the domain structures in a unified way, rather than searching on a case-by-case basis.
- The Thomas-Fermi approximation neglects the kinetic energy contribution completely. This is assumed to be true for large condensates. When the density is high enough, the interaction energies become large and in comparison, the kinetic energy contribution becomes less significant. But even for large condensates, situations may arise when competing ground state candidates differ in energy, which is of the order of the kinetic energy contribution. In such situations, the Thomas-Fermi ap-

proximation will break down in predicting the correct ground state as the kinetic energy contribution, which the Thomas-Fermi approximation disregards, can alter the prediction. In Chapter 4 we discussed such a situation and proposed a multi-modal variational method that takes the kinetic energy contribution into account and analytically produces more refined estimations of the ground state structures and related quantities.

- When the density is not high enough (for example, in the low-density region, which is away from the trap center of a harmonically trapped condensate), one cannot neglect the kinetic energy completely. Even for large condensates, the effect of the kinetic energy is taken into account in the multi-modal variational method. That is why this method can produce the condensate profile in the low-density region with great accuracy, which is beyond the capability of the Thomas-Fermi approximation. On top of that, this method can produce the analytical number density profile even for condensates with particle numbers as low as 500, where needless to say, the Thomas-Fermi approximation is not at all accurate.
- In the presence of the magnetic field, the multi-component states are not bound to follow a single spatial mode, and in situations like this, the Thomas-Fermi approximation wrongly indicates the phenomenon of domain formation in the ground state (in Chapter 5). Away from the trap center, if one of the sub-components tends to vanish faster than the other components, the Thomas-Fermi approximation is bound to predict a domain structure in the ground state. This happens irrespective of the higher number of condensate particles (in the so-called Thomas-Fermi regime). On the other hand, the well-known method of single-mode approximation is also inaccurate in estimating the sub-component profiles.
- In the absence of a trustworthy analytical procedure, the multi-modal variational method produces an accurate description of the multi-component ground states of a trapped condensate in the presence of the magnetic field. The variational method, being a multi-modal method, treats each sub-components separately and can account for the low-density or tail part of the sub-component profiles. The accurate determination of this tail part of the condensate especially, for the sub-component(s) that tends to vanish earlier than the other components gives the idea of why there

is no domain-formation in the ground state involving the multi-component states. This further emphasizes that the general intuition that the kinetic energy, as well as the tail part, can be neglected for large condensates (in the so-called T-F limit) might produce an inaccurate physical picture when dealing with multi-component BEC, no matter how large the condensate may be. In higher dimensional space, where the simulations are computationally expensive, the variational method can be readily used to get the ground state. This method can also be generalized to higher spin systems as well.

- The multi-modal variational method is crucial to analytically obtain the phase diagram of a trapped condensate. Inside a 3-D isotropic harmonic confinement, the variational method estimates the PM-polar phase transition in the q , p parameter space for different condensate particles. These phase boundaries can be compared with that of the homogeneous case. On top of that, the trapped phase boundaries for different numbers of particles show a universal behavior under the scaling of the q , p axes. Similar analysis can be done for other possible phase transitions, that would reveal a complete and phase diagram of the spin-1 condensate under harmonic confinement.

6.2 Future directions

- An interesting direction can be in the studies of instabilities. Generally, the instability analysis is either done numerically or analytically only in the absence of the trapping potential. As the variational method provides accurate analytical expressions of the ground state profiles, this opens up the possibility of analytical studies in the presence of trapping.
- The multi-modal variational method can be extended for a more accurate determination of domain formation. This could rule out some of the domain formation possibilities under the T-F approximation. Under the T-F approximation, one is restricted to search for domain structures only near the center of the trap, but the variational method could relax this restriction. Moreover, if the variational method is extended to the domain forming scenario, it could determine the sub-component profiles of the condensate near the domain boundary thus, estimating the domain

layer energy.

- Having known the ground state one can also investigate the transition to an excited state for example, large-scale oscillations under periodic forcing, vortex structures, and other situations like macroscopic tunneling phenomena.

Publications

Publications

1. P. K. Kanjilal and A. Bhattacharyay, *Physica Scripta* 95, 045702 (2020).
2. Kanjilal, Projjwal Kanti and Bhattacharyay, A., *Eur. Phys. J. Plus* 137, 547 (2022).
3. P. K. Kanjilal and A. Bhattacharyay, *Physica Scripta* 97, 129501 (2022).
4. P. K. Kanjilal and A. Bhattacharyay, arXiv: 2301.06856, Multi-component states for trapped spin-1 Bose-Einstein condensates in the presence of magnetic field (2023).

Bibliography

- [1] Bose. Plancks gesetz und lichtquantenhypothese. *Zeitschrift für Physik*, 26(1): 178–181, Dec 1924. ISSN 0044-3328. doi: 10.1007/BF01327326. URL <https://doi.org/10.1007/BF01327326>.
- [2] James P. Sethna. *Statistical Mechanics: Entropy, Order Parameters and Complexity*. Oxford University Press, Great Clarendon Street, Oxford OX2 6DP, first edition edition, 2006.
- [3] A. Einstein. Quantentheorie des einatomigen idealen gases. *Sitzungber. Kgl. Akad. Wiss.*, (261), 1924.
- [4] A. Einstein. *Quantentheorie des einatomigen idealen Gases. Zweite Abhandlung*, pages 245–257. John Wiley Sons, Ltd, 2005. ISBN 9783527608959. doi: <https://doi.org/10.1002/3527608958.ch28>. URL <https://onlinelibrary.wiley.com/doi/abs/10.1002/3527608958.ch28>.
- [5] F. London. On the bose-einstein condensation. *Phys. Rev.*, 54:947–954, Dec 1938. doi: 10.1103/PhysRev.54.947. URL <https://link.aps.org/doi/10.1103/PhysRev.54.947>.
- [6] N.N.Bogolubov. On the theory of superfluidity. *J. Phys. (USSR)*, 11(1):23–32, 1947. URL https://ufn.ru/pdf/jphysussr/1947/11_1/3jphysussr19471101.pdf.
- [7] Oliver Penrose and Lars Onsager. Bose-einstein condensation and liquid helium. *Phys. Rev.*, 104:576–584, Nov 1956. doi: 10.1103/PhysRev.104.576. URL <https://link.aps.org/doi/10.1103/PhysRev.104.576>.
- [8] Eugene P Gross. Quantum theory of interacting bosons. *Annals of Physics*, 9(2):292–324, 1960. ISSN 0003-4916. doi: [https://doi.org/10.1016/0003-4916\(60\)90001-1](https://doi.org/10.1016/0003-4916(60)90001-1).

- 1016/0003-4916(60)90033-6. URL <https://www.sciencedirect.com/science/article/pii/0003491660900336>.
- [9] L.P. Pitaevskii. Vortex lines in an imperfect bose gas. *JETP*, 13(2):451–454, 1961. URL <http://www.jetp.ras.ru/cgi-bin/e/index/e/13/2/p451?a=list>.
- [10] A. Aspect, E. Arimondo, R. Kaiser, N. Vansteenkiste, and C. Cohen-Tannoudji. Laser cooling below the one-photon recoil energy by velocity-selective coherent population trapping. *Phys. Rev. Lett.*, 61:826–829, Aug 1988. doi: 10.1103/PhysRevLett.61.826. URL <https://link.aps.org/doi/10.1103/PhysRevLett.61.826>.
- [11] T.W. Hänsch and A.L. Schawlow. Cooling of gases by laser radiation. *Optics Communications*, 13(1):68–69, 1975. ISSN 0030-4018. doi: [https://doi.org/10.1016/0030-4018\(75\)90159-5](https://doi.org/10.1016/0030-4018(75)90159-5). URL <https://www.sciencedirect.com/science/article/pii/0030401875901595>.
- [12] William H. Wing. On neutral particle trapping in quasistatic electromagnetic fields. *Progress in Quantum Electronics*, 8(3):181–199, 1984. ISSN 0079-6727. doi: [https://doi.org/10.1016/0079-6727\(84\)90012-0](https://doi.org/10.1016/0079-6727(84)90012-0). URL <https://www.sciencedirect.com/science/article/pii/0079672784900120>.
- [13] Harald F. Hess, Greg P. Kochanski, John M. Doyle, Naoto Masuhara, Daniel Kleppner, and Thomas J. Greytak. Magnetic trapping of spin-polarized atomic hydrogen. *Phys. Rev. Lett.*, 59:672–675, Aug 1987. doi: 10.1103/PhysRevLett.59.672. URL <https://link.aps.org/doi/10.1103/PhysRevLett.59.672>.
- [14] Naoto Masuhara, John M. Doyle, Jon C. Sandberg, Daniel Kleppner, Thomas J. Greytak, Harald F. Hess, and Greg P. Kochanski. Evaporative cooling of spin-polarized atomic hydrogen. *Phys. Rev. Lett.*, 61:935–938, Aug 1988. doi: 10.1103/PhysRevLett.61.935. URL <https://link.aps.org/doi/10.1103/PhysRevLett.61.935>.
- [15] Simon Stellmer, Benjamin Pasquiou, Rudolf Grimm, and Florian Schreck. Laser cooling to quantum degeneracy. *Phys. Rev. Lett.*, 110:263003, Jun 2013. doi: 10.1103/PhysRevLett.110.263003. URL <https://link.aps.org/doi/10.1103/PhysRevLett.110.263003>.

- [16] M. H. Anderson, J. R. Ensher, M. R. Matthews, C. E. Wieman, and E. A. Cornell. Observation of bose-einstein condensation in a dilute atomic vapor. *Science*, 269(5221):198–201, 1995. doi: 10.1126/science.269.5221.198. URL <https://www.science.org/doi/abs/10.1126/science.269.5221.198>.
- [17] NOVA. *Absolute Zero*. NOVA website, <http://www.pbs.org/wgbh/nova/zero/> (accessed April 10, 2008). URL <http://www.pbs.org/wgbh/nova/zero/>.
- [18] K. B. Davis, M. O. Mewes, M. R. Andrews, N. J. van Druten, D. S. Durfee, D. M. Kurn, and W. Ketterle. Bose-einstein condensation in a gas of sodium atoms. *Phys. Rev. Lett.*, 75:3969–3973, Nov 1995. doi: 10.1103/PhysRevLett.75.3969. URL <https://link.aps.org/doi/10.1103/PhysRevLett.75.3969>.
- [19] C. C. Bradley, C. A. Sackett, J. J. Tollett, and R. G. Hulet. Evidence of bose-einstein condensation in an atomic gas with attractive interactions. *Phys. Rev. Lett.*, 75:1687–1690, Aug 1995. doi: 10.1103/PhysRevLett.75.1687. URL <https://link.aps.org/doi/10.1103/PhysRevLett.75.1687>.
- [20] Dale G. Fried, Thomas C. Killian, Lorenz Willmann, David Landhuis, Stephen C. Moss, Daniel Kleppner, and Thomas J. Greytak. Bose-einstein condensation of atomic hydrogen. *Phys. Rev. Lett.*, 81:3811–3814, Nov 1998. doi: 10.1103/PhysRevLett.81.3811. URL <https://link.aps.org/doi/10.1103/PhysRevLett.81.3811>.
- [21] S. Giorgini, L. P. Pitaevskii, and S. Stringari. Condensate fraction and critical temperature of a trapped interacting bose gas. *Phys. Rev. A*, 54:R4633–R4636, Dec 1996. doi: 10.1103/PhysRevA.54.R4633. URL <https://link.aps.org/doi/10.1103/PhysRevA.54.R4633>.
- [22] F. Dalfovo and S. Stringari. Bosons in anisotropic traps: Ground state and vortices. *Phys. Rev. A*, 53:2477–2485, Apr 1996. doi: 10.1103/PhysRevA.53.2477. URL <https://link.aps.org/doi/10.1103/PhysRevA.53.2477>.
- [23] S. Stringari. Collective excitations of a trapped bose-condensed gas. *Phys. Rev. Lett.*, 77:2360–2363, Sep 1996. doi: 10.1103/PhysRevLett.77.2360. URL <https://link.aps.org/doi/10.1103/PhysRevLett.77.2360>.
- [24] Dennis Becker, Maike D. Lachmann, Stephan T. Seidel, Holger Ahlers, Aline N.

- Dinkelaker, Jens Grosse, Ortwin Hellmig, Hauke Müntinga, Vladimir Schkolnik, Thijs Wendrich, André Wenzlawski, Benjamin Weps, Robin Corgier, Tobias Franz, Naceur Gaaloul, Waldemar Herr, Daniel Lüdtke, Manuel Popp, Sirine Amri, Hannes Duncker, Maik Erbe, Anja Kohfeldt, André Kubelka-Lange, Claus Braxmaier, Eric Charron, Wolfgang Ertmer, Markus Krutzik, Claus Lämmerzahl, Achim Peters, Wolfgang P. Schleich, Klaus Sengstock, Reinhold Walser, Andreas Wicht, Patrick Windpassinger, and Ernst M. Rasel. Space-borne bose-einstein condensation for precision interferometry. *Nature*, 562(7727):391–395, Oct 2018. ISSN 1476-4687. doi: 10.1038/s41586-018-0605-1. URL <https://doi.org/10.1038/s41586-018-0605-1>.
- [25] Stuart S. Szigeti, Samuel P. Nolan, John D. Close, and Simon A. Haine. High-precision quantum-enhanced gravimetry with a bose-einstein condensate. *Phys. Rev. Lett.*, 125:100402, Sep 2020. doi: 10.1103/PhysRevLett.125.100402. URL <https://link.aps.org/doi/10.1103/PhysRevLett.125.100402>.
- [26] S. Gupta, K. Dieckmann, Z. Hadzibabic, and D. E. Pritchard. Contrast interferometry using bose-einstein condensates to measure h/m and α . *Phys. Rev. Lett.*, 89:140401, Sep 2002. doi: 10.1103/PhysRevLett.89.140401. URL <https://link.aps.org/doi/10.1103/PhysRevLett.89.140401>.
- [27] Alan O. Jamison, J. Nathan Kutz, and Subhadeep Gupta. Atomic interactions in precision interferometry using bose-einstein condensates. *Phys. Rev. A*, 84:043643, Oct 2011. doi: 10.1103/PhysRevA.84.043643. URL <https://link.aps.org/doi/10.1103/PhysRevA.84.043643>.
- [28] D. Hanneke, S. Fogwell, and G. Gabrielse. New measurement of the electron magnetic moment and the fine structure constant. *Phys. Rev. Lett.*, 100:120801, Mar 2008. doi: 10.1103/PhysRevLett.100.120801. URL <https://link.aps.org/doi/10.1103/PhysRevLett.100.120801>.
- [29] Pranab Dutta, S. Sagar Maurya, Kushal Patel, Korak Biswas, Jay Mangaonkar, Sumit Sarkar, and Umakant D. Rapol. A decade of advancement of quantum sensing and metrology in india using cold atoms and ions. *Journal of the Indian Institute of Science*, Oct 2022. ISSN 0019-4964. doi: 10.1007/s41745-022-00335-8. URL <https://doi.org/10.1007/s41745-022-00335-8>.

- [30] Immanuel Bloch, Jean Dalibard, and Sylvain Nascimbène. Quantum simulations with ultracold quantum gases. *Nature Physics*, 8(4):267–276, Apr 2012. ISSN 1745-2481. doi: 10.1038/nphys2259. URL <https://doi.org/10.1038/nphys2259>.
- [31] N. Dupont, G. Chatelain, L. Gabardos, M. Arnal, J. Billy, B. Peaudecerf, D. Sugny, and D. Guéry-Odelin. Quantum state control of a bose-einstein condensate in an optical lattice. *PRX Quantum*, 2:040303, Oct 2021. doi: 10.1103/PRXQuantum.2.040303. URL <https://link.aps.org/doi/10.1103/PRXQuantum.2.040303>.
- [32] Ruwan Senaratne, Shankari V Rajagopal, Toshihiko Shimasaki, Peter E Dotti, Kurt M Fujiwara, Kevin Singh, Zachary A Geiger, and David M Weld. Quantum simulation of ultrafast dynamics using trapped ultracold atoms. *Nat Commun*, 9(1):2065, May 2018.
- [33] Yoshihisa Yamamoto and Yoshiro Takahashi. *Bose-Einstein Condensation: A Platform for Quantum Simulation Experiments*, pages 265–307. Springer Japan, Tokyo, 2016. ISBN 978-4-431-55756-2. doi: 10.1007/978-4-431-55756-2_13. URL https://doi.org/10.1007/978-4-431-55756-2_13.
- [34] Tupac Bravo, Carlos Sabín, and Ivette Fuentes. Analog quantum simulation of gravitational waves in a bose-einstein condensate. *EPJ Quantum Technology*, 2(1):3, Jan 2015. ISSN 2196-0763. doi: 10.1140/epjqt16. URL <https://doi.org/10.1140/epjqt16>.
- [35] J. Ignacio Cirac and Peter Zoller. Goals and opportunities in quantum simulation. *Nature Physics*, 8(4):264–266, Apr 2012. ISSN 1745-2481. doi: 10.1038/nphys2275. URL <https://doi.org/10.1038/nphys2275>.
- [36] I. M. Georgescu, S. Ashhab, and Franco Nori. Quantum simulation. *Rev. Mod. Phys.*, 86:153–185, Mar 2014. doi: 10.1103/RevModPhys.86.153. URL <https://link.aps.org/doi/10.1103/RevModPhys.86.153>.
- [37] S. I. Mistakidis, A. G. Volosniev, R. E. Barfknecht, T. Fogarty, Th. Busch, A. Foerster, P. Schmelcher, and N. T. Zinner. Cold atoms in low dimensions – a laboratory for quantum dynamics, 2022. URL <https://arxiv.org/abs/2202.11071>.
- [38] G. Roati, M. Zaccanti, C. D’Errico, J. Catani, M. Modugno, A. Simoni, M. Inguscio, and G. Modugno. ^{39}K bose-einstein condensate with tunable interactions. *Phys.*

- Rev. Lett.*, 99:010403, Jul 2007. doi: 10.1103/PhysRevLett.99.010403. URL <https://link.aps.org/doi/10.1103/PhysRevLett.99.010403>.
- [39] T. Kishimoto, J. Kobayashi, K. Noda, K. Aikawa, M. Ueda, and S. Inouye. Direct evaporative cooling of ^{41}K into a bose-einstein condensate. *Phys. Rev. A*, 79:031602, Mar 2009. doi: 10.1103/PhysRevA.79.031602. URL <https://link.aps.org/doi/10.1103/PhysRevA.79.031602>.
- [40] Tino Weber, Jens Herbig, Michael Mark, Hanns-Christoph Nägerl, and Rudolf Grimm. Bose-einstein condensation of cesium. *Science*, 299(5604):232–235, 2003. doi: 10.1126/science.1079699. URL <https://www.science.org/doi/abs/10.1126/science.1079699>.
- [41] K. Aikawa, A. Frisch, M. Mark, S. Baier, A. Rietzler, R. Grimm, and F. Ferlaino. Bose-einstein condensation of erbium. *Phys. Rev. Lett.*, 108:210401, May 2012. doi: 10.1103/PhysRevLett.108.210401. URL <https://link.aps.org/doi/10.1103/PhysRevLett.108.210401>.
- [42] Mingwu Lu, Nathaniel Q. Burdick, Seo Ho Youn, and Benjamin L. Lev. Strongly dipolar bose-einstein condensate of dysprosium. *Phys. Rev. Lett.*, 107:190401, Oct 2011. doi: 10.1103/PhysRevLett.107.190401. URL <https://link.aps.org/doi/10.1103/PhysRevLett.107.190401>.
- [43] Yijun Tang, Nathaniel Q Burdick, Kristian Baumann, and Benjamin L Lev. Bose–einstein condensation of ^{162}Dy and ^{160}Dy . *New Journal of Physics*, 17(4):045006, apr 2015. doi: 10.1088/1367-2630/17/4/045006. URL <https://dx.doi.org/10.1088/1367-2630/17/4/045006>.
- [44] Takeshi Fukuhara, Seiji Sugawa, and Yoshiro Takahashi. Bose-einstein condensation of an ytterbium isotope. *Phys. Rev. A*, 76:051604, Nov 2007. doi: 10.1103/PhysRevA.76.051604. URL <https://link.aps.org/doi/10.1103/PhysRevA.76.051604>.
- [45] J. R. Ensher, D. S. Jin, M. R. Matthews, C. E. Wieman, and E. A. Cornell. Bose-einstein condensation in a dilute gas: Measurement of energy and ground-state occupation. *Phys. Rev. Lett.*, 77:4984–4987, Dec 1996. doi: 10.1103/PhysRevLett.77.4984. URL <https://link.aps.org/doi/10.1103/PhysRevLett.77.4984>.

- [46] W Ketterle, M R Andrews, K B Davis, D S Durfee, D M Kurn, M O Mewes, and N J van Druten. Bose–einstein condensation of ultracold atomic gases. *Physica Scripta*, 1996(T66):31, jan 1996. doi: 10.1088/0031-8949/1996/T66/004. URL <https://dx.doi.org/10.1088/0031-8949/1996/T66/004>.
- [47] D. M. Stamper-Kurn, M. R. Andrews, A. P. Chikkatur, S. Inouye, H.-J. Miesner, J. Stenger, and W. Ketterle. Optical confinement of a bose-einstein condensate. *Phys. Rev. Lett.*, 80:2027–2030, Mar 1998. doi: 10.1103/PhysRevLett.80.2027. URL <https://link.aps.org/doi/10.1103/PhysRevLett.80.2027>.
- [48] Dan M. Stamper-Kurn and Masahito Ueda. Spinor bose gases: Symmetries, magnetism, and quantum dynamics. *Rev. Mod. Phys.*, 85:1191–1244, Jul 2013. doi: 10.1103/RevModPhys.85.1191. URL <https://link.aps.org/doi/10.1103/RevModPhys.85.1191>.
- [49] J Stenger, S Inouye, DM Stamper-Kurn, H-J Miesner, AP Chikkatur, and W Ketterle. Spin domains in ground-state bose–einstein condensates. *Nature*, 396(6709): 345–348, 1998.
- [50] D. S. Hall, M. R. Matthews, J. R. Ensher, C. E. Wieman, and E. A. Cornell. Dynamics of component separation in a binary mixture of bose-einstein condensates. *Phys. Rev. Lett.*, 81:1539–1542, Aug 1998. doi: 10.1103/PhysRevLett.81.1539. URL <https://link.aps.org/doi/10.1103/PhysRevLett.81.1539>.
- [51] D. S. Hall, M. R. Matthews, C. E. Wieman, and E. A. Cornell. Measurements of relative phase in two-component bose-einstein condensates. *Phys. Rev. Lett.*, 81: 1543–1546, Aug 1998. doi: 10.1103/PhysRevLett.81.1543. URL <https://link.aps.org/doi/10.1103/PhysRevLett.81.1543>.
- [52] M. R. Matthews, D. S. Hall, D. S. Jin, J. R. Ensher, C. E. Wieman, E. A. Cornell, F. Dalfovo, C. Minniti, and S. Stringari. Dynamical response of a bose-einstein condensate to a discontinuous change in internal state. *Phys. Rev. Lett.*, 81:243–247, Jul 1998. doi: 10.1103/PhysRevLett.81.243. URL <https://link.aps.org/doi/10.1103/PhysRevLett.81.243>.
- [53] M. D. Barrett, J. A. Sauer, and M. S. Chapman. All-optical formation of an atomic bose-einstein condensate. *Phys. Rev. Lett.*, 87:010404, Jun 2001.

- doi: 10.1103/PhysRevLett.87.010404. URL <https://link.aps.org/doi/10.1103/PhysRevLett.87.010404>.
- [54] Tin-Lun Ho. Spinor bose condensates in optical traps. *Phys. Rev. Lett.*, 81:742–745, Jul 1998. doi: 10.1103/PhysRevLett.81.742. URL <https://link.aps.org/doi/10.1103/PhysRevLett.81.742>.
- [55] Tetsuo Ohmi and Kazushige Machida. Bose-einstein condensation with internal degrees of freedom in alkali atom gases. *Journal of the Physical Society of Japan*, 67(6):1822–1825, 1998. doi: 10.1143/JPSJ.67.1822. URL <https://doi.org/10.1143/JPSJ.67.1822>.
- [56] D. M. Stamper-Kurn and W. Ketterle. Spinor condensates and light scattering from bose-einstein condensates. In *Les Houches - Ecole d'Ete de Physique Theorique*, pages 139–217. Springer Berlin Heidelberg. doi: 10.1007/3-540-45338-5_2. URL https://doi.org/10.1007%2F3-540-45338-5_2.
- [57] Yuki Kawaguchi, Hiroki Saito, and Masahito Ueda. Spontaneous circulation in ground-state spinor dipolar bose-einstein condensates. *Phys. Rev. Lett.*, 97:130404, Sep 2006. doi: 10.1103/PhysRevLett.97.130404. URL <https://link.aps.org/doi/10.1103/PhysRevLett.97.130404>.
- [58] A. E. Leanhardt, Y. Shin, D. Kielpinski, D. E. Pritchard, and W. Ketterle. Coreless vortex formation in a spinor bose-einstein condensate. *Phys. Rev. Lett.*, 90:140403, Apr 2003. doi: 10.1103/PhysRevLett.90.140403. URL <https://link.aps.org/doi/10.1103/PhysRevLett.90.140403>.
- [59] Erich J. Mueller. Spin textures in slowly rotating bose-einstein condensates. *Phys. Rev. A*, 69:033606, Mar 2004. doi: 10.1103/PhysRevA.69.033606. URL <https://link.aps.org/doi/10.1103/PhysRevA.69.033606>.
- [60] Masaya Kunimi. Metastable spin textures and nambu-goldstone modes of a ferromagnetic spin-1 bose-einstein condensate confined in a ring trap. *Phys. Rev. A*, 90:063632, Dec 2014. doi: 10.1103/PhysRevA.90.063632. URL <https://link.aps.org/doi/10.1103/PhysRevA.90.063632>.
- [61] Masahito Ueda. Topological aspects in spinor bose-einstein condensates. *Reports*

- on Progress in Physics*, 77(12):122401, nov 2014. doi: 10.1088/0034-4885/77/12/122401. URL <https://dx.doi.org/10.1088/0034-4885/77/12/122401>.
- [62] Magnus O. Borgh and Janne Ruostekoski. Topological interface engineering and defect crossing in ultracold atomic gases. *Phys. Rev. Lett.*, 109:015302, Jul 2012. doi: 10.1103/PhysRevLett.109.015302. URL <https://link.aps.org/doi/10.1103/PhysRevLett.109.015302>.
- [63] Magnus O. Borgh and Janne Ruostekoski. Topological interface physics of defects and textures in spinor bose-einstein condensates. *Phys. Rev. A*, 87:033617, Mar 2013. doi: 10.1103/PhysRevA.87.033617. URL <https://link.aps.org/doi/10.1103/PhysRevA.87.033617>.
- [64] M O Borgh, J Lovegrove, and J Ruostekoski. Imprinting a topological interface using zeeman shifts in an atomic spinor bose-einstein condensate. *New Journal of Physics*, 16(5):053046, may 2014. doi: 10.1088/1367-2630/16/5/053046. URL <https://dx.doi.org/10.1088/1367-2630/16/5/053046>.
- [65] Gordon W. Semenoff and Fei Zhou. Discrete symmetries and $1/3$ -quantum vortices in condensates of $f = 2$ cold atoms. *Phys. Rev. Lett.*, 98:100401, Mar 2007. doi: 10.1103/PhysRevLett.98.100401. URL <https://link.aps.org/doi/10.1103/PhysRevLett.98.100401>.
- [66] U. Leonhardt and G. E. Volovik. How to create an alice string (half-quantum vortex) in a vector bose-einstein condensate. *Journal of Experimental and Theoretical Physics Letters*, 72(2):46–48, Jul 2000. ISSN 1090-6487. doi: 10.1134/1.1312008. URL <https://doi.org/10.1134/1.1312008>.
- [67] Seong-Ho Shinn and Uwe R. Fischer. Mesoscopics of half-quantum vortex pair deconfinement in a trapped spin-one condensate. *Phys. Rev. A*, 98:053602, Nov 2018. doi: 10.1103/PhysRevA.98.053602. URL <https://link.aps.org/doi/10.1103/PhysRevA.98.053602>.
- [68] J. Ruostekoski and J. R. Anglin. Monopole core instability and alice rings in spinor bose-einstein condensates. *Phys. Rev. Lett.*, 91:190402, Nov 2003. doi: 10.1103/PhysRevLett.91.190402. URL <https://link.aps.org/doi/10.1103/PhysRevLett.91.190402>.

- [69] Michikazu Kobayashi, Yuki Kawaguchi, Muneto Nitta, and Masahito Ueda. Collision dynamics and rung formation of non-abelian vortices. *Phys. Rev. Lett.*, 103:115301, Sep 2009. doi: 10.1103/PhysRevLett.103.115301. URL <https://link.aps.org/doi/10.1103/PhysRevLett.103.115301>.
- [70] Magnus O. Borgh and Janne Ruostekoski. Core structure and non-abelian reconnection of defects in a biaxial nematic spin-2 bose-einstein condensate. *Phys. Rev. Lett.*, 117:275302, Dec 2016. doi: 10.1103/PhysRevLett.117.275302. URL <https://link.aps.org/doi/10.1103/PhysRevLett.117.275302>.
- [71] H. E. Nistazakis, D. J. Frantzeskakis, P. G. Kevrekidis, B. A. Malomed, and R. Carretero-González. Bright-dark soliton complexes in spinor bose-einstein condensates. *Phys. Rev. A*, 77:033612, Mar 2008. doi: 10.1103/PhysRevA.77.033612. URL <https://link.aps.org/doi/10.1103/PhysRevA.77.033612>.
- [72] T. M. Bersano, V. Gokhroo, M. A. Khamehchi, J. D'Ambroise, D. J. Frantzeskakis, P. Engels, and P. G. Kevrekidis. Three-component soliton states in spinor $f = 1$ bose-einstein condensates. *Phys. Rev. Lett.*, 120:063202, Feb 2018. doi: 10.1103/PhysRevLett.120.063202. URL <https://link.aps.org/doi/10.1103/PhysRevLett.120.063202>.
- [73] G C Katsimiga, S I Mistakidis, P Schmelcher, and P G Kevrekidis. Phase diagram, stability and magnetic properties of nonlinear excitations in spinor bose-einstein condensates. *New Journal of Physics*, 23(1):013015, feb 2021. doi: 10.1088/1367-2630/abd27c. URL <https://dx.doi.org/10.1088/1367-2630/abd27c>.
- [74] Gautam Hegde, Sandra M. Jose, and Rejish Nath. Dynamics of a pair of overlapping polar bright solitons in spin-1 bose-einstein condensates. *Phys. Rev. A*, 106:043307, Oct 2022. doi: 10.1103/PhysRevA.106.043307. URL <https://link.aps.org/doi/10.1103/PhysRevA.106.043307>.
- [75] YONG-QING LIU. Magnons interaction of spinor bose-einstein condensates in an optical lattice. *PRAMANA- J. Phys.*, 73(6):1105–1110, 2009. URL <https://www.ias.ac.in/article/fulltext/pram/073/06/1105-1110>.
- [76] G. Edward Marti, Andrew MacRae, Ryan Olf, Sean Lourette, Fang Fang, and Dan M. Stamper-Kurn. Coherent magnon optics in a ferromagnetic

- spinor bose-einstein condensate. *Phys. Rev. Lett.*, 113:155302, Oct 2014. doi: 10.1103/PhysRevLett.113.155302. URL <https://link.aps.org/doi/10.1103/PhysRevLett.113.155302>.
- [77] Fang Fang, Ryan Olf, Shun Wu, Holger Kadau, and Dan M. Stamper-Kurn. Condensing magnons in a degenerate ferromagnetic spinor bose gas. *Phys. Rev. Lett.*, 116:095301, Mar 2016. doi: 10.1103/PhysRevLett.116.095301. URL <https://link.aps.org/doi/10.1103/PhysRevLett.116.095301>.
- [78] Z. D. Li, P. B. He, L. Li, J. Q. Liang, and W. M. Liu. Magnetic soliton and soliton collisions of spinor bose-einstein condensates in an optical lattice. *Phys. Rev. A*, 71:053611, May 2005. doi: 10.1103/PhysRevA.71.053611. URL <https://link.aps.org/doi/10.1103/PhysRevA.71.053611>.
- [79] X. Chai, D. Lao, Kazuya Fujimoto, Ryusuke Hamazaki, Masahito Ueda, and C. Raman. Magnetic solitons in a spin-1 bose-einstein condensate. *Phys. Rev. Lett.*, 125:030402, Jul 2020. doi: 10.1103/PhysRevLett.125.030402. URL <https://link.aps.org/doi/10.1103/PhysRevLett.125.030402>.
- [80] Konstantin Tiurev, Tuomas Ollikainen, Pekko Kuopanportti, Mikio Nakahara, David S Hall, and Mikko Möttönen. Three-dimensional skyrmions in spin-2 bose-einstein condensates. *New Journal of Physics*, 20(5):055011, may 2018. doi: 10.1088/1367-2630/aac2a8. URL <https://dx.doi.org/10.1088/1367-2630/aac2a8>.
- [81] Jae-yoon Choi, Woo Jin Kwon, and Yong-il Shin. Observation of topologically stable 2d skyrmions in an antiferromagnetic spinor bose-einstein condensate. *Phys. Rev. Lett.*, 108:035301, Jan 2012. doi: 10.1103/PhysRevLett.108.035301. URL <https://link.aps.org/doi/10.1103/PhysRevLett.108.035301>.
- [82] A. Tokuno, Y. Mitamura, M. Oshikawa, and I. F. Herbut. Skyrmion in spinor condensates and its stability in trap potentials. *Phys. Rev. A*, 79:053626, May 2009. doi: 10.1103/PhysRevA.79.053626. URL <https://link.aps.org/doi/10.1103/PhysRevA.79.053626>.
- [83] Yuki Kawaguchi and Masahito Ueda. Spinor bose-einstein condensates. *Physics Reports*, 520(5):253 – 381, 2012. ISSN 0370-1573. doi: <https://doi.org/10.1016/>

- j.physrep.2012.07.005. URL <http://www.sciencedirect.com/science/article/pii/S0370157312002098>. Spinor Bose–Einstein condensates.
- [84] M.-S. Chang, C. D. Hamley, M. D. Barrett, J. A. Sauer, K. M. Fortier, W. Zhang, L. You, and M. S. Chapman. Observation of spinor dynamics in optically trapped ^{87}Rb bose-einstein condensates. *Phys. Rev. Lett.*, 92:140403, Apr 2004. doi: 10.1103/PhysRevLett.92.140403. URL <https://link.aps.org/doi/10.1103/PhysRevLett.92.140403>.
- [85] S. Yi, Ö. E. Müstecaphoğlu, C. P. Sun, and L. You. Single-mode approximation in a spinor-1 atomic condensate. *Phys. Rev. A*, 66:011601, Jul 2002. doi: 10.1103/PhysRevA.66.011601. URL <https://link.aps.org/doi/10.1103/PhysRevA.66.011601>.
- [86] Wenxian Zhang, D. L. Zhou, M.-S. Chang, M. S. Chapman, and L. You. Coherent spin mixing dynamics in a spin-1 atomic condensate. *Phys. Rev. A*, 72:013602, Jul 2005. doi: 10.1103/PhysRevA.72.013602. URL <https://link.aps.org/doi/10.1103/PhysRevA.72.013602>.
- [87] Jianwen Jie, Q. Guan, S. Zhong, A. Schwettmann, and D. Blume. Mean-field spin-oscillation dynamics beyond the single-mode approximation for a harmonically trapped spin-1 bose-einstein condensate. *Phys. Rev. A*, 102:023324, Aug 2020. doi: 10.1103/PhysRevA.102.023324. URL <https://link.aps.org/doi/10.1103/PhysRevA.102.023324>.
- [88] J. Jie, S. Zhong, Q. Zhang, I. Morgenstern, H. G. Ooi, Q. Guan, A. Bhagat, D. Nematollahi, A. Schwettmann, and D. Blume. Dynamical mean-field driven spinor condensate physics beyond the single-mode approximation, 2023. URL <https://arxiv.org/abs/2301.06461>.
- [89] Stuart S. Szigeti, Onur Hosten, and Simon A. Haine. Improving cold-atom sensors with quantum entanglement: Prospects and challenges. *Applied Physics Letters*, 118(14), 04 2021. ISSN 0003-6951. doi: 10.1063/5.0050235. URL <https://doi.org/10.1063/5.0050235>. 140501.
- [90] M. Vengalattore, J. M. Higbie, S. R. Leslie, J. Guzman, L. E. Sadler, and D. M. Stamper-Kurn. High-resolution magnetometry with a spinor bose-einstein conden-

- sate. *Phys. Rev. Lett.*, 98:200801, May 2007. doi: 10.1103/PhysRevLett.98.200801. URL <https://link.aps.org/doi/10.1103/PhysRevLett.98.200801>.
- [91] R. J. Sewell, M. Koschorreck, M. Napolitano, B. Dubost, N. Behbood, and M. W. Mitchell. Magnetic sensitivity beyond the projection noise limit by spin squeezing. *Phys. Rev. Lett.*, 109:253605, Dec 2012. doi: 10.1103/PhysRevLett.109.253605. URL <https://link.aps.org/doi/10.1103/PhysRevLett.109.253605>.
- [92] Yuval Cohen, Krishna Jadeja, Sindi Sula, Michela Venturelli, Cameron Deans, Luca Marmugi, and Ferruccio Renzoni. A cold atom radio-frequency magnetometer. *Applied Physics Letters*, 114(7), 02 2019. ISSN 0003-6951. doi: 10.1063/1.5084004. URL <https://doi.org/10.1063/1.5084004>. 073505.
- [93] Silvana Palacios Alvarez, Pau Gomez, Simon Coop, Roberto Zamora-Zamora, Chiara Mazzinghi, and Morgan W. Mitchell. Single-domain bose condensate magnetometer achieves energy resolution per bandwidth below $\times 10^6$. *Proceedings of the National Academy of Sciences*, 119(6):e2115339119, 2022. doi: 10.1073/pnas.2115339119. URL <https://www.pnas.org/doi/abs/10.1073/pnas.2115339119>.
- [94] P. Feldmann, M. Gessner, M. Gabbrielli, C. Klempt, L. Santos, L. Pezzè, and A. Smerzi. Interferometric sensitivity and entanglement by scanning through quantum phase transitions in spinor bose-einstein condensates. *Phys. Rev. A*, 97:032339, Mar 2018. doi: 10.1103/PhysRevA.97.032339. URL <https://link.aps.org/doi/10.1103/PhysRevA.97.032339>.
- [95] E. Timmermans. Phase separation of bose-einstein condensates. *Phys. Rev. Lett.*, 81:5718–5721, Dec 1998. doi: 10.1103/PhysRevLett.81.5718. URL <https://link.aps.org/doi/10.1103/PhysRevLett.81.5718>.
- [96] Tomasz Świsłocki and Michał Matuszewski. Controlled creation of spin domains in spin-1 bose-einstein condensates by phase separation. *Phys. Rev. A*, 85:023601, Feb 2012. doi: 10.1103/PhysRevA.85.023601. URL <https://link.aps.org/doi/10.1103/PhysRevA.85.023601>.
- [97] Kui-Tian Xi, Jinbin Li, and Da-Ning Shi. Phase separation of a two-component dipolar bose-einstein condensate in the quasi-one-dimensional and quasi-two-

- dimensional regime. *Phys. Rev. A*, 84:013619, Jul 2011. doi: 10.1103/PhysRevA.84.013619. URL <https://link.aps.org/doi/10.1103/PhysRevA.84.013619>.
- [98] Soumik Bandyopadhyay, Arko Roy, and D. Angom. Dynamics of phase separation in two-species bose-einstein condensates with vortices. *Phys. Rev. A*, 96:043603, Oct 2017. doi: 10.1103/PhysRevA.96.043603. URL <https://link.aps.org/doi/10.1103/PhysRevA.96.043603>.
- [99] Tomoya Isoshima, Kazushige Machida, and Tetsuo Ohmi. Spin-domain formation in spinor bose-einstein condensation. *Phys. Rev. A*, 60:4857–4863, Dec 1999. doi: 10.1103/PhysRevA.60.4857. URL <https://link.aps.org/doi/10.1103/PhysRevA.60.4857>.
- [100] Michal Matuszewski, Tristram J. Alexander, and Yuri S. Kivshar. Spin-domain formation in antiferromagnetic condensates. *Phys. Rev. A*, 78:023632, Aug 2008. doi: 10.1103/PhysRevA.78.023632. URL <https://link.aps.org/doi/10.1103/PhysRevA.78.023632>.
- [101] Michał Matuszewski, Tristram J. Alexander, and Yuri S. Kivshar. Excited spin states and phase separation in spinor bose-einstein condensates. *Phys. Rev. A*, 80:023602, Aug 2009. doi: 10.1103/PhysRevA.80.023602. URL <https://link.aps.org/doi/10.1103/PhysRevA.80.023602>.
- [102] Tin-Lun Ho and V. B. Shenoy. Binary mixtures of bose condensates of alkali atoms. *Phys. Rev. Lett.*, 77:3276–3279, Oct 1996. doi: 10.1103/PhysRevLett.77.3276. URL <https://link.aps.org/doi/10.1103/PhysRevLett.77.3276>.
- [103] S Bhuvaneswari, K Nithyanandan, and P Muruganandam. Spotlighting phase separation in rashba spin-orbit coupled bose–einstein condensates in two dimensions. *Journal of Physics Communications*, 2(2):025008, 2018. URL <http://stacks.iop.org/2399-6528/2/i=2/a=025008>.
- [104] L. Wen, W. M. Liu, Yongyong Cai, J. M. Zhang, and Jiangping Hu. Controlling phase separation of a two-component bose-einstein condensate by confinement. *Phys. Rev. A*, 85:043602, Apr 2012. doi: 10.1103/PhysRevA.85.043602. URL <https://link.aps.org/doi/10.1103/PhysRevA.85.043602>.
- [105] Zuhan Liu. Phase separation of two-component bose–einstein condensates. *Journal*

- of Mathematical Physics*, 50(10):102104, 2009. doi: 10.1063/1.3243875. URL <https://doi.org/10.1063/1.3243875>.
- [106] Long Zhu and Jinbin Li. Phase separation of two-component bose-einstein condensates with monopolar interaction. *Modern Physics Letters B*, 31(23):1750215, 2017. doi: 10.1142/S0217984917502153. URL <https://doi.org/10.1142/S0217984917502153>.
- [107] Satoshi Tojo, Yoshihisa Taguchi, Yuta Masuyama, Taro Hayashi, Hiroki Saito, and Takuya Hirano. Controlling phase separation of binary bose-einstein condensates via mixed-spin-channel feshbach resonance. *Phys. Rev. A*, 82:033609, Sep 2010. doi: 10.1103/PhysRevA.82.033609. URL <https://link.aps.org/doi/10.1103/PhysRevA.82.033609>.
- [108] Ji Li, Yan-Mei Yu, Kai-Jun Jiang, and Wu-Ming Liu. Phase separation and hidden vortices induced by spin-orbit coupling in spin-1 bose-einstein condensates. *arXiv preprint arXiv:1802.00138*, 2018.
- [109] Kean Loon Lee, Nils B. Jørgensen, I-Kang Liu, Lars Wacker, Jan J. Arlt, and Nick P. Proukakis. Phase separation and dynamics of two-component bose-einstein condensates. *Phys. Rev. A*, 94:013602, Jul 2016. doi: 10.1103/PhysRevA.94.013602. URL <https://link.aps.org/doi/10.1103/PhysRevA.94.013602>.
- [110] Jacopo Sabbatini, Wojciech H. Zurek, and Matthew J. Davis. Phase separation and pattern formation in a binary bose-einstein condensate. *Phys. Rev. Lett.*, 107:230402, Nov 2011. doi: 10.1103/PhysRevLett.107.230402. URL <https://link.aps.org/doi/10.1103/PhysRevLett.107.230402>.
- [111] Sandeep Gautam and S. K. Adhikari. Phase separation in a spin-orbit-coupled bose-einstein condensate. *Phys. Rev. A*, 90:043619, Oct 2014. doi: 10.1103/PhysRevA.90.043619. URL <https://link.aps.org/doi/10.1103/PhysRevA.90.043619>.
- [112] S Gautam and D Angom. Phase separation of binary condensates in harmonic and lattice potentials. *Journal of Physics B: Atomic, Molecular and Optical Physics*, 44(2):025302, 2011. URL <http://stacks.iop.org/0953-4075/44/i=2/a=025302>.
- [113] Hiroki Saito and Masahito Ueda. Spontaneous magnetization and structure formation in a spin-1 ferromagnetic bose-einstein condensate. *Phys. Rev. A*, 72:023610,

- Aug 2005. doi: 10.1103/PhysRevA.72.023610. URL <https://link.aps.org/doi/10.1103/PhysRevA.72.023610>.
- [114] Michał Matuszewski. Ground states of trapped spin-1 condensates in magnetic field. *Phys. Rev. A*, 82:053630, Nov 2010. doi: 10.1103/PhysRevA.82.053630. URL <https://link.aps.org/doi/10.1103/PhysRevA.82.053630>.
- [115] Sandeep Gautam and S. K. Adhikari. Analytic models for the density of a ground-state spinor condensate. *Phys. Rev. A*, 92:023616, Aug 2015. doi: 10.1103/PhysRevA.92.023616. URL <https://link.aps.org/doi/10.1103/PhysRevA.92.023616>.
- [116] K Jiménez-García, A Invernizzi, B Evrard, C Frapolli, J Dalibard, and F Gerbier. Spontaneous formation and relaxation of spin domains in antiferromagnetic spin-1 quasi-condensates. *Nat Commun*, 10:1422, 2019. doi: <https://doi.org/10.1038/s41467-019-08505-6>.
- [117] Ivana Vidanović, N J van Druten, and Masudul Haque. Spin modulation instabilities and phase separation dynamics in trapped two-component bose condensates. *New Journal of Physics*, 15(3):035008, 2013. URL <http://stacks.iop.org/1367-2630/15/i=3/a=035008>.
- [118] Chunji Wang, Chao Gao, Chao-Ming Jian, and Hui Zhai. Spin-orbit coupled spinor bose-einstein condensates. *Phys. Rev. Lett.*, 105:160403, Oct 2010. doi: 10.1103/PhysRevLett.105.160403. URL <https://link.aps.org/doi/10.1103/PhysRevLett.105.160403>.
- [119] D. M. Stamper-Kurn, M. R. Andrews, A. P. Chikkatur, S. Inouye, H.-J. Miesner, J. Stenger, and W. Ketterle. Optical confinement of a bose-einstein condensate. *Phys. Rev. Lett.*, 80:2027–2030, Mar 1998. doi: 10.1103/PhysRevLett.80.2027. URL <https://link.aps.org/doi/10.1103/PhysRevLett.80.2027>.
- [120] Nick Proukakis. *Quantum gases: finite temperature and non-equilibrium dynamics*, volume 1. World Scientific, 2013.
- [121] Projjwal K Kanjilal and A Bhattacharyay. Spin domains in ground state of a trapped spin-1 condensate: a general study under thomas–fermi approximation.

- Physica Scripta*, 95(4):045702, feb 2020. doi: 10.1088/1402-4896/ab5e95. URL <https://doi.org/10.1088%2F1402-4896%2Fab5e95>.
- [122] Projjwal K Kanjilal and A Bhattacharyay. Corrigendum: Spin domains in ground state of a trapped spin-1 condensate: A general study under thomas-fermi approximation (2020 phys. scr. 95 045702). *Physica Scripta*, 97(12):129501, nov 2022. doi: 10.1088/1402-4896/ac9eec. URL <https://dx.doi.org/10.1088/1402-4896/ac9eec>.
- [123] Kanjilal, Projjwal Kanti and Bhattacharyay, A. A variational approach for the ground-state profile of a trapped spinor-bec: a detailed study of phase transition in spin-1 condensate at zero magnetic field. *Eur. Phys. J. Plus*, 137(5):547, 2022. doi: 10.1140/epjp/s13360-022-02729-0. URL <https://doi.org/10.1140/epjp/s13360-022-02729-0>.
- [124] M. D. Barrett, J. A. Sauer, and M. S. Chapman. All-optical formation of an atomic bose-einstein condensate. *Phys. Rev. Lett.*, 87:010404, Jun 2001. doi: 10.1103/PhysRevLett.87.010404. URL <https://link.aps.org/doi/10.1103/PhysRevLett.87.010404>.
- [125] A. J. Moerdijk, B. J. Verhaar, and A. Axelsson. Resonances in ultracold collisions of ${}^6\text{Li}$, ${}^7\text{Li}$, and ${}^{23}\text{Na}$. *Phys. Rev. A*, 51:4852–4861, Jun 1995. doi: 10.1103/PhysRevA.51.4852. URL <https://link.aps.org/doi/10.1103/PhysRevA.51.4852>.
- [126] S Inouye, MR Andrews, J Stenger, H-J Miesner, DM Stamper-Kurn, and W Ketterle. Observation of feshbach resonances in a bose–einstein condensate. *Nature*, 392(6672):151, 1998.
- [127] Cheng Chin, Rudolf Grimm, Paul Julienne, and Eite Tiesinga. Feshbach resonances in ultracold gases. *Rev. Mod. Phys.*, 82:1225–1286, Apr 2010. doi: 10.1103/RevModPhys.82.1225. URL <https://link.aps.org/doi/10.1103/RevModPhys.82.1225>.
- [128] C. Frapolli, T. Zibold, A. Invernizzi, K. Jiménez-García, J. Dalibard, and F. Gerbier. Stepwise bose-einstein condensation in a spinor gas. *Phys. Rev. Lett.*, 119:050404, Aug 2017. doi: 10.1103/PhysRevLett.119.050404. URL <https://link.aps.org/doi/10.1103/PhysRevLett.119.050404>.

- [129] Wenxian Zhang, Su Yi, and Li You. Mean field ground state of a spin-1 condensate in a magnetic field. *New Journal of Physics*, 5:77–77, jun 2003. doi: 10.1088/1367-2630/5/1/377. URL <https://doi.org/10.1088%2F1367-2630%2F5%2F1%2F377>.
- [130] S. Yi, Ö. E. Müstecaplıoğlu, C. P. Sun, and L. You. Single-mode approximation in a spinor-1 atomic condensate. *Phys. Rev. A*, 66:011601, Jul 2002. doi: 10.1103/PhysRevA.66.011601. URL <https://link.aps.org/doi/10.1103/PhysRevA.66.011601>.
- [131] H. Pu, C. K. Law, S. Raghavan, J. H. Eberly, and N. P. Bigelow. Spin-mixing dynamics of a spinor bose-einstein condensate. *Phys. Rev. A*, 60:1463–1470, Aug 1999. doi: 10.1103/PhysRevA.60.1463. URL <https://link.aps.org/doi/10.1103/PhysRevA.60.1463>.
- [132] Nguyen Thanh Phuc, Yuki Kawaguchi, and Masahito Ueda. Effects of thermal and quantum fluctuations on the phase diagram of a spin-1 ^{87}Rb bose-einstein condensate. *Phys. Rev. A*, 84:043645, Oct 2011. doi: 10.1103/PhysRevA.84.043645. URL <https://link.aps.org/doi/10.1103/PhysRevA.84.043645>.
- [133] Yuki Kawaguchi, Nguyen Thanh Phuc, and P. Blair Blakie. Finite-temperature phase diagram of a spin-1 bose gas. *Phys. Rev. A*, 85:053611, May 2012. doi: 10.1103/PhysRevA.85.053611. URL <https://link.aps.org/doi/10.1103/PhysRevA.85.053611>.
- [134] E. Serrano-Ensaístiga and F. Mireles. Spinor bose-einstein condensates: self-consistent symmetries and characterization, 2022. URL <https://arxiv.org/abs/2211.16428>.
- [135] K. M. Mittal, S. I. Mistakidis, P. G. Kevrekidis, and P. Schmelcher. Many-body effects on second-order phase transitions in spinor bose-einstein condensates and breathing dynamics. *Phys. Rev. A*, 102:013302, Jul 2020. doi: 10.1103/PhysRevA.102.013302. URL <https://link.aps.org/doi/10.1103/PhysRevA.102.013302>.
- [136] Abhijit Pendse and Arijit Bhattacharyay. Effect of non-local interactions on the vortex solution in bose-einstein condensates. *The European Physical Journal B*,

- 90:244, 2017. ISSN 1745-2481. doi: 10.1140/epjb/e2017-80213-6. URL <https://doi.org/10.1140/epjb/e2017-80213-6>.
- [137] Jen-Hao Chen, I-Liang Chern, and Weichung Wang. A complete study of the ground state phase diagrams of spin-1 bose–einstein condensates in a magnetic field via continuation methods. *Journal of Scientific Computing*, 64:35–54, 2015. doi: 10.1007/s10915-014-9924-z.
- [138] L.P. Pitaevskii, S. Stringari, and Oxford University Press. *Bose-Einstein Condensation*. International Series of Monographs on Physics. Clarendon Press, 2003. ISBN 9780198507192. URL <https://global.oup.com/academic/product/bose-einstein-condensation-9780198507192?cc=in&lang=en&>.
- [139] Chuanzhou Zhu, Lin Dong, and Han Pu. Harmonically trapped atoms with spin–orbit coupling. *Journal of Physics B: Atomic, Molecular and Optical Physics*, 49(14):145301, jun 2016. doi: 10.1088/0953-4075/49/14/145301. URL <https://doi.org/10.1088/0953-4075/49/14/145301>.
- [140] Mark Edwards and K. Burnett. Numerical solution of the nonlinear schrödinger equation for small samples of trapped neutral atoms. *Phys. Rev. A*, 51:1382–1386, Feb 1995. doi: 10.1103/PhysRevA.51.1382. URL <https://link.aps.org/doi/10.1103/PhysRevA.51.1382>.
- [141] Pardeep Kaur, Arko Roy, and Sandeep Gautam. Fortress: Fortran programs for solving coupled gross–pitaevskii equations for spin–orbit coupled spin-1 bose–einstein condensate. *Computer Physics Communications*, 259:107671, 2021. ISSN 0010-4655. doi: <https://doi.org/10.1016/j.cpc.2020.107671>. URL <https://www.sciencedirect.com/science/article/pii/S001046552030326X>.
- [142] Weizhu Bao and Fong Yin Lim. Computing ground states of spin-1 bose–einstein condensates by the normalized gradient flow. *SIAM Journal on Scientific Computing*, 30(4):1925–1948, 2008. doi: 10.1137/070698488. URL <https://doi.org/10.1137/070698488>.
- [143] D. J. Papoular, G. V. Shlyapnikov, and J. Dalibard. Microwave-induced fano-feshbach resonances. *Phys. Rev. A*, 81:041603, Apr 2010. doi: 10.1103/PhysRevA.81.041603. URL <https://link.aps.org/doi/10.1103/PhysRevA.81.041603>.

- [144] Sandhya Ganesh. Modelling spin-1 rubidium-87 bose einstein condensate to study ground states under inhomogenous magnetic fields. Master's thesis, KTH, Applied Physics, 2019.
- [145] L. E. Sadler, J. M. Higbie, S. R. Leslie, M. Vengalattore, and D. M. Stamper-Kurn. Spontaneous symmetry breaking in a quenched ferromagnetic spinor bose-einstein condensate. *Nature*, 443(7109):312–315, Sep 2006. ISSN 1476-4687. doi: 10.1038/nature05094. URL <https://doi.org/10.1038/nature05094>.
- [146] Hiroki Saito, Yuki Kawaguchi, and Masahito Ueda. Topological defect formation in a quenched ferromagnetic bose-einstein condensates. *Phys. Rev. A*, 75:013621, Jan 2007. doi: 10.1103/PhysRevA.75.013621. URL <https://link.aps.org/doi/10.1103/PhysRevA.75.013621>.
- [147] Hiroki Saito, Yuki Kawaguchi, and Masahito Ueda. Kibble-zurek mechanism in a quenched ferromagnetic bose-einstein condensate. *Phys. Rev. A*, 76:043613, Oct 2007. doi: 10.1103/PhysRevA.76.043613. URL <https://link.aps.org/doi/10.1103/PhysRevA.76.043613>.